PHYSICAL REVIEW D VOLUME 6, NUMBER 5 1 SEPTEMBER 1972

Two-Body Strange-Particle Final States in π^-p Interactions at 4.5 and 6 GeV/c*

David J. Crennell, Howard A. Gordon, Kwan-Wu Lai, and J. Michael Scarr
Physics Department, Brookhaven National Laboratory, Upton, New York 11973

(Received 13 April 1972)

Results on the following π^-p reactions involving a hyperon are studied at 4.5 and 6.0 GeV/c from a high-statistics bubble-chamber experiment. (1) $\pi^-p \to (\Lambda, \Sigma^0)K^0$: Differential cross sections and hyperon polarizations are presented. Comparison with the line-reversed reactions $\bar{K}N \to (\Lambda, \Sigma^0)\pi$ indicates the failure of the predictions of $K^*(890)$ and $K^*(1420)$ exchange degeneracy. Effective trajectories for these two reactions are compared. Shrinkage is observed in $\bar{K}N \to \Lambda\pi$ and not in $\pi^-p \to \Lambda K^0$. (2) $\pi^-p \to (\Lambda, \Sigma^0)K^*(890)^0$: Differential cross sections, hyperon polarizations, and $K^*(890)^0$ density-matrix elements are determined. $\Lambda K^*(890)^0$ decay correlations are found to impose strong constraints on the scattering amplitudes. The data indicate that both natural- and unnatural-parity exchanges contribute large, but opposite, Λ polarizations. This behavior cannot be explained by a simple exchange model utilizing K and the exchange-degenerate $K^*(890)$ and $K^*(1420)$ only. Additional trajectories or absorption effects are required to obtain the observed Λ-polarization effects. Comparison of $\Lambda K^*(890)^0$ and $\Sigma^0K^*(890)^0$ indicates the greater importance of unnatural-parity exchange in the former reaction. We observe no evidence for deviations from isospin predictions in $\Lambda K^*(890)^0$ production where $K^*(890)^0 \to K^+\pi^-$ and $K^0_S\pi^0$. (3) $\pi^-p \to \Lambda K^*(1420)^0$ and $\Lambda K^*(1300)^0$: $K^*(1420)^0$ density-matrix elements satisfying positivity constraints are determined allowing for s-wave interference effects. Evidence of the existence of a narrow $K^*(1300)^0 \to K\pi\pi$ with a dominant $K^+\rho^-$ decay mode is observed in the 4.5- and 6-GeV/c data. (4) $\Sigma(1385)$, $\Lambda(1405)$, $\Lambda(1520)$ production: Differential cross sections for the quasi-two-body reactions $\pi^-p \to Y^0K^0$, where Y^0 is $\Lambda(1405)$, $\Lambda(1520)$, or $\Sigma(1385)^0$, are presented and found to have a very similar flat slope in the forward direction. Data for forward K^+ scattering in the reaction $\pi^-p \to \Sigma(1385)^-K^+$ are presented and discussed. It is argued that this forward peak cannot be explained by kinematic reflection or an s-channel effect and therefore must be due to either two-particle exchange or a single exotic exchange in the t channel.

I. INTRODUCTION

Differential cross sections and some hyperon polarizations and spin-density-matrix elements are presented for the following reactions:

$$\pi^-p \to \Lambda K^0 \tag{1a}$$

$$\to \Lambda K^*(890)^0 \tag{2a}$$

$$\to \Lambda K^*(1420)^0 \tag{3a}$$

$$\to \Lambda(1405)K^0 \tag{4}$$

$$\to \Lambda(1520)K^0, \tag{5}$$

$$\pi^-p \to \Sigma^0K^0 \tag{1b}$$

$$\to \Sigma^0K^*(890)^0 \tag{2b}$$

$$\to \Sigma^0K^*(1420)^0 \tag{3b}$$

$$\to \Sigma(1385)^0K^0 \tag{6}$$

$$\to \Sigma(1385)^-K^+ \tag{7}$$

at 4.5 and 6 GeV/c.

The data for this analysis come from an ~500 000 picture exposure of the Stanford Linear Accelerator Center (SLAC) 82-in. hydrogen bubble chamber to a 4.5-GeV/c π^- beam and an ~200 000 picture exposure of the Brookhaven National Laboratory 80-in. hydrogen bubble chamber to a 6-GeV/c π^- beam. This corresponds to 31.4 events/μb exposure at 4.5 GeV/c and 18 events/μb at 6 GeV/c. The exposures were scanned for all topologies with one or more V^0's. We will present the relevant data for reactions (1)–(7) separately.

II. SEPARATION OF FINAL STATES

A. ΛK^0, Σ^0K^0, and $\Lambda K^0\pi^0$ Final States

1. *Two-V^0 Topology*

When both Λ and K^0 decays are visible within the fiducial volume, events kinematically ambiguous between the four-constraint (4C) reaction $\pi^-p \to \Lambda K^0$ (1a) and the 2C reaction $\pi^-p \to \Sigma^0K^0$ (1b) were assigned to (1a), on the basis that a fit to the 4C hypothesis is more likely to be correct. These kinematic ambiguities amount to 10% of the ΛK^0 sample. Their interpretation as Σ^0K^0 events would lead to a strongly asymmetric Σ^0-decay distribution, a fact which indicates the correctness of the above assignment and that the contamination to the ΛK^0 sample is, at most, a few percent for the two V^0 events. The remaining Σ^0K^0 sample contained approximately 15% kinematic ambiguities with the 1C final state $\Lambda K^0\pi^0$. For the $\Lambda K^0\pi^0$ final state the

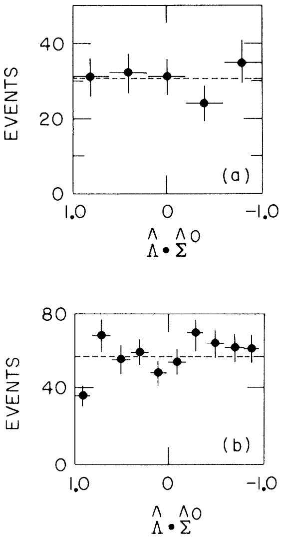

FIG. 1. Σ^0 decay angular distributions. $\hat{\Lambda}$ is the direction of the Λ evaluated in the Σ^0 rest frame. $\hat{\Sigma}^0$ is the direction of the Σ^0 in the over-all center-of-mass system. (a) For reaction $\pi^-p \rightarrow \Sigma^0K^0$ at 4.5 GeV/c. (b) For reaction $\pi^-p \rightarrow \Sigma^0K^+\pi^-$ at 4.5 GeV/c. Dashed line indicates isotropic distribution normalized to the number of events.

square of the missing mass recoiling against K^0, $MM^2(K^0)$, should lie above the kinematic threshold of 1.56 GeV^2. The assignment of these ambiguous events was such that those with $MM^2(K^0) \leq 1.56$ GeV^2 were assigned to reaction (1b). The validity of this assignment is illustrated, for the 4.5-GeV/c data, by the observed isotropic distribution of the $\Sigma^0 \rightarrow \Lambda\gamma$ decay [see Fig. 1(a)]. The remaining events are assigned to the $\Lambda K^0\pi^0$ final state if the kinematic-fit probability, $P(\chi^2)$, $\geq 5\%$ and missing mass squared, $|MM^2|$, ≤ 0.1 GeV^2.

2. *One-V^0 Topology*

Events with either Λ or K^0 decay observed within the fiducial region are used for the reaction $\pi^-p \rightarrow \Lambda K^0$ at 4.5 GeV/c, but only those with visible Λ are used at 6 GeV/c. The Σ^0 contamination is estimated to be less than 5% by interpreting the two V^0 events as if only one V^0 is visible. No one-V^0 events were used for the Σ^0K^0 final state.

B. $\Lambda^0K^+\pi^-$ and $\Sigma^0K^+\pi^-$ Final States

Events ambiguous between the Λ and Σ^0 fits have been assigned to the Λ sample. This is justified by the strong peaking of the $\Sigma^0 \rightarrow \Lambda^0\gamma$ decay distribution at $\hat{\Sigma}\cdot\hat{\Lambda} \approx 1$ for the ambiguous events, in contrast to the required isotropy. For the Σ^0 sample, the effective mass recoiling against the π^-K^+ system is required <1.4 GeV, to minimize the contamination from $\Lambda K^+\pi^-\pi^0$ events. The resulting sample, using 4.5-GeV/c data, shows $\Sigma^0 \rightarrow \Lambda\gamma$ decays consistent with isotropy [see Fig. 1(b)] apart from a loss of ~20 events in the first bin due to allocating all 148 ambiguous events to the Λ sample.

C. $\Lambda K^0\pi^+\pi^-$ and $\Lambda K^+\pi^-\pi^0$ Final States

For the 4.5-GeV/c data, we separate these two final states as follows.

1. *Two-V^0 Topology*

All 451 events satisfying 4C fits to the $\Lambda K^0\pi^+\pi^-$ hypothesis are accepted in that sample.

2. *One-V^0 Topology*

Only events with a visible Λ are used in order to eliminate ambiguities with such final states as $nK^+\bar{K}^0\pi^-$ and $nK^-K^0\pi^+$. The missing mass squared is required to be

$$0.2 < MM^2 < 0.3 \text{ GeV}^2 \text{ for } \Lambda K^0\pi^+\pi^-$$

and

$$-0.04 < MM^2 < 0.08 \text{ GeV}^2 \text{ for } \Lambda K^+\pi^-\pi^0 .$$

There are 1728 events satisfying the $\Lambda K^+\pi^-\pi^0$ hypotheses and 1063 one-V^0 events satisfying the $\Lambda K^0\pi^+\pi^-$ hypotheses. In addition, there are 277 one-V^0 ambiguous events which satisfy both missing-mass criteria and fit both hypotheses. These ambiguous events are assigned to the $\Lambda K^+\pi^-\pi^0$ hypothesis. This allocation is made on the basis of studying scatter plots of neutral versus positive momenta for the two-V^0, unique one-V^0, and ambiguous samples separately. Ambiguous events lie in regions where neutral and positive momenta are approximately equal. A greater loss has been observed in the scatter plot of the unique $\Lambda K^+\pi^-\pi^0$ events than in that of the unique one-V^0 $\Lambda K^0\pi^+\pi^-$ events, and consequently all ambiguous events have been assigned to the former hypothesis. We estimate that less than 33% of these ambiguous events are incorrectly assigned. This corresponds to less than 5% in the final $\Lambda K^0\pi^+\pi^-$ sample and less than 7% in the final two-V^0 and one-V^0 $\Lambda K^0\pi^+\pi^-$ sample. The ratio between one-V^0 and two-V^0 events in the final $\Lambda K^0\pi^+\pi^-$ sample is consistent with the expected ratio.

Because of limited statistics at 6 GeV/c, we assigned half-weight to ~20% of the events ambiguous between these two final states.

D. Corrections and Cross Sections

The lifetimes of seen decays were examined as a function of minimum distance between the production and decay vertices. Stable values of lifetime were obtained at 0.2 cm for Λ and 0.4 cm for K^0, which were taken to be the minimum distances required for the sample. The decays (one or both)

TABLE I. Cross sections and slope parameters for two-body strange-particle reactions at 4.5 and 6 GeV/c.

Reaction	P_{lab} (GeV/c)	No. of events	σ (μb)	$\frac{d\sigma}{dt'} = Ae^{bt'}$ ($\lvert t'_1\rvert \longleftrightarrow \lvert t'_2\rvert$)			
				A (μb/GeV^2)	b (GeV^{-2})	$\lvert t'_1\rvert$ (GeV^2)	$\lvert t'_2\rvert$ (GeV^2)
$\pi^- p \to \Lambda K^0$	4.5 [a]	912	54 ± 2	318 ± 12	7.3 ± 0.3	0	0.4
ΛK^0	6 [b]	326	38 ± 2	231 ± 14	6.7 ± 0.3	0	0.8
$\pi^- p \to \Lambda K^*(890)^0$	4.5	627 ($K^+\pi^-$)	53 ± 2 [c]	130 ± 11	2.5 ± 0.2	0.1	1.6
$\Lambda K^*(890)^0$	6	172 ($K^+\pi^-$)	25.5 ± 2 [c]	92 ± 14	3.2 ± 0.4	0.1	1.5
$\pi^- p \to \Lambda K^*(1420)^0$	4.5	193 ($K^+\pi^-$)	16.5 ± 2.5 [d]	21 ± 5	1.9 ± 0.4	0	2
$\Lambda K^*(1420)^0$	6	44 ($K^+\pi^-$)	6.3 ± 1.5 [d]				
$\pi^- p \to \Lambda(1405) K^0$	4.5	43 ($\Sigma^\pm \pi^\mp$)	18 ± 3 [e]	32 ± 7	2.6 ± 0.4	0	2
$\pi^- p \to \Lambda(1520) K^0$	4.5	53 ($K^- p$)	26 ± 3.5 [e]	60 ± 13	2.3 ± 0.4	0	2
$\pi^- p \to \Sigma^0 K^0$	4.5	150	30 ± 2	186 ± 28	7.0 ± 1.0	0	0.4
$\pi^- p \to \Sigma^0 K^*(890)^0$	4.5	305 ($K^+\pi^-$)	26 ± 2 [c]	52 ± 8	2.1 ± 0.2	0.2	2.0
$\pi^- p \to \Sigma^0 K^*(1420)^0$	4.5	78 ($K^+\pi^-$)	5.5 ± 1.1 [d]				
$\pi^- p \to \Sigma(1385)^0 K^0$	4.5	94 ($\Lambda\pi^0$)	17 ± 2 [e]	29 ± 6	1.9 ± 0.3	0	2

[a] An alternative fit $d\sigma/dt = [(305 \pm 14)e^{(9\pm0.4)t'} + (28 \pm 2)e^{(1.6\pm0.1)t'}]\,\mu\text{b/GeV}^2$ for $t' < 2.0$ GeV^2 at 4.5 GeV/c.

[b] An alternative fit $d\sigma/dt = [(236 \pm 15)e^{(7.4\pm0.4)t'} + (4.4 \pm 1.2)e^{(1.0\pm0.3)t'}]\,\mu\text{b/GeV}^2$ for $t' < 2.0$ GeV^2 at 6 GeV/c.

[c] Corrected for the $K^0\pi^0$ decay mode.

[d] $K\pi$ decay mode only.

[e] Corrected for all decay modes.

were required also to lie within the fiducial volume used. Each accepted event was then weighted by the reciprocal of the detection probability. This correction was only significant and therefore applied to reactions (1a), (1b) and (4). To estimate the scanning efficiency, a subsample of the exposures was rescanned. The efficiency for topologies of interest was about 90%. Kinematic and geometric processing losses amounted to about 11% for one-V^0, about 15% for two-V^0, and about 19% for the two-prong plus V^0 topology.

The cross sections for the two-body and quasi-two-body channels discussed in this paper are summarized in Table I. The quoted errors are statistical. We estimate that the systematic errors could be as large as 10% for the 4.5-GeV/c data and 15% for the 6-GeV/c data. These cross sections have been corrected for unseen decay modes. In addition, the parameters for the forward differential cross section listed are obtained from least-squares fits to the expression

$$\frac{d\sigma}{dt'} = Ae^{bt'}$$

over the indicated ranges of $t' = t - t_0$ where t_0 is the minimum allowed momentum transfer squared.

III. $\pi^- p \to \Lambda K^0$ AND $\pi^- p \to \Sigma^0 K^0$

The center-of-mass angular distributions for $\pi^- p \to \Lambda K^0$ at 4.5 and 6.0 GeV/c and for $\pi^- p \to \Sigma^0 K^0$ at 4.5 GeV/c are shown in Figs. 2 and 3 and listed in Tables II, III, and IV. These distributions show both forward and backward peaks[1] ($\hat{\pi}^- \cdot \hat{K}^0 \approx \pm 1$). The differential cross sections and polarizations[2] P_Λ for reaction (1a) are presented in Figs. 4 and 5 and Tables V and VI and the differential cross section for reaction (1b) is shown in Fig. 6 and Table VII.

Reaction (1a) shows a clear break of slope at $t' \approx -0.4$ GeV^2 at 4.5 GeV/c. The data for reactions (1b) at 4.5 GeV/c and (1a) at 6.0 GeV/c also show a definite change of slope near the same t region. Results of fits to the differential cross sections are given in Table I. For reaction (1a) the Λ polarization is positive at small $|t'|$, crossing through zero for $t' \approx -0.45$ GeV^2 and becoming large and negative for larger values of $|t'|$. It should be noted that the polarization changes sign at the position of the break in the differential cross section,[1] a feature which is particularly clear in the 4.5-GeV/c data.

A. Remarks on $\pi^- p \to \Lambda K^0$

In the forward peripheral region the $\pi^- p \to \Lambda K^0$ reaction is expected to be dominated by the exchange of $K^*(890)$ and $K^*(1420)$, the only allowed known exchanges. The Regge-pole model relates $\pi^- p \to \Lambda K^0$ to the line-reversed reaction $\bar{K}^0 p \to \Lambda \pi^+$ and thus to the charge-symmetric $K^- n \to \Lambda \pi^-$.[3] The assumption of weak exchange degeneracy of $K^*(890)$ and $K^*(1420)$ $[\alpha_{K^*(890)}(t) = \alpha_{K^*(1420)}(t)$ where the α's

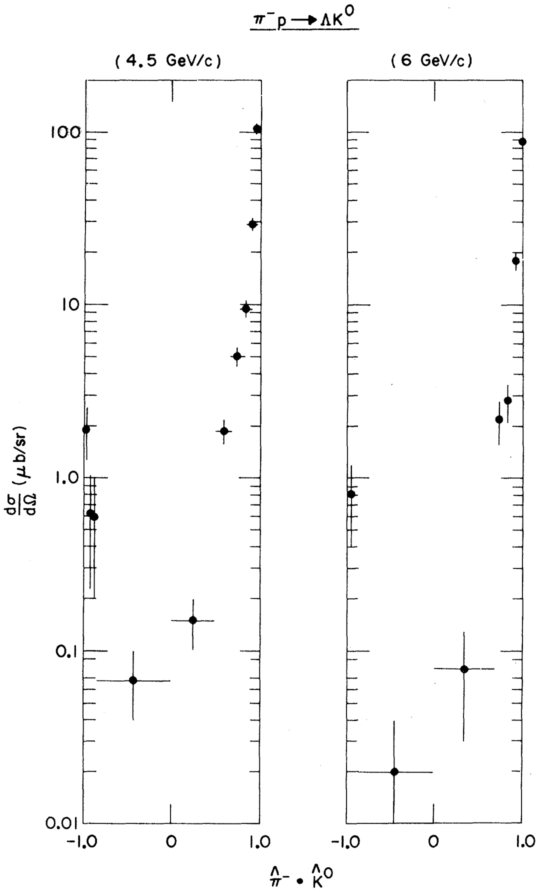

FIG. 2. Differential cross section for reaction (1a) vs center-of-mass production angle ($\hat{\pi}^- \cdot \hat{K}^0$) at 4.5 and 6 GeV/$c$.

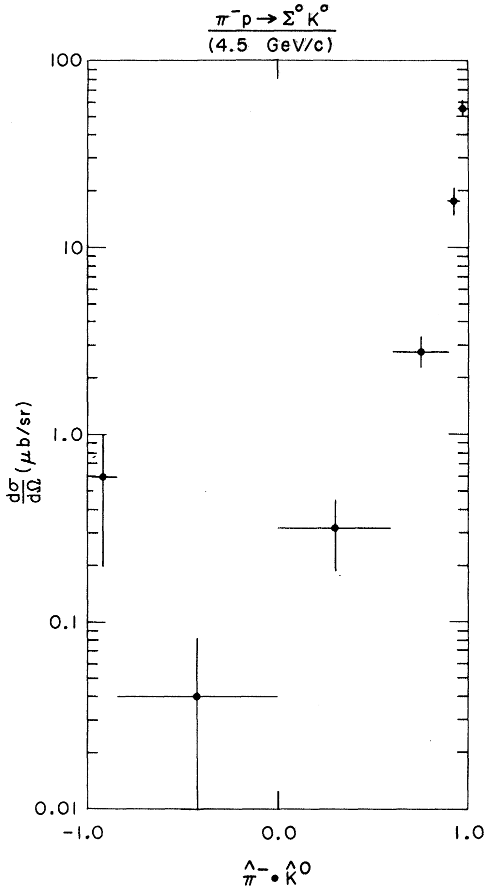

FIG. 3. Differential cross section for reaction (1b) at 4.5 GeV/c vs center-of-mass production angle ($\hat{\pi}^- \cdot \hat{K}^0$).

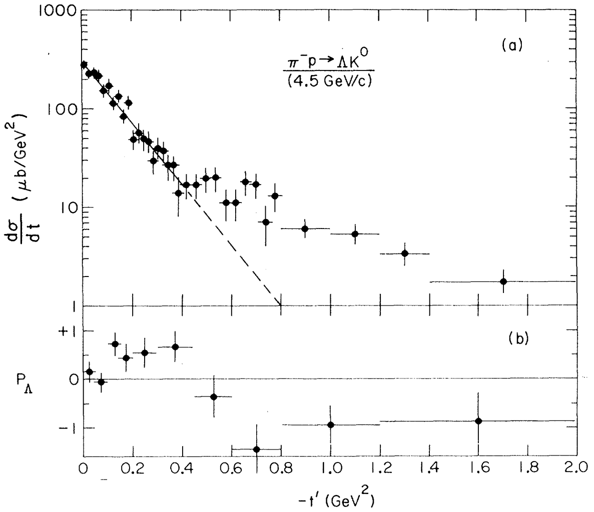

FIG. 4. Differential cross section and Λ polarization vs t' for reaction (1a) at 4.5 GeV/c. Solid line, indicating the fit (shown in Table I), is extended by the dashed line for reference.

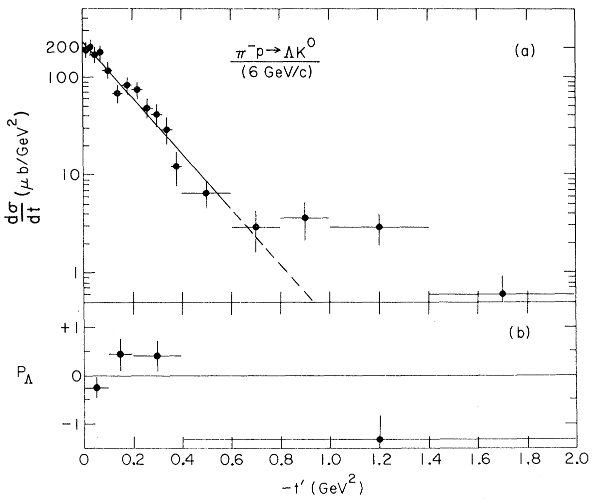

FIG. 5. Differential cross section and Λ polarization vs t' for reaction (1a) at 6.0 GeV/c. Solid line, indicating the fit (shown in Table I), is extended by the dashed line for reference.

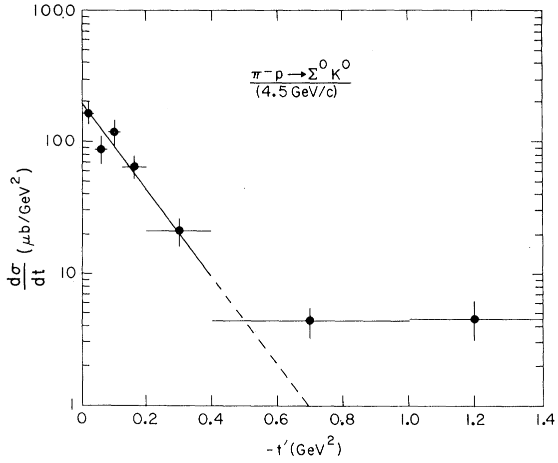

FIG. 6. Differential cross section vs t' for reaction (1b) at 4.5 GeV/c. Solid line, indicating the fit (shown in Table I), is extended by the dashed line for reference.

are the trajectory functions] predicts

$$\frac{d\sigma}{dt}(\pi^- p \to \Lambda K^0) = \frac{d\sigma}{dt}(K^- n \to \Lambda \pi^-)$$

and

$$P_\Lambda \frac{d\sigma}{dt}(\pi^- p \to \Lambda K^0) = -P_\Lambda \frac{d\sigma}{dt}(K^- n \to \Lambda \pi^-)\,.$$

In the case of strong exchange degeneracy [$\alpha_{K^*(890)}(t) = \alpha_{K^*(1420)}(t)$ and $\beta_{K^*(890)}(t) = \beta_{K^*(1420)}(t)$ where the β's are the real residues] the prediction is for zero Λ polarization.

The differential cross section and Λ polarization for the reaction $\pi^- p \to \Lambda K^0$ at 4.5 GeV/c is compared in Fig. 7 with that of $K^- n \to \Lambda \pi^-$ at 3.9 GeV/c, the best available data at a nearby energy.[3] The difference between the differential cross sections is significant. The polarizations are similar for $|t'| < 0.4$ GeV^2 but opposite in sign beyond this region. These observations are in direct contradiction with the simple predictions from either strong or weak exchange degeneracy.[4]

TABLE II. Differential cross section for $\pi^- p \to \Lambda K^0$ at 4.5 GeV/c.

Range of $\cos\theta^*$	$\frac{d\sigma}{d\Omega}$ (μb/sr)
1.0–0.99	146 ± 12
0.99–0.98	126 ± 11
0.98–0.97	100 ± 11
0.97–0.95	73 ± 6
0.95–0.9	28 ± 2
0.9–0.8	9.3 ± 1
0.8–0.7	4.9 ± 0.7
0.7–0.5	1.8 ± 0.3
0.5–0.0	0.15 ± 0.05
0.0– –0.85	0.07 ± 0.03
–0.85– –0.9	0.6 ± 0.4
–0.9– –0.95	0.6 ± 0.4
–0.95– –1.0	1.9 ± 0.6

TABLE III. Differential cross section for $\pi^- p \to \Lambda K^0$ at 6 GeV/c.

Range of $\cos\theta^*$	$\frac{d\sigma}{d\Omega}$ (μb/sr)
1.0–0.95	88 ± 6
0.95–0.9	18 ± 2.5
0.9–0.8	2.8 ± 0.7
0.8–0.7	2.2 ± 0.7
0.7–0.0	0.08 ± 0.05
0.0– –0.9	0.02 ± 0.02
–0.9– –1.0	0.8 ± 0.4

To explore all the available data[1,3] in these two classes of reactions ($\pi^- p \to \Lambda K^0$; and $K^- n \to \Lambda \pi^-$, $\bar{K}^0 p \to \Lambda \pi^+$, and $K^- p \to \Lambda \pi^0$) we show in Fig. 8 a compilation of the total cross sections for these reactions. Clearly, $\sigma(\bar{K}N \to \Lambda\pi)$ exceeds $\sigma(\pi^- p \to \Lambda K^0)$ by a factor of between 5 and 2 in the region of 2 to 5 GeV/c, a factor which is decreasing with increasing momentum. In addition, in Fig. 9 the slope b of the forward differential cross section is shown for these reactions. The mean values $\langle b_+ \rangle_{\pi^- p \to \Lambda K^0} = 7.15 \pm 0.25$ GeV^{-2} and $\langle b_- \rangle_{\bar{K}N \to \Lambda\pi} = 4.0 \pm 0.85$ GeV^{-2} differ appreciably. It is interesting to note, however, approximate equality of the differential cross section at $t' = 0$ for $\bar{K}N \to \Lambda\pi$ at 3.9 GeV/c and $\pi^- p \to \Lambda K^0$ at 4.5 GeV/c in Fig. 7. Our data as well as other data[1,3] indicate equality of the forward differential cross sections in the momentum range 3–6 GeV/c to the level of ~20%, a much closer agreement than shown by the integrated cross sections.

The effective trajectories $\alpha(t)$ for $\pi^- p \to \Lambda K^0$ and $\bar{K}N \to \Lambda\pi$ have been determined from available data[1,3] using the expression

$$\frac{d\sigma}{dt}(s,t) = f(t)\left(\frac{s-u}{2}\right)^{2\alpha(t)-2},$$

where s and u are the usual Mandelstam variables. The results for $\alpha(t)$ are shown in Fig. 10. The two reactions show quite different behavior. $\alpha(\pi^- p$

TABLE IV. Differential cross section for $\pi^- p \to \Sigma^0 K^0$ at 4.5 GeV/c.

Range of $\cos\theta^*$	$\frac{d\sigma}{d\Omega}$ (μb/sr)
1.0–0.95	55 ± 6
0.95–0.9	18 ± 3
0.9–0.6	2.8 ± 0.5
0.6–0.0	0.32 ± 0.13
0.0– –0.85	0.04 ± 0.04
–0.85– –1.0	0.6 ± 0.4

TABLE V. Differential cross section and Λ polarization for $\pi^-p \to \Lambda K^0$ at 4.5 GeV/c.

$-t'$ (GeV^2)	Visible events	$\frac{d\sigma}{dt'}$ (μb/GeV^2)
0.0–0.02	95	288 ± 30
0.02–0.04	79	229 ± 26
0.04–0.06	79	235 ± 26
0.06–0.08	78	218 ± 25
0.08–0.10	53	152 ± 21
0.10–0.12	60	170 ± 22
0.12–0.14	40	114 ± 18
0.14–0.16	45	134 ± 20
0.16–0.18	30	83 ± 15
0.18–0.20	38	114 ± 18
0.20–0.22	19	49 ± 11
0.22–0.24	19	57 ± 13
0.24–0.26	18	50 ± 12
0.26–0.28	16	47 ± 12
0.28–0.30	11	30 ± 9
0.30–0.32	14	40 ± 11
0.32–0.34	14	37 ± 10
0.34–0.36	10	27 ± 9
0.36–0.38	10	27 ± 9
0.38–0.40	5	14 ± 6
0.40–0.44	12	17 ± 5
0.44–0.48	12	17 ± 5
0.48–0.52	13	20 ± 6
0.52–0.56	13	20 ± 6
0.56–0.60	9	11 ± 4
0.60–0.64	8	11 ± 4
0.64–0.68	12	18 ± 5
0.68–0.72	12	17 ± 5
0.72–0.76	5	7 ± 3
0.76–0.80	10	13 ± 4
0.8–1.0	21	6 ± 1.3
1.0–1.2	21	5.3 ± 1.2
1.2–1.4	12	3.4 ± 0.9
1.4–2.0	17	1.7 ± 0.4

$-t'$ (GeV^2)	P_Λ
0.0–0.05	+0.14 ± 0.20
0.05–0.10	−0.04 ± 0.21
0.10–0.15	+0.73 ± 0.26
0.15–0.20	+0.45 ± 0.29
0.20–0.30	+0.56 ± 0.31
0.30–0.45	+0.67 ± 0.35
0.45–0.60	−0.36 ± 0.45
0.60–0.80	−1.44 ± 0.50
0.80–1.2	−0.94 ± 0.41
1.2–2.0	−0.88 ± 0.62

$\to \Lambda K^0$) is constant for $-t \lesssim 0.4$ GeV^2 indicating no shrinkage of the forward peak in the momentum range 2–6 GeV/c. On the other hand, $\alpha(\bar{K}N \to \Lambda\pi)$ is linear with a slope ~1.3 which indicates shrinkage of the forward peak. This accounts for the greater spread of $\langle b_- \rangle$ in Fig. 9.

In short, the notion of the simple ($K^*(890)$, $K^*(1420)$) exchange-degenerate Regge-pole model is significantly violated by the data available so far, with the possible exception of the very forward direction. In order to achieve fits to these reactions, Regge-Pomeranchukon cuts and daughter trajectories must be added to the simple model.[5] At this point the model loses much of its attractiveness. In spite of these difficulties it should be noted that for the reaction $\pi^-p \to \Lambda K^0$ the zero of the polarization near $t' \approx -0.45$ GeV^2 coincides with the zero of the effective trajectory which itself is close to the zero of a linear ($K^*(890)$, $K^*(1420)$) trajectory. This type of behavior, however, does not seem to occur for the $\bar{K}N \to \Lambda\pi$ reaction.

TABLE VI. Differential cross section and Λ polarization for $\pi^-p \to \Lambda K^0$ at 6 GeV/c.

$-t'$ (GeV^2)	Visible events	$\frac{d\sigma}{dt'}$ (μb/GeV^2)
0.00–0.02	32	188 ± 33
0.02–0.04	35	205 ± 35
0.04–0.06	29	171 ± 32
0.06–0.08	30	177 ± 32
0.08–0.12	39	115 ± 18
0.12–0.16	23	68 ± 14
0.16–0.20	28	82 ± 16
0.20–0.24	25	74 ± 15
0.24–0.28	16	48 ± 12
0.28–0.32	14	41 ± 11
0.32–0.36	10	29 ± 9
0.36–0.40	4	12 ± 5.5
0.40–0.60	11	6.5 ± 1.9
0.60–0.80	5	2.9 ± 1.3
0.80–1.00	6	3.6 ± 1.5
1.00–1.4	10	2.9 ± 1.0
1.4–2.0	3	0.6 ± 0.4

$-t'$ (GeV^2)	P_Λ
0.0–0.1	−0.25 ± 0.22
0.1–0.2	+0.44 ± 0.35
0.2–0.4	+0.41 ± 0.31
0.4–2.0	−1.35 ± 0.48

TABLE VII. Differential cross section and Λ polarization for $\pi^-p \to K^0\Sigma^0$ at 4.5 GeV/c.

$-t'$ (GeV^2)	Visible events	$\frac{d\sigma}{dt}$ (μb/GeV^2)
0–0.04	32	161 ± 29
0.04–0.08	17	85 ± 21
0.08–0.12	23	116 ± 25
0.12–0.2	25	63 ± 13
0.2–0.4	21	21 ± 5
0.4–1.0	13	4.4 ± 1.2
1.0–1.4	9	4.5 ± 1.5
1.4–2.0	2	0.7 ± 0.5

$-t'$ (GeV^2)	P_Σ
0–0.4	0.59 ± 0.41

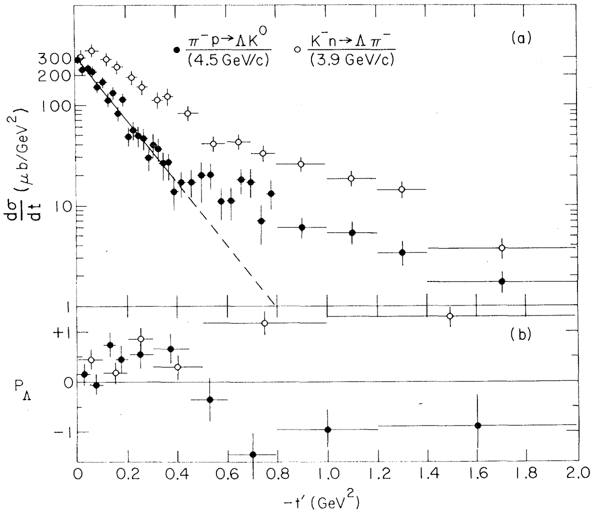

FIG. 7. Comparison of differential cross sections and Λ polarizations vs t' for the reactions $K^-n\to\Lambda\pi^-$ at 3.9 GeV/c to those of the reaction $\pi^-p\to\Lambda K^0$ at 4.5 GeV/c. The solid line, indicating the fit shown in Table I, is extended by the dashed line for reference.

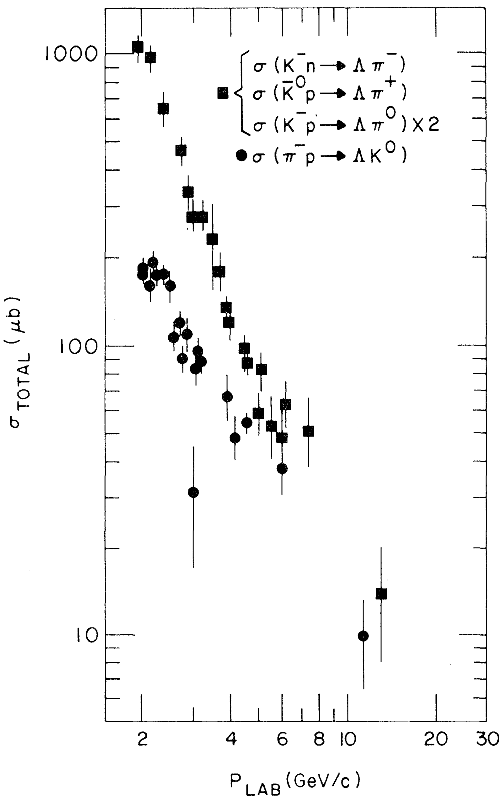

FIG. 8. Comparison of the total cross sections for the various $\bar{K}N\to\Lambda\pi$ reactions to the total cross section of the reaction $\pi^-p\to\Lambda K^0$ as a function of the laboratory momentum of the incident particle, P_{lab}. The data are from Refs. 1 and 3.

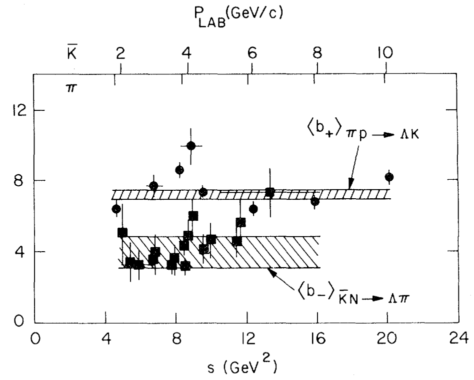

FIG. 9. Comparison of the forward slope (b_-) of the differential cross section for the reaction $\bar{K}N\to\Lambda\pi$ (shown by squares) to the forward slope (b_+) for the reaction $\pi^-p\to\Lambda K^0$ (shown by circles) as a function of s – the total center-of-mass energy squared. The shaded regions show the weighted averages of b plus and minus 1 standard deviation. The data are from Refs. 1 and 3.

B. Remarks on $\pi^-p\to\Sigma^0K^0$

We compare the reaction $\pi^-p\to\Sigma^0K^0$ to $\pi^+p\to\Sigma^+K^+$ to determine whether any $a_{3/2}$, isospin-$\frac{3}{2}$ amplitude [in addition to the $a_{1/2}$, $I=\frac{1}{2}K^*(890), K^*(1420)$ exchange] might exist in the t-channel exchange when a Σ hyperon is involved in the final state. This may be done by comparing reaction (1b) with the reaction $\pi^+p\to\Sigma^+K^+$. The ratio of cross sections is

$$R\left[\frac{\sigma(\pi^+p\to\Sigma^+K^+)}{\sigma(\pi^-p\to\Sigma^0K^0)}\right]=\frac{|a_{3/2}|^2+4|a_{1/2}|^2+4\,\mathrm{Re}(a_{3/2}^*a_{1/2})}{2|a_{3/2}|^2+2|a_{1/2}|^2-4\,\mathrm{Re}(a_{3/2}^*a_{1/2})}.$$

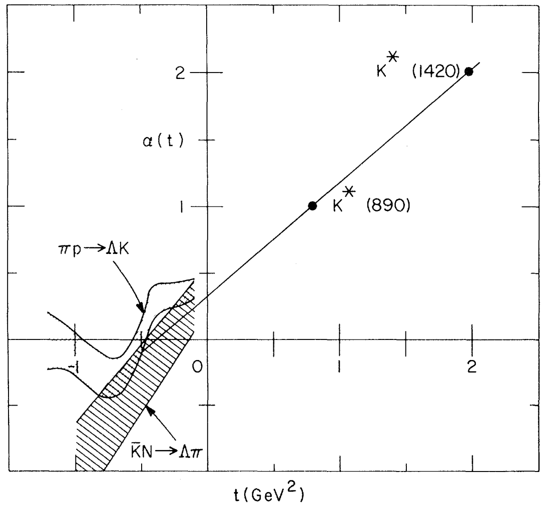

FIG. 10. Chew-Frautschi plot of the $K^*(890)$ and $K^*(1420)$ trajectory. Shaded regions show experimental determination of the effective trajectories extracted from data for the reactions $\pi^-p\to\Lambda K^0$ and $\bar{K}N\to\Lambda\pi$. See text for details.

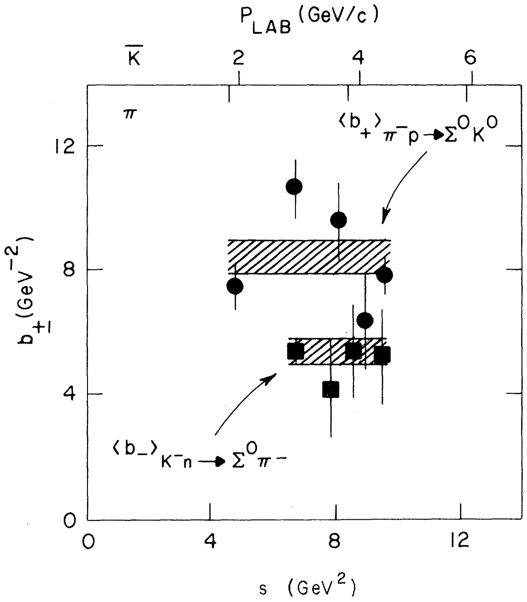

FIG. 11. Comparison of the forward slope (b_+) of the differential cross section for the reaction $\pi^- p \to \Sigma^0 K^0$ (shown by circles) to the forward slope (b_-) for the reaction $K^- n \to \Sigma^0 \pi^-$ (shown by squares). The shaded regions show the weighted averages of b plus and minus 1 standard deviation. The data are from Refs. 1 and 3.

$R = 2$ if only the $a_{1/2}$ amplitude is present. Therefore any deviation of the value of R different from 2 indicates the presence of the $a_{3/2}$ amplitude. The differential cross section for $\pi^+ p \to \Sigma^+ K^+$ at 4.5 GeV/c for this comparison comes from an interpolation of the Michigan-Argonne data which are measured at momenta between 3 and 7 GeV/c.[6] We obtained a weighted average of the ratio R to be 1.9 ± 0.2 for $|t'| < 1$ GeV^2. This is consistent with no $I = \frac{3}{2}$ present in the t-channel exchange for $\pi^- p \to \Sigma^0 K^0$ and $\pi^+ p \to \Sigma^+ K^+$ at 4.5 GeV/c.

Similar arguments concerning the ($K^*(890)$, $K^*(1420)$) exchange degeneracy can also be applied here with the $\pi^- p \to \Sigma^0 K^0$ and the line-reversed reaction $\bar{K}^0 p \to \Sigma^0 \pi^+$ or $K^- n \to \Sigma^0 \pi^-$. Limited date from this experiment as well as others preclude a detailed examination as done for the $\pi^- p \to \Lambda K^0$ and $\bar{K}N \to \Lambda\pi$ in Sec. III A. However, a similar disparity between $\pi^- p \to \Sigma^0 K^0$ and $K^- n \to \Sigma^0 \pi^-$ seems to exist, as can be illustrated in the slope parameter $b_\pm$ for the Σ^0 final states (Fig. 11).[1,3]

At $t' \sim 0$, the ratio of

$$\frac{d\sigma}{dt'}(\pi^- p \to \Sigma^0 K^0) \Big/ \frac{d\sigma}{dt'}(\pi^- p \to \Lambda K^0) = 0.59 \pm 0.09\ .$$

Since the spin-flip amplitude contribution is negligible at $t' \sim 0$, the ratio can be related[7] to spin-nonflip contributions as follows:

$$\left[\frac{\frac{d\sigma}{dt'}(\pi^- p \to \Sigma^0 K^0)}{\frac{d\sigma}{dt'}(\pi^- p \to \Lambda^0 K^0)}\right]_{t \sim 0} = \left[\frac{f_{++}^{\Sigma^0}}{f_{++}^{\Lambda}}\right]^2 = \frac{g_\Sigma^{\ 2}}{g_\Lambda^{\ 2}}$$

$$= 3\left[\frac{1 - D/F}{3 + D/F}\right]^2 .$$

The D/F ratio for $\bar{p}K^*\Sigma^0$ and $\bar{p}K^*\Lambda$ can be estimated where K^* represents both $K^*(890)$ and $K^*(1420)$. The values of D/F are -0.24 ± 0.06 or 4.2 ± 0.4.

The Σ^0 polarization[8] for $|t'| < 0.4$ GeV^2 is (+) 0.59 ± 0.41. This can be compared with the Λ polarization in $\pi^- p \to \Lambda K^0$ for the same t range which is $+0.50 \pm 0.05$. Thus Σ^0 and Λ polarization appear to be the same sign and approximately equal in magnitude.

IV. THE QUASI-TWO-BODY REACTIONS $\pi^- p \to \Lambda K^*(890)^0$ AND $\Sigma^0 K^*(890)^0$

Much attention has been paid to two-body and quasi-two-body reactions. Various competing models have been applied to the description of differential cross sections and decay distributions in the peripheral region.[9] Although some apparent success has been obtained, competing models frequently predict radically different behavior of the helicity amplitudes.[10] The complete elucidation of these amplitudes can only be accomplished using a polarized target. However, in reactions such as $\pi^- p \to \Lambda K^*(890)^0$ and $\Sigma^0 K^*(890)^0$ where the final baryon polarization is easily measured, study of the combined decay distributions of Λ and $K^*(890)^0$ can lead, under favorable circumstances, to strong constraints on the behavior of the helicity amplitudes.

A. General Features of $\pi^- p \to \Lambda K^+ \pi^-$ and $\pi^- p \to \Sigma^0 K^+ \pi^-$

The general features of these reactions are shown in the Dalitz plots and effective-mass plots of Figs. 12–17, and the Chew-Low plots of Figs. 18–20. The dominant feature is the strong forward peripheral and marked backward $K^*(890)^0$ production appearing in all cases; $K^*(1420)^0$ is also clearly present in the $\Lambda K^+ \pi^-$ final state. The center-of-mass angular distributions of $\Lambda K^*(890)^0$ and $\Sigma^0 K^*(890)^0$ at 4.5 GeV/c are shown in Fig. 21 and Table VIII. In the $\Lambda K^+ \pi^-$ channel the $N^*(1700) \to \Lambda K^+$ enhancement is observed at both energies.[11] The shaded area in the ΛK^+ mass spectra is for the events remaining after removal of the $K^*(890)^0$ events (0.79–0.99 GeV) and illustrates the absence of overlap between this $N^*(1700)$ and the $K^*(890)^0$.

There are 1259 and 372 events from the final

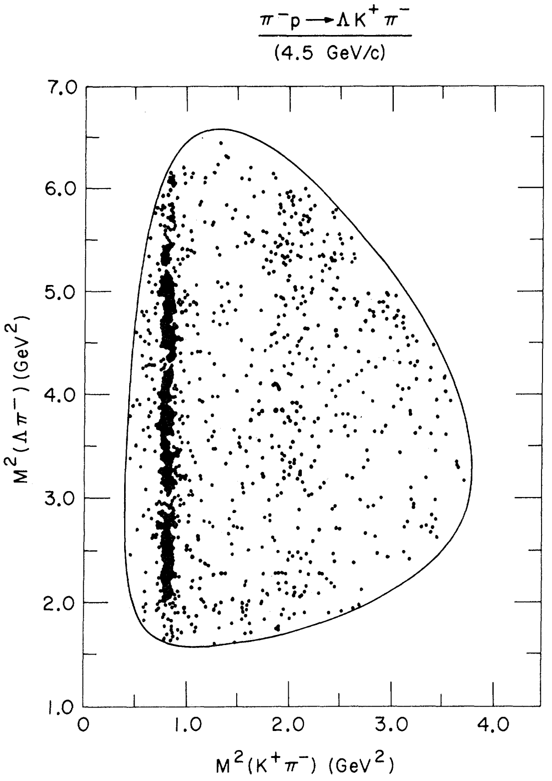

FIG. 12. Dalitz plot for the $\Lambda K^+\pi^-$ final state at 4.5 GeV/c.

state $\Lambda K^+\pi^-$ at 4.5 and 6 GeV/c, respectively, and 567 events from the final state $\Sigma^0 K^+\pi^-$ at 4.5 GeV/c for our analysis in this section.

We now turn to discussion of the quasi-two-body reactions

$$\pi^- p \to \Lambda K^*(890)^0 , \qquad (2a)$$

$$\pi^- p \to \Sigma^0 K^*(890)^0 , \qquad (2b)$$

which dominate the $\pi^- p \to \Lambda K^+\pi^-$ and $\pi^- p \to \Sigma^0 K^+\pi^-$ reactions.

B. $\pi^- p \to \Lambda K^*(890)^0$ at 4.5 GeV/c

Differential cross sections and polarizations for this reaction are shown in Fig. 22 and presented in Table IX. Relevant cross sections and slope parameters are presented in Table I. Because of the small background (~8%) in the $K^*(890)^0$ mass region, the differential cross section obtained from taking all events in the mass range (0.79–0.99 GeV) is indistinguishable from that obtained from fitting the mass spectra to a Breit-Wigner resonance shape plus a linear background for different regions of t'. The differential cross section is less steep ($b = 2.5 \pm 0.2$ GeV^{-2}) than the $\pi^- p \to \Lambda K^0$ reaction. One obvious feature of the differential cross section is a flattening effect in the forward region ($0 < |t'| < 0.1$ GeV^2). The Λ polarization is consistent with zero up to $|t'| \sim 0.4$ GeV^2 and then becomes large and negative. We will examine the significance of these observations after presentation of the density-matrix elements of the $K^*(890)^0$.

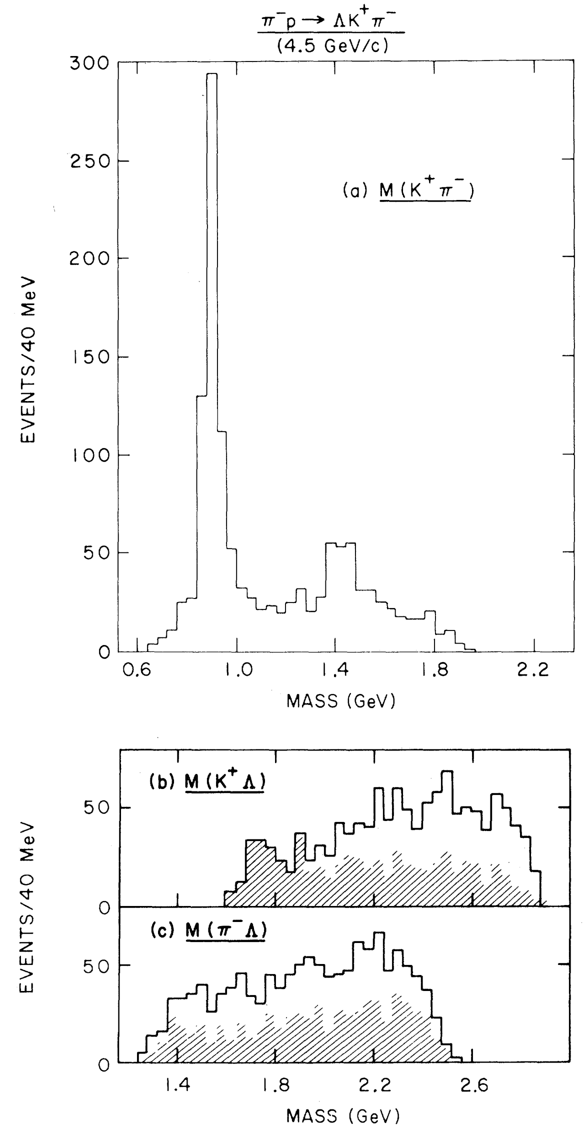

FIG. 13. Mass projections for the $\Lambda K^+\pi^-$ final state at 4.5 GeV/c. Shaded regions indicate events outside $K^*(890)^0$ region $[0.79 < M(K^+\pi^-) < 0.99$ GeV].

The $\Lambda K^*(890)^0$ double density-matrix elements are determined for the $K^*(890)^0$ mass interval by the method of moments. The angular distribution for this case is[12]

$$W(\theta, \varphi, \theta', \varphi') = \frac{1}{4\pi}\left[W_{K^*}(\theta, \varphi) + W_\Lambda(\theta', \varphi') - \tfrac{1}{4}\pi\right] + \frac{3\alpha_\Lambda}{16\pi^2} C , \qquad (8)$$

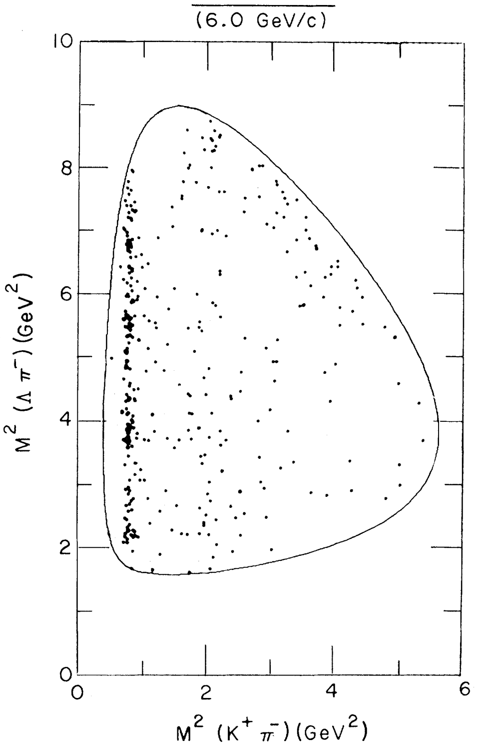

FIG. 14. Dalitz plot for the $\Lambda K^+\pi^-$ final state at 6.0 GeV/c.

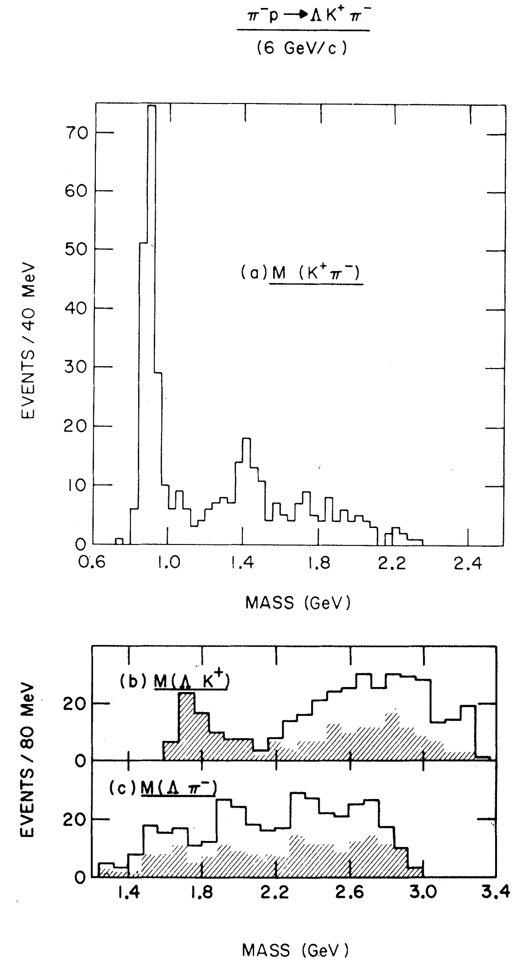

FIG. 15. Mass projections for the $\Lambda K^+\pi^-$ final state at 4.5 GeV/c. Shaded regions indicate events outside $K^*(890)^0$ region $[0.79 < M(K^+\pi^-) < 0.99$ GeV].

where the single decay distributions are

$$W_{K^*}(\theta,\varphi)=\frac{3}{4\pi}\left[\tfrac{1}{3}+(\cos^2\theta-\tfrac{1}{3})(\rho_{00}-\rho_{11})\right.$$
$$-\sqrt{2}\,\mathrm{Re}\rho_{10}\sin 2\theta\cos\varphi$$
$$\left.-\rho_{1\,-1}\sin^2\theta\cos 2\varphi\right] \tag{9}$$

and

$$W_\Lambda(\theta',\varphi')=\frac{1}{4\pi}(1+2\alpha_\Lambda\mathrm{Im}\rho_{+-}\sin\theta'\sin\varphi') \tag{10}$$

where we use $\alpha_\Lambda = +0.645$ and subscripts ± refer to the Λ helicity.[13] The correlation terms are given by

$$C=\sin\theta'\sin\varphi'[2(\mathrm{Im}\rho^{00}_{+-}-\mathrm{Im}\rho^{11}_{+-})(\cos^2\theta-\tfrac{1}{3})]$$
$$-\sin\theta'\sin\varphi'[(\mathrm{Im}\rho^{1\,-1}_{+\,-}-\mathrm{Im}\rho^{1\,-1}_{-\,+})\sin^2\theta\cos 2\varphi-\sqrt{2}(\mathrm{Im}\rho^{10}_{+-}-\mathrm{Im}\rho^{10}_{-+})\sin 2\theta\cos\varphi]$$
$$-\sin\theta'\cos\varphi'[(\mathrm{Im}\rho^{1\,-1}_{+\,-}+\mathrm{Im}\rho^{1\,-1}_{-\,+})\sin^2\theta\sin^2\varphi+\sqrt{2}(\mathrm{Im}\rho^{10}_{+-}+\mathrm{Im}\rho^{10}_{-+})\sin 2\theta\sin\varphi]$$
$$-\cos\theta'[2\,\mathrm{Im}\rho^{1\,-1}_{+\,+}\sin^2\theta\sin 2\varphi+\sqrt{2}\,(\mathrm{Im}\rho^{10}_{++}-\mathrm{Im}\rho^{10}_{--})\sin 2\theta\sin\varphi]\,. \tag{11}$$

This distribution, with 11 measurable quantities plus $d\sigma/dt$, applies equally to the s- and t-channel frames. The direction of the normal to the production plane, $\hat{Y}$, is defined as $\hat{\pi}^-\times\hat{K}^*(890)^0$, or equivalently, $\hat{p}\times\hat{\Lambda}$. For the t-channel frame the z direction is defined as the π^- [p] direction in the $K^*(890)^0$ [Λ] rest frame for description of the $K^*(890)^0$ [Λ] decay. For the s-channel frame the z direction is opposite to the Λ [$K^*(890)^0$] direction in the $K^*(890)^0$ [Λ] rest frame. The π^- has been used to define the Λ-decay direction. Thus we can determine 11 combinations of density-matrix elements which are shown in Figs. 23–25 and listed in Tables IX–XII. No attempt has been made to constrain the values of the density-matrix elements within their allowed ranges. However, the positivity conditions on the density matrix are satisfied to the level expected from the statistics.

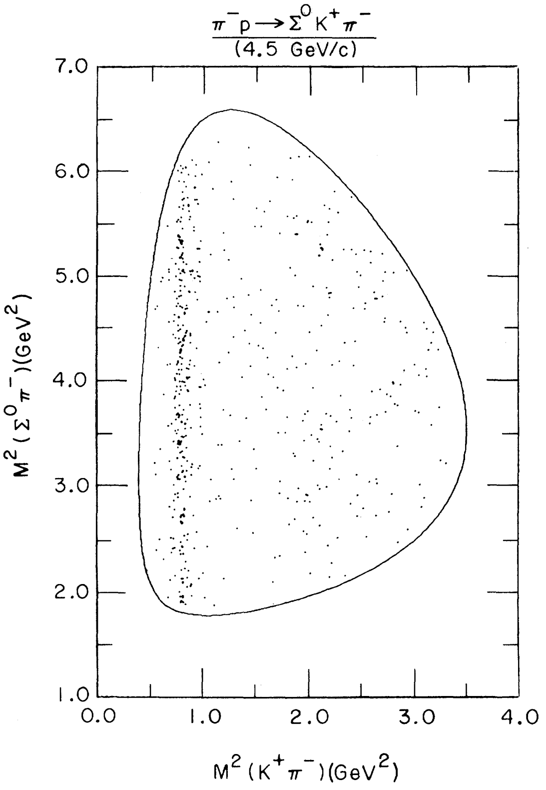

FIG. 16. Dalitz plot for the $\Sigma^0 K^+\pi^-$ final state at 4.5 GeV/*c*.

We now consider the interpretation of this data. Following the method of Byers and Yang,[14] we define linear combinations of the helicity amplitudes $F^{\mu}_{\lambda\lambda'}$ where λ, λ', and μ are helicity indices for proton, Λ, and $K^*(890)^0$ respectively. For either s- or t-channel frame,

$$A_\pm = \frac{F^0_{++} \mp iF^0_{+-}}{\sqrt{2}}, \quad B_\pm = \frac{F^1_{++} \mp iF^1_{+-}}{\sqrt{2}}, \quad C_\pm = \frac{F^{-1}_{++} \mp iF^{-1}_{+-}}{\sqrt{2}}, \tag{12}$$

and further

$$S_\pm = \frac{B_\pm + C_\pm}{\sqrt{2}}, \quad D_\pm = \frac{B_\pm - C_\pm}{\sqrt{2}}.$$

$F^{\mu}_{\lambda\lambda'}$ are related to the double and single density-matrix elements and differential cross sections as follows:

$$\rho^{\mu\mu'}_{\lambda\lambda'} = \Big(\sum_{\nu} F^{\mu}_{\nu\lambda} F^{\mu'*}_{\nu\lambda'}\Big)\Big/\frac{d\sigma}{dt}$$

and (13)

$$\rho_{\mu\mu'} = \sum_{\lambda} \rho^{\mu\mu'}_{\lambda\lambda} = \Big(\sum_{\nu\lambda} F^{\mu}_{\nu\lambda} F^{\mu'*}_{\nu\lambda}\Big)\Big/\frac{d\sigma}{dt}.$$

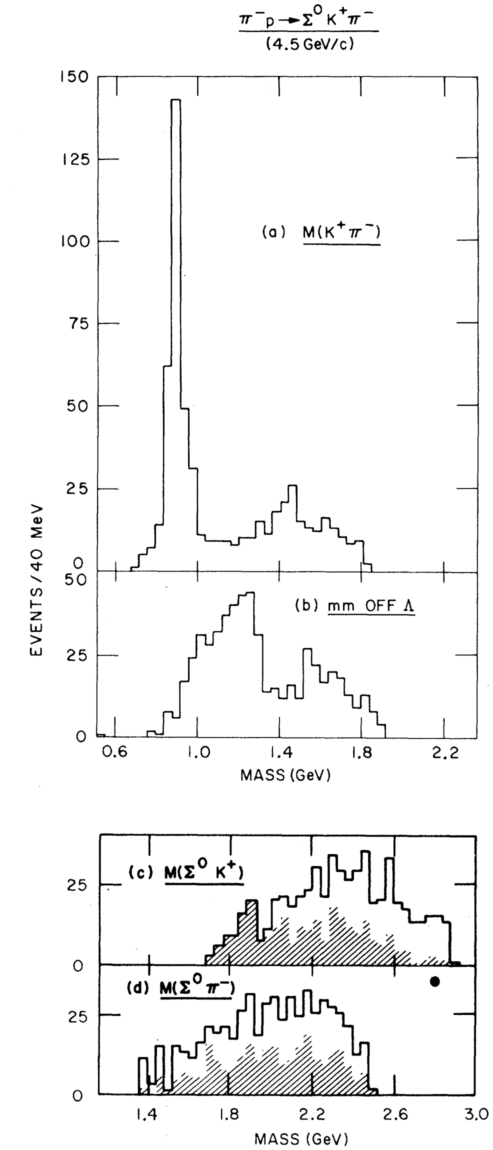

FIG. 17. (a), (c), and (d) are mass projections for the $\Sigma^0 K^+\pi^-$ final state at 4.5 GeV/*c*. Shaded regions indicate events outside $K^*(890)^0$ region $[0.79 < M(K^+\pi^-) < 0.99$ GeV]. (b) The missing mass recoiling from the Λ.

We can express six measurable quantities [from Eqs. (9), (10), and (11)] in terms of $A_\pm^2$, $S_\pm^2$, and $D_\pm^2$ as follows:

$$\frac{d\sigma}{dt} = A_+^2 + A_-^2 + S_+^2 + S_-^2 + D_+^2 + D_-^2,$$

$$(\rho_{00} - \rho_{11})\frac{d\sigma}{dt} = A_+^2 + A_-^2 - \tfrac{1}{2}(S_+^2 + S_-^2 + D_+^2 + D_-^2),$$

$$\rho_{1-1}\frac{d\sigma}{dt} = \tfrac{1}{2}(S_+^2 + S_-^2 - D_+^2 - D_-^2),$$

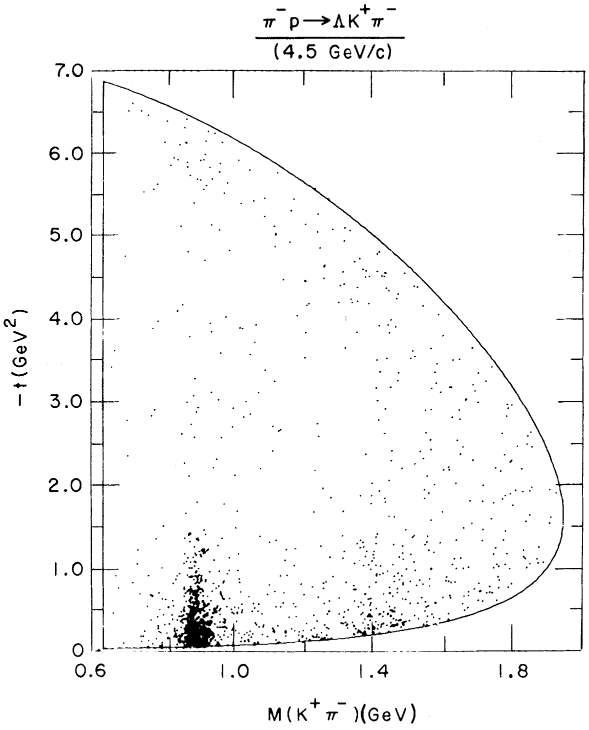

FIG. 18. Chew-Low plot for reaction $\pi^- p \rightarrow \Lambda K^+ \pi^-$ at 4.5 GeV/c.

$$-P_\Lambda \frac{d\sigma}{dt} = 2\,\mathrm{Im}\rho_{+-}\frac{d\sigma}{dt} = A_-^{\,2} - A_+^{\,2} + S_-^{\,2} - S_+^{\,2} + D_-^{\,2} - D_+^{\,2}, \qquad (14)$$

$$2(\mathrm{Im}\rho_{+-}^{00} - \mathrm{Im}\rho_{+-}^{11})\frac{d\sigma}{dt} = A_-^{\,2} - A_+^{\,2} - \tfrac{1}{2}(S_-^{\,2} - S_+^{\,2} + D_-^{\,2} - D_+^{\,2}),$$

$$(\mathrm{Im}\rho_{+-}^{1\,-1} - \mathrm{Im}\rho_{-+}^{1\,-1})\frac{d\sigma}{dt} = \tfrac{1}{2}(S_-^{\,2} - S_+^{\,2} + D_+^{\,2} - D_-^{\,2}).$$

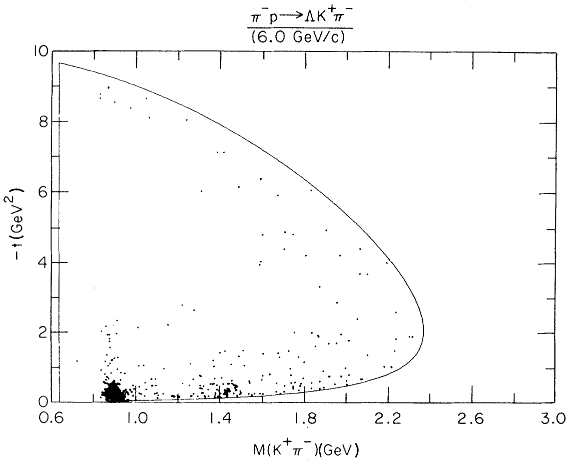

FIG. 19. Chew-Low plot for reaction $\pi^- p \rightarrow \Lambda K^+ \pi^-$ at 6.0 GeV/c.

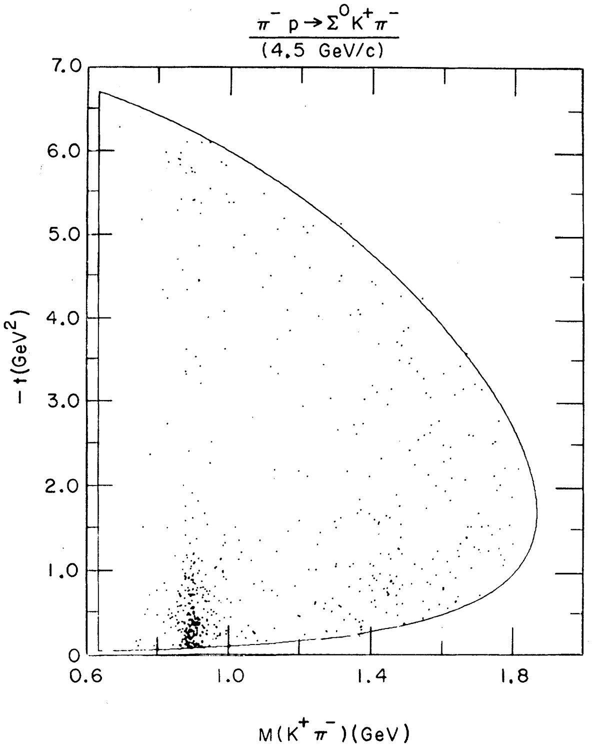

FIG. 20. Chew-Low plot for reaction $\pi^- p \rightarrow \Sigma^0 K^+ \pi^-$ at 4.5 GeV/c.

From these six equations, one can experimentally determine the six unknowns ($A_\pm^{\,2}$, $S_\pm^{\,2}$, and $D_\pm^{\,2}$). First, it is instructive to express these six un-

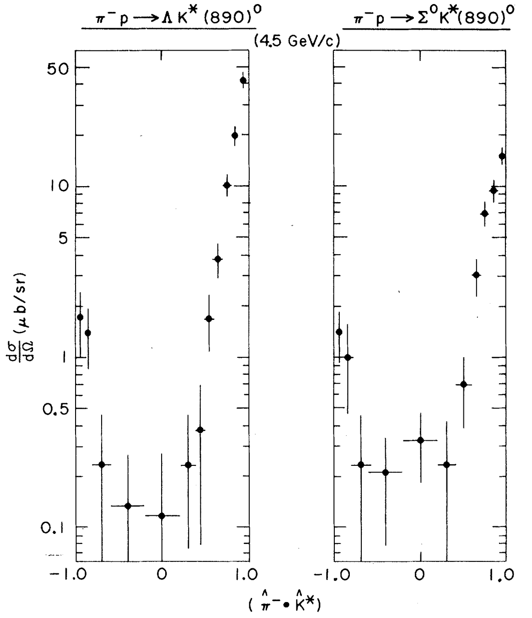

FIG. 21. Differential cross sections vs center-of-mass production angle $[\hat{\pi}^- \cdot \hat{K}^*(890)^0]$ for reactions (2a) and (2b) at 4.5 GeV/c.

TABLE VIII. Differential cross sections for $\pi^- p \to \Lambda K^*(890)^0$ and $\pi^- p \to \Sigma^0 K^*(890)^0$ at 4.5 GeV/c.

Range of $\cos\theta^*$	$d\sigma/d\Omega[\pi^- p \to \Lambda K^*(890)^0]$ (μb/sr)	$d\sigma/d\Omega[\pi^- p \to \Sigma^0 K^*(890)^0]$ (μb/sr)
1.0–0.9	42 ± 4	15.0 ± 1.7
0.9–0.8	20 ± 2	9.5 ± 1.1
0.8–0.7	10 ± 1.5	7.0 ± 1.0
0.7–0.6	3.8 ± 0.9	3.1 ± 0.7
0.6–0.5	1.7 ± 0.7	0.7 ± 0.3
0.5–0.4	0.38 ± 0.32	
0.4–0.2	0.24 ± 0.24	0.24 ± 0.18
0.2– –0.2	0.12 ± 0.15	0.33 ± 0.14
–0.2– –0.6	0.13 ± 0.14	0.21 ± 0.13
–0.6– –0.8	0.24 ± 0.24	0.23 ± 0.24
–0.8– –0.9	1.4 ± 0.6	1.0 ± 0.6
–0.9– –1.0	1.7 ± 0.7	1.4 ± 0.5

knowns as

$$A_\pm{}^2 = \rho_\pm^{00}\frac{d\sigma}{dt}, \quad S_\pm{}^2 = (\rho_\pm^{11} + \rho_\pm^{1\,-1})\frac{d\sigma}{dt},$$
$$D_\pm{}^2 = (\rho_\pm^{11} - \rho_\pm^{1\,-1})\frac{d\sigma}{dt}, \tag{15}$$

where the lower index of $\rho_\pm^{\mu\mu'}$ indicates the Λ spin with respect to the production plane normal (*not* the helicity index as for $\rho_{\lambda\lambda'}^{\mu\mu'}$). Note that $S_\pm{}^2$ and $(A_\pm{}^2 + D_\pm{}^2)$ are invariant under rotation about the production plane normal. To the extent that absorptive effects are not dominant, the quantity $A_\pm{}^2$ has only unnatural-parity-exchange contributions, and $S_\pm{}^2$ and $D_\pm{}^2$ correspond approximately to natural- and unnatural-parity exchanges, respectively.[15]

Figure 26 shows the experimentally determined values of $A_\pm{}^2$, $D_\pm{}^2$, and $S_\pm{}^2$ for the t-channel frame. In this frame only $A_+{}^2$ and $S_-{}^2$ are dominant throughout a wide range of $|t'|$. This is not the case for the s-channel frame where $A_+{}^2$ and $D_+{}^2$ and $S_-{}^2$ are *all* important (not shown).[16] Consequently in the following, we consider only the t-channel frame, since the dominance of only two quantities, $A_+{}^2$ and $S_-{}^2$, for $|t'| < 0.8$ GeV^2 leads to a simpler interpretation of the data in this frame. This behavior in the t-channel frame indicates that the contributions from the $\mu = 0$ and $\mu = \pm 1$ amplitudes give near maximal, but opposite, contributions to the Λ polarization. Thus the net Λ polarization is found to be small for $|t'| < 0.4$ GeV^2 where the two contributions cancel. For $|t'| > 0.4$ GeV^2 the faster decrease of $A_+{}^2$ with $|t'|$ leads to a large negative Λ polarization as seen in Fig. 22. To illustrate this effect, we divide the data with respect to the Gottfried-Jackson angle θ in the $K^*(890)^0$ rest frame to enhance the $A_+{}^2$ (unnatural contributions) and the $S_-{}^2$ (natural contributions) by selecting $|\cos\theta| > 0.8$ and $|\cos\theta| < 0.4$, respectively, and plot the corresponding Λ-decay distributions as shown in Figs. 27(a) and 27(c). It is evident, in these two regions that the strong Λ polarizations are opposite in sign, whereas in the transition region ($0.4 < |\cos\theta| < 0.8$) the Λ polarization is zero as shown in Fig. 27(b). The over-all Λ polarization ($0 \leqslant |\cos\theta| \leqslant 1$) as shown in Fig. 27(d) is small and consistent with zero.

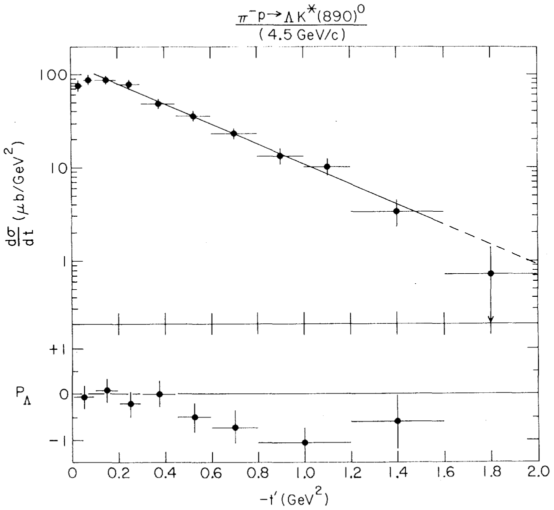

FIG. 22. Differential cross section and Λ polarization for reaction (2a) at 4.5 GeV/c. Solid line, indicating the fit shown in Table I, is extended by the dashed line for reference.

To be more specific, we make the following three conclusions in the t channel for the region $|t'| < 0.8$ GeV^2 where $A_+{}^2$ and $S_-{}^2$ are dominant:

1. $A_+{}^2 \gg A_-{}^2$. This requires $F_{++}^0 \simeq -iF_{+-}^0$ from Eq. (12) (approximate equality in magnitude with a relative phase of ~90°) which implies a near maximal positive Λ-polarization contribution of the $\mu = 0$ amplitudes. This is the effect illustrated in Fig. 27(a).

2. $S_-{}^2 \gg S_+{}^2$ *and* $S_-{}^2 \gg D_\pm{}^2$. This requires

TABLE IX. Differential cross section, Λ polarization, and density-matrix elements for $\pi^-p \rightarrow \Lambda K^*(890)^0$ at 4.5 GeV/*c*.

Range of $-t'$ (GeV^2)	$d\sigma/dt$ (μb/GeV^2)	P_Λ	t channel ρ_{00}	t channel $\rho_{1\,-1}$	t channel Reρ_{10}	s channel ρ_{00}	s channel $\rho_{1\,-1}$	s channel Reρ_{10}
0–0.05	77.0 ± 11	−0.11 ± 0.28	0.40 ± 0.08	0.18 ± 0.06	−0.02 ± 0.05	0.37 ± 0.08	0.16 ± 0.06	0.06 ± 0.05
0.05–0.1	87.0 ± 12							
0.1–0.2	86.7 ± 8.5	0.09 ± 0.28	0.42 ± 0.07	0.25 ± 0.06	−0.04 ± 0.04	0.26 ± 0.07	0.17 ± 0.06	0.14 ± 0.04
0.2–0.3	78.4 ± 8.1	−0.16 ± 0.26	0.26 ± 0.08	0.29 ± 0.07	0.03 ± 0.04	0.08 ± 0.07	0.20 ± 0.07	0.04 ± 0.04
0.3–0.45	48.2 ± 5.2	−0.04 ± 0.29	0.26 ± 0.08	0.26 ± 0.06	−0.02 ± 0.05	0.16 ± 0.07	0.20 ± 0.08	0.03 ± 0.05
0.45–0.6	35.7 ± 4.5	−0.50 ± 0.35	0.15 ± 0.08	0.29 ± 0.08	0.08 ± 0.05	0.10 ± 0.07	0.26 ± 0.08	−0.07 ± 0.05
0.6–0.8	23.0 ± 3.0	−0.68 ± 0.38	0.15 ± 0.09	0.25 ± 0.09	0.06 ± 0.06	0.16 ± 0.09	0.25 ± 0.09	−0.06 ± 0.06
0.8–1.0	13.0 ± 2.5	−1.06 ± 0.34	0.24 ± 0.09	0.07 ± 0.09	0.07 ± 0.07	0.35 ± 0.11	0.12 ± 0.08	−0.06 ± 0.06
1.0–1.2	10.0 ± 2							
1.2–1.6	3.3 ± 1.0	−0.6 ± 0.6	0.0 ± 0.15	0.0 ± 0.2	−0.05 ± 0.10	0.45 ± 0.20	0.20 ± 0.10	0.20 ± 0.10
1.6–2.0	0.7 ± 0.7	···	···	···	···	···	···	···

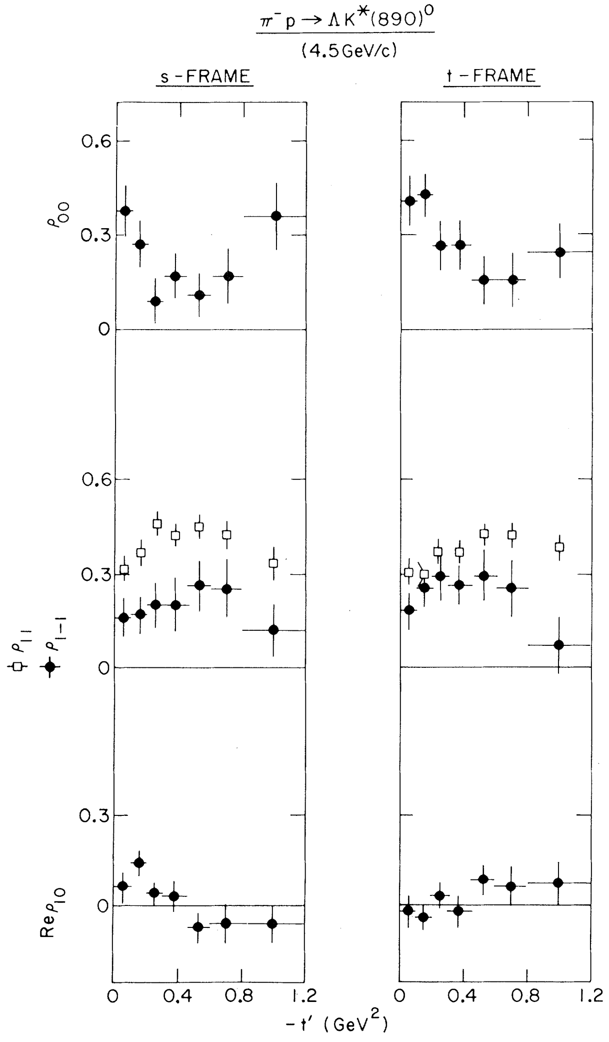

FIG. 23. Single density-matrix elements vs t' for events in the $K^*(890)^0$ region $[0.79 < M(K^+\pi^-) < 0.99$ GeV$]$ from reaction (2a) at 4.5 GeV/*c*.

$(B_- \simeq C_-) \gg B_+$ or C_+ from Eq. (12) and gives rise to the conditions

$$F^1_{++} \approx iF^1_{+-}$$

and

$$F^1_{+\pm} \approx F^{-1}_{+\pm}\,.$$

The first relation expresses the near maximal negative contribution to the Λ polarization of the $\mu = \pm 1$ amplitudes. This effect is illustrated in Fig. 27(c). The second condition may indicate the dominance of natural-parity exchange for these amplitudes. This is reflected in the approximate equality of ρ_{11} and $\rho_{1\,-1}$ in the t channel as indicated in Fig. 23.

3. Restriction on other measurable quantities. $A_\pm{}^2$, $D_\pm{}^2$, and $S_\pm{}^2$ have been determined from six of the measured variables as indicated in Eq. (14). The dominance of A_+ and S_- restricts the possible values of the six remaining density-matrix elements in Eq. (9) and (11). These requirements are satisfied experimentally for $|t'| < 0.8$, giving a check on the consistency of the data.

These requirements from A_+ and S_- dominance are as follows:

$$\text{(a)}\quad \mathrm{Re}\rho_{10} = \frac{1}{\sqrt{2}}\,\mathrm{Re}(A_-^* D_- + A_+^* D_+)\,, \tag{16}$$

$$\mathrm{Im}(\rho^{10}_{+-} - \rho^{10}_{-+}) = \frac{1}{\sqrt{2}}\mathrm{Re}(A_-^* D_- - A_+^* D_+)\,; \tag{17}$$

both (16) and (17) should be small but opposite in sign as shown in Figs. 23 and 24.

$$\text{(b)}\quad \mathrm{Im}\rho^{1\,-1}_{+\,+} = \tfrac{1}{2}\,\mathrm{Im}(D_- S_+^* - S_- D_+^*)\,, \tag{18}$$

$$\mathrm{Im}(\rho^{1\,-1}_{+\,-} + \rho^{1\,-1}_{-\,+}) = \mathrm{Re}(S_- D_+^* - D_- S_+^*)\,; \tag{19}$$

both (18) and (19) should be small as shown in Figs. 25 and 24.

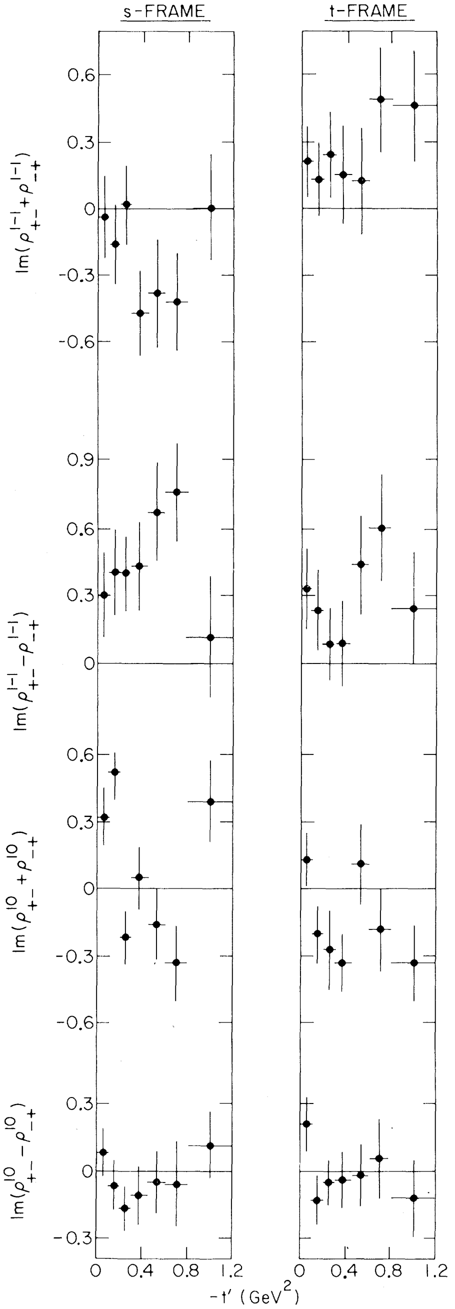

FIG. 24. Double density-matrix elements of the $K^*(890)^0$ decay and Λ polarization correlation vs t' for the reaction $\pi^-p \to \Lambda K^*(890)^0$ at 4.5 GeV/c, part one of two. See text for details.

$$\text{(c)}\quad \mathrm{Im}(\rho^{10}_{++}-\rho^{10}_{--})=\frac{1}{\sqrt{2}}\mathrm{Im}(S_-A_+^*-A_-S_+^*)\,, \qquad (20)$$

$$\mathrm{Im}(\rho^{10}_{+-}+\rho^{10}_{-+})=\frac{1}{\sqrt{2}}\,\mathrm{Re}(A_-S_+^*-S_-A_+^*)\,. \qquad (21)$$

In this case either one *or* both must be large depending on the relative phase of A_+ and S_- (see Figs. 25 and 24). From Eqs. (20) and (21) the phase of S_- with respect to A_+ is found to be in the range 0° → −120° for $|t'|<0.8$ GeV^2.

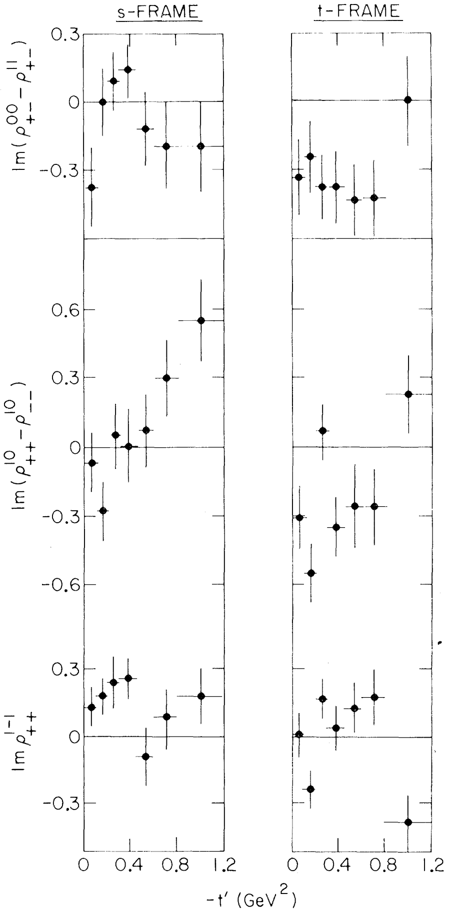

FIG. 25. Double density-matrix elements of the $K^*(890)^0$ decay and Λ polarization correlation vs t' for the reaction $\pi^-p \to \Lambda K^*(890)^0$ at 4.5 GeV/c, part two of two. See text for details.

The conclusions 1 and 2 indicate strong Λ polarization produced by both natural- and unnatural-parity exchanges, positive in sign for the unnatural-parity exchange and negative for natural-parity exchange. Consequently the simplest model with only K and exchange-degenerate $K^*(890)$ and $K^*(1420)$ exchanges cannot explain the Λ-polarization data. Additional trajectories must be introduced for both unnatural- and natural-parity exchanges (or exchange degeneracy broken). Alternatively, absorptive effects could be introduced.

With a greater amount of data all the relative phases within the two sets of amplitudes $(A_+S_-D_+)$ and $(A_-S_+D_-)$ could be determined using Eqs. (16)–(21). The relative phase between these two sets can only be determined using a longitudinally polarized target. However, the greater the domi-

TABLE X. t-channel double density-matrix elements [a] for $\pi^-p \to \Lambda K^*(890)^0$ at 4.5 GeV/c.

Range of $-t'$			t channel				
(GeV^2)	$\rho^{00}_{+-}-\rho^{11}_{+-}$	$\rho^{10}_{++}-\rho^{10}_{--}$	$\rho^{1\,-1}_{++}$	$\rho^{1\,-1}_{+-}+\rho^{1\,-1}_{-+}$	$\rho^{1\,-1}_{+-}-\rho^{1\,-1}_{-+}$	$\rho^{10}_{+-}+\rho^{10}_{-+}$	$\rho^{10}_{+-}-\rho^{10}_{-+}$
0.0−0.1	-0.34 ± 0.17	-0.31 ± 0.14	0.01 ± 0.10	0.22 ± 0.16	0.33 ± 0.19	0.13 ± 0.12	0.21 ± 0.12
0.1−0.2	-0.25 ± 0.16	-0.55 ± 0.13	-0.23 ± 0.08	0.13 ± 0.16	0.23 ± 0.18	-0.20 ± 0.14	-0.14 ± 0.11
0.2−0.3	-0.38 ± 0.14	0.07 ± 0.12	0.17 ± 0.09	0.24 ± 0.20	0.08 ± 0.16	-0.27 ± 0.18	-0.05 ± 0.10
0.3−0.45	-0.38 ± 0.16	-0.35 ± 0.13	0.04 ± 0.10	0.15 ± 0.22	0.07 ± 0.19	-0.33 ± 0.14	-0.04 ± 0.12
0.45−0.6	-0.44 ± 0.16	-0.26 ± 0.18	0.13 ± 0.11	0.12 ± 0.24	0.44 ± 0.23	0.12 ± 0.18	-0.02 ± 0.14
0.6−0.8	-0.43 ± 0.17	-0.26 ± 0.17	0.18 ± 0.12	0.49 ± 0.24	0.59 ± 0.24	-0.18 ± 0.20	0.07 ± 0.18
0.8−1.2	0.00 ± 0.20	0.23 ± 0.17	-0.37 ± 0.12	0.45 ± 0.25	0.23 ± 0.25	-0.33 ± 0.17	-0.12 ± 0.17

[a] The data shown are the imaginary part of the combinations listed.

nance of the amplitudes A_+ and S_-, the less the information that can be obtained from the polarized-target experiment.

C. $\pi^-p \to \Lambda K^*(890)^0$ at 6 GeV/c

The differential cross section is shown in Fig. 28 together with the Λ polarization. A forward flattening of the differential cross section is again observed; we will comment on this point in Sec. IV D.

Single density-matrix elements (see Fig. 29) and double density-matrix elements are presented in Tables XIII and XIV. The limited amount of data at 6 GeV/c only allows the determination of double density-matrix elements for two intervals of t'. The experimentally determined values of $A_\pm{}^2$, $D_\pm{}^2$, and $S_\pm{}^2$ are displayed in Fig. 26 and show a similar behavior to the 4.5-GeV/c data, namely, the dominance of $A_+{}^2$ and $S_-{}^2$.

D. Remarks on $K^*(890)^0$ Production from $\pi^-p \to \Lambda K^*(890)^0$ at 4.5 and 6 GeV/c

The principal difference between the data at the two momenta is the steeper slope of the differential cross section at 6 GeV/c where $b = 3.2\pm0.4$ GeV^{-2} compared to a value of $b = 2.5\pm0.2$ GeV^{-2} at 4.5 GeV/c. The forward flattening of the differential cross sections is observed at both momenta and can be associated with the dip observed in $(\rho_{11}+\rho_{1\,-1})d\sigma/dt$ as shown in Figs. 30 and 31. This is most naturally explained by the kinematic requirement of a forward dip for the natural-parity contributions from the $K^*(890)^0$ and $K^*(1420)^0$. Furthermore, one also notes for the t-channel frame

$$\rho_{00}\frac{d\sigma}{dt} \gg (\rho_{11}-\rho_{1\,-1})\frac{d\sigma}{dt},$$

$$(\rho_{11}+\rho_{1\,-1})\frac{d\sigma}{dt} \gg (\rho_{11}-\rho_{1\,-1})\frac{d\sigma}{dt},$$

$$(\rho_{11}+\rho_{1\,-1})\frac{d\sigma}{dt} \simeq 2\rho_{00}\frac{d\sigma}{dt} \text{ for } |t'|>0.1 \text{ GeV}^2$$

at both momenta. This can be taken as an indication of the relative importance of the natural-parity exchanges compared to the unnatural-parity exchanges for $|t'|>0.1$ GeV^2.

E. $\pi^-p \to \Sigma^0 K^*(890)^0$ at 4.5 GeV/c

The differential cross section and $K^*(890)^0$ single density-matrix elements are shown in Figs. 32 and 33 and in Table XV. The determination of polarization as a function of t' is not possible due to limited statistics. The mean value for the range $|t'| < 2.0$ GeV^2 is given and appears positive ($P_{\Sigma^0} = 0.45 \pm 0.3$). We note that the $(\rho_{11}+\rho_{1\,-1})d\sigma/dt$ gives the largest contribution to the cross section as shown in Fig. 34 and Table XVI.

TABLE XI. s-channel double density-matrix elements [a] for $\pi^-p \to \Lambda K^*(890)^0$ at 4.5 GeV/c.

Range of $-t'$			s channel				
(GeV^2)	$\rho^{00}_{+-}-\rho^{11}_{+-}$	$\rho^{10}_{++}-\rho^{10}_{--}$	$\rho^{1\,-1}_{++}$	$\rho^{1\,-1}_{+-}+\rho^{1\,-1}_{-+}$	$\rho^{1\,-1}_{+-}-\rho^{1\,-1}_{-+}$	$\rho^{10}_{+-}+\rho^{10}_{-+}$	$\rho^{10}_{+-}-\rho^{10}_{-+}$
0.0−0.1	-0.38 ± 0.17	-0.07 ± 0.13	0.13 ± 0.09	-0.05 ± 0.19	0.30 ± 0.19	0.32 ± 0.13	0.08 ± 0.11
0.1−0.2	0.01 ± 0.15	-0.28 ± 0.13	0.18 ± 0.08	-0.16 ± 0.18	0.39 ± 0.19	0.52 ± 0.12	-0.07 ± 0.11
0.2−0.3	0.09 ± 0.13	0.05 ± 0.14	0.24 ± 0.12	0.03 ± 0.18	0.39 ± 0.17	-0.22 ± 0.12	-0.17 ± 0.10
0.3−0.45	0.14 ± 0.13	0.00 ± 0.16	0.26 ± 0.09	-0.47 ± 0.19	0.42 ± 0.20	0.06 ± 0.14	-0.11 ± 0.13
0.45−0.6	-0.12 ± 0.16	0.07 ± 0.16	-0.09 ± 0.13	-0.37 ± 0.25	0.66 ± 0.22	-0.16 ± 0.16	-0.05 ± 0.14
0.6−0.8	-0.20 ± 0.19	0.30 ± 0.17	0.09 ± 0.15	-0.41 ± 0.22	0.75 ± 0.22	-0.32 ± 0.17	-0.06 ± 0.19
0.8−1.2	-0.20 ± 0.20	0.55 ± 0.18	0.18 ± 0.12	0.02 ± 0.24	0.10 ± 0.27	0.39 ± 0.18	0.11 ± 0.15

[a] The data shown are the imaginary part of the combinations listed.

TABLE XII. Density-matrix elements times differential cross section[a] for $\pi^-p \rightarrow \Lambda K^*(890)^0$ at 4.5 GeV/c.

Range of	t channel			s and t channels			s channel		
$-t'$ (GeV^2)	$\rho_{11}-\rho_{1\,-1}$	$(\rho_{11}-\rho_{1\,-1})\frac{d\sigma}{dt}$	$\rho_{00}\frac{d\sigma}{dt}$	$\rho_{11}+\rho_{1\,-1}$	$(\rho_{11}+\rho_{1\,-1})\frac{d\sigma}{dt}$	$(1-\rho_{11}-\rho_{1\,-1})\frac{d\sigma}{dt}$	$\rho_{11}-\rho_{1\,-1}$	$(\rho_{11}-\rho_{1\,-1})\frac{d\sigma}{dt}$	$\rho_{00}\frac{d\sigma}{dt}$
0.0–0.1	0.13 ± 0.06	10.1 ± 5.3	32.2 ± 7.4	0.48 ± 0.08	38.6 ± 7.8	42.3 ± 8.0	0.16 ± 0.07	12.5 ± 5.6	29.8 ± 7.1
0.1–0.2	0.04 ± 0.05	3.0 ± 4.7	36.6 ± 7.4	0.54 ± 0.08	47.0 ± 8.2	39.7 ± 7.6	0.20 ± 0.07	17.1 ± 6.4	22.6 ± 6.7
0.2–0.3	0.07 ± 0.07	5.8 ± 5.4	20.7 ± 6.4	0.66 ± 0.08	51.9 ± 8.4	26.5 ± 7.0	0.26 ± 0.07	20.0 ± 5.9	6.5 ± 5.1
0.3–0.45	0.12 ± 0.06	5.6 ± 3.1	12.4 ± 4.2	0.63 ± 0.09	30.2 ± 5.4	18.0 ± 4.7	0.22 ± 0.08	10.5 ± 3.9	7.5 ± 3.3
0.45–0.6	0.13 ± 0.08	4.8 ± 2.8	5.4 ± 2.8	0.72 ± 0.09	25.5 ± 4.6	10.2 ± 3.5	0.19 ± 0.08	6.7 ± 2.8	3.5 ± 2.6
0.6–0.8	0.17 ± 0.09	4.0 ± 2.1	3.5 ± 2.0	0.67 ± 0.11	15.5 ± 3.3	7.5 ± 2.7	0.17 ± 0.09	3.8 ± 2.0	3.6 ± 2.1
0.8–1.2	0.32 ± 0.10	3.6 ± 1.2	2.7 ± 1.1	0.45 ± 0.11	5.1 ± 1.4	6.4 ± 1.5	0.20 ± 0.09	2.3 ± 1.1	4.0 ± 1.3
1.2–1.6	0.5 ± 0.2	1.6 ± 0.8	0.0 ± 0.4	0.5 ± 0.2	1.7 ± 0.8	1.6 ± 0.8	0.05 ± 0.15	0.2 ± 0.5	1.4 ± 0.7

[a] Cross sections are given in μb/GeV^2.

F. Comparison of $\pi^-p \rightarrow \Sigma^0 K^*(890)^0$ and $\pi^-p \rightarrow \Lambda K^*(890)^0$

If we identify $(\rho_{11}+\rho_{1\,-1})d\sigma/dt$ as the natural-parity exchange and $(1-\rho_{11}-\rho_{1\,-1})d\sigma/dt$ as the unnatural-parity exchange, the natural-parity exchange is seen to be more important than the unnatural-parity exchange beyond the small t' values. This is particularly pronounced in the $\pi^-p \rightarrow \Sigma^0K^*(890)^0$ reaction. Comparison of Figs. 23 and 33 shows that the t-channel density-matrix element ρ_{00} takes smaller values for $\pi^-p \rightarrow \Sigma^0K^*(890)^0$ than for $\pi^-p \rightarrow \Lambda K^*(890)^0$. This feature, interpreted as the greater dominance of natural-parity exchanges in $\pi^-p \rightarrow \Sigma^0K^*(890)^0$ compared to $\pi^-p \rightarrow \Lambda K^*(890)^0$, is indeed expected on the basis of the known smallness of the ratio $g_{K\Sigma\bar{N}}/g_{K\Lambda\bar{N}}$,[17] assuming K exchange to be the main unnatural-parity-exchange contribution.

The natural-parity-exchange contribution to the Λ polarization in $\pi^-p \rightarrow \Lambda K^*(890)^0$ has been shown to be negative and is illustrated in Fig. 46(a) below. The opposite sign is observed for Σ^0 polarization in $\pi^-p \rightarrow \Sigma^0K^*(890)$, a reaction dominated by natural-parity exchanges.

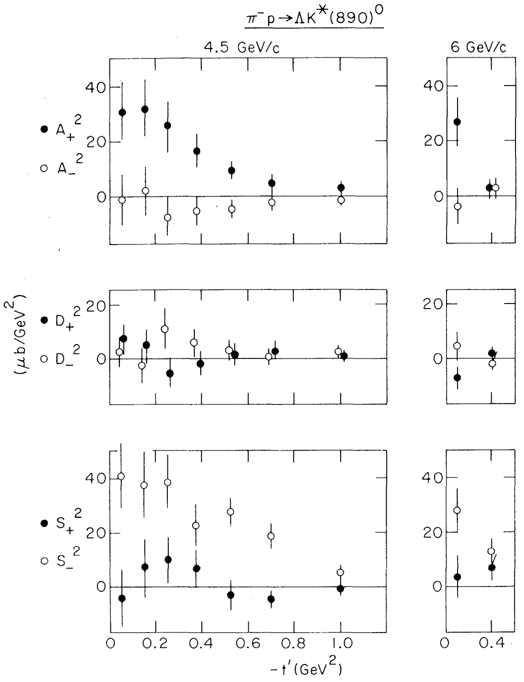

FIG. 26. Relevant combinations of the helicity amplitudes in the t frame for reaction (2a). See text for details.

G. Isospin Conservation in $\pi^-p \rightarrow \Lambda K^*(890)^0$

Assuming isospin conservation, the $K^*(890)^0$ decay branching ratio is

$$R\left(\frac{K^* \rightarrow K^+\pi^-}{K^* \rightarrow K^0\pi^0}\right) = 5.82$$

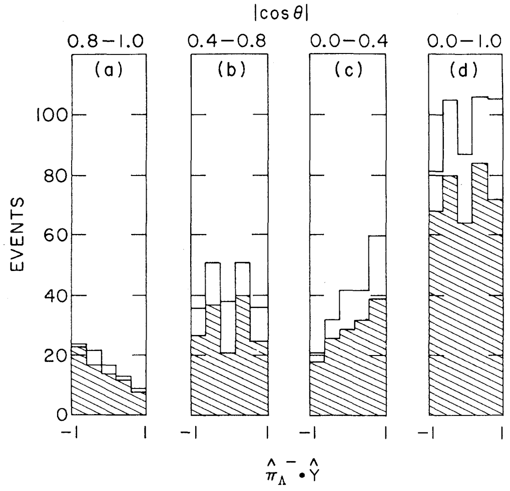

FIG. 27. Λ decay distribution, $\hat{\pi}_\Lambda^- \cdot \hat{Y}$, for various regions of cosθ. $\hat{\pi}_\Lambda^-$ is the direction of the π^- in the Λ decay calculated in the Λ rest frame. $\hat{Y}$ is the direction of the production normal. cosθ is the Gottfried-Jackson angle of the $K^*(890)^0$ from the reaction $\pi^-p \rightarrow \Lambda K^*(890)^0$ at 4.5 GeV/c. Shaded region is for $|t'| < 0.45$ GeV^2 while unshaded region is for $|t'| < 0.8$ GeV^2.

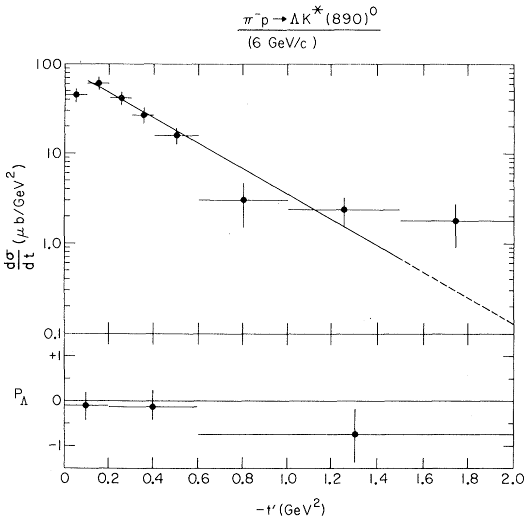

FIG. 28. Differential cross section and Λ polarization for reaction (2a) at 6 GeV/c. Solid line, indicating the fit shown in Table I, is extended by the dashed line for reference.

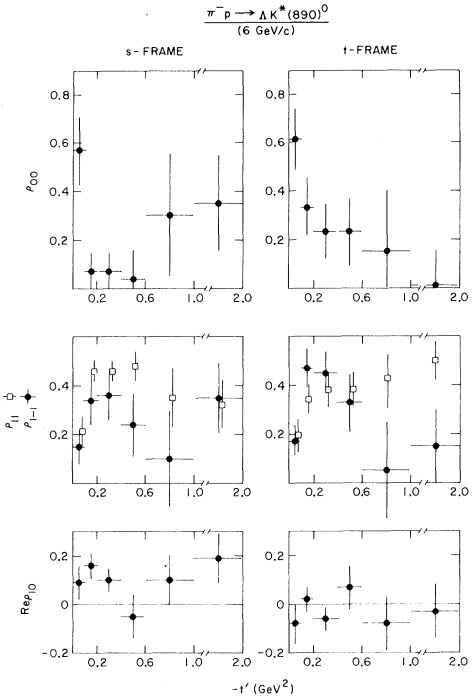

FIG. 29. Density-matrix elements vs t' for reaction (2a) at 6.0 GeV/c.

when a visible K^0 is required. Lynch *et al.*[18] claimed to observe a 3-standard-deviation deficit in the number of $K^*(890)^0 \to K^0\pi^0$, $K^*(890)^+ \to K^+\pi^0$ compared to the number expected from the observed $K^*(890)^0 \to K^+\pi^-$ and $K^*(890)^+ \to K^0\pi^+$ in the reactions $\pi^- p \to \Lambda K^*(890)^0$ and $\pi^+ n \to \Lambda K^*(890)^+$ at 7 GeV/c. They suggested the possibility of isospin nonconservation in the production process for these reactions.

We have examined this ratio in the reaction $\pi^- p \to \Lambda K^*(890)^0$ at both 4.5 and 6.0 GeV/c. The critical question is the separation of the $\pi^- p \to \Lambda K^0\pi^0$ events from the $\Sigma^0 K^0\pi^0$ final state. The effect of

TABLE XIII. Differential cross section, density-matrix elements and density-matrix elements times differential cross sections[a] for $\pi^- p \to \Lambda K^*(890)^0$ at 6.0 GeV/c.

Range of $-t'$ (GeV^2)	$d\sigma/dt$ (μb/GeV^2)	t channel ρ_{00}	t channel ρ_{1-1}	t channel Reρ_{10}	s channel ρ_{00}	s channel ρ_{1-1}	s channel Reρ_{10}
0.0–0.1	45 ± 8	0.61 ± 0.13	0.17 ± 0.06	−0.08 ± 0.08	0.57 ± 0.14	0.15 ± 0.07	0.09 ± 0.07
0.1–0.2	61 ± 10	0.33 ± 0.12	0.47 ± 0.08	0.02 ± 0.05	0.07 ± 0.08	0.34 ± 0.10	0.16 ± 0.05
0.2–0.3	42 ± 8	0.23 ± 0.11	0.45 ± 0.08	−0.06 ± 0.05	0.07 ± 0.08	0.36 ± 0.10	0.10 ± 0.05
0.3–0.4	27 ± 6						
0.4–0.6	16 ± 3.4	0.23 ± 0.14	0.33 ± 0.12	0.07 ± 0.09	0.04 ± 0.12	0.24 ± 0.13	−0.05 ± 0.09
0.6–1.0	3.0 ± 1.5	0.15 ± 0.25	0.05 ± 0.21	−0.08 ± 0.11	0.30 ± 0.25	0.10 ± 0.20	0.10 ± 0.10
1.0–1.5	2.4 ± 0.9	0.0 ± 0.15	0.15 ± 0.15	−0.03 ± 0.11	0.35 ± 0.2	0.35 ± 0.15	0.19 ± 0.10
1.5–2.0	1.8 ± 0.9						

Range of $\|t'\|$ (GeV^2)	$d\sigma/dt'$ (μb/GeV^2)	t channel $\rho_{00}\frac{d\sigma}{dt}$	t channel $(\rho_{11}-\rho_{1-1})\frac{d\sigma}{dt}$	s channel $\rho_{00}\frac{d\sigma}{dt}$	s channel $(\rho_{11}-\rho_{1-1})\frac{d\sigma}{dt}$	$(\rho_{11}+\rho_{1-1})\frac{d\sigma}{dt}$	$(1-\rho_{11}-\rho_{1-1})\frac{d\sigma}{dt}$
0.0–0.1	45 ± 8	27 ± 7	1 ± 3	28 ± 8	3 ± 5	16 ± 5	29 ± 7
0.1–0.2	61 ± 10	20 ± 8	0 ± 4	4 ± 5	8 ± 6	49 ± 10	12 ± 7
0.2–0.3	42 ± 8	8 ± 4	0 ± 2	2 ± 3	4 ± 4	28 ± 6	6 ± 4
0.3–0.4	27 ± 6						
0.4–0.6	16 ± 3.4	3.5 ± 2	1 ± 2	1 ± 2	4 ± 2	11 ± 3.5	4.5 ± 2.5
0.6–1.0	3.0 ± 1.5	0.5 ± 0.8	1.1 ± 0.8	0.9 ± 0.9	0.7 ± 0.9	1.4 ± 0.9	1.6 ± 0.9
1.0–1.5	2.4 ± 0.9	0 ± 0.3				1.4 ± 0.5	
1.5–2.0	1.8 ± 0.9						

[a] Cross sections are given in μb/GeV^2.

TABLE XIV. Differential cross section, Λ polarization, single density-matrix elements, double density-matrix elements,[a] and density-matrix elements times differential cross section[b] for $\pi^- p \to \Lambda K^*(890)^0$ at 6.0 GeV/c.

Range of $-t'$ (GeV^2)	$d\sigma/dt$ (μb/GeV^2)	P_Λ	t channel ρ_{00}	t channel ρ_{1-1}	t channel Reρ_{10}	s channel ρ_{00}	s channel ρ_{1-1}	s channel Reρ_{10}
0.0–0.2	53 ± 7	−0.11 ± 0.33	0.45 ± 0.09	0.34 ± 0.05	−0.03 ± 0.05	0.28 ± 0.08	0.36 ± 0.10	0.10 ± 0.05
0.2–0.6	25 ± 3	−0.11 ± 0.32	0.23 ± 0.09	0.41 ± 0.07	−0.02 ± 0.05	0.06 ± 0.07	0.32 ± 0.08	0.06 ± 0.04
0.6–2.0	2.4 ± 0.6	−0.73 ± 0.55						

t channel[a]

Range of $-t'$ (GeV^2)	$\rho^{00}_{+-} - \rho^{11}_{+-}$	$\rho^{10}_{++} - \rho^{10}_{--}$	ρ^{1-1}_{++}	$\rho^{1-1}_{+-} + \rho^{1-1}_{-+}$	$\rho^{1-1}_{+-} + \rho^{1-1}_{-+}$	$\rho^{10}_{+-} + \rho^{10}_{-+}$	$\rho^{10}_{+-} - \rho^{10}_{-+}$
0.0–0.2	−0.48 ± 0.18	−0.45 ± 0.14	−0.09 ± 0.10	0.37 ± 0.22	0.13 ± 0.19	−0.05 ± 0.20	0.10 ± 0.12
0.2–0.6	−0.03 ± 0.17	−0.11 ± 0.15	0.00 ± 0.09	0.09 ± 0.26	0.19 ± 0.21	−0.55 ± 0.16	0.11 ± 0.11

s channel[a]

Range of $-t'$ (GeV^2)	$\rho^{00}_{+-} - \rho^{11}_{+-}$	$\rho^{10}_{++} - \rho^{10}_{--}$	ρ^{1-1}_{++}	$\rho^{1-1}_{+-} + \rho^{1-1}_{-+}$	$\rho^{1-1}_{+-} - \rho^{1-1}_{-+}$	$\rho^{10}_{+-} + \rho^{10}_{-+}$	$\rho^{10}_{+-} - \rho^{10}_{-+}$
0.0–0.2	−0.33 ± 0.18	−0.10 ± 0.18	0.16 ± 0.11	−0.05 ± 0.21	0.23 ± 0.19	0.36 ± 0.17	−0.10 ± 0.13
0.2–0.6	−0.19 ± 0.14	−0.11 ± 0.18	0.42 ± 0.12	−0.13 ± 0.19	0.08 ± 0.25	0.10 ± 0.14	−0.04 ± 0.10

Range of $-t'$ (GeV^2)	t channel $\rho_{11} - \rho_{1-1}$	t channel $(\rho_{11} - \rho_{1-1})\frac{d\sigma}{dt}$	t channel $\rho_{00}\frac{d\sigma}{dt}$	s and t channels $\rho_{11} + \rho_{1-1}$	s and t channels $(\rho_{11} + \rho_{1-1})\frac{d\sigma}{dt}$	s and t channels $(1 - \rho_{11} - \rho_{1-1})\frac{d\sigma}{dt}$	s channel $\rho_{11} - \rho_{1-1}$	s channel $(\rho_{11} - \rho_{1-1})\frac{d\sigma}{dt}$	s channel $\rho_{00}\frac{d\sigma}{dt}$
0.0–0.2	−0.07 ± 0.05	−3 ± 3	24 ± 5	0.62 ± 0.08	33 ± 6	20 ± 5	0.10 ± 0.07	5 ± 4	15 ± 5
0.2–0.6	−0.02 ± 0.06	−1 ± 2	6 ± 2	0.79 ± 0.09	20 ± 4	5 ± 2	0.15 ± 0.08	4 ± 2	1 ± 2

[a] The data shown are the imaginary part of the combinations listed.

[b] Cross sections are given in μb/GeV^2.

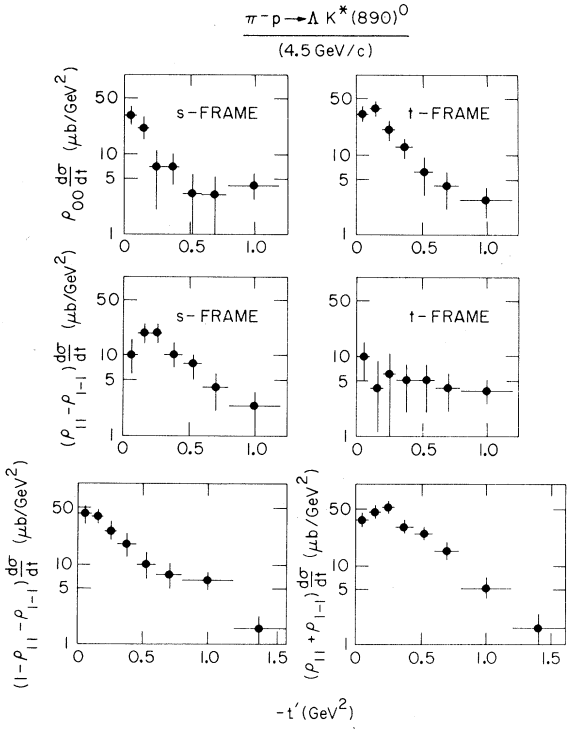

FIG. 30. Single density-matrix elements multiplied by the differential cross section vs t' for reaction (2a) at 4.5 GeV/c.

$\Sigma^0K^0\pi^0$ contamination of $\Lambda K^0\pi^0$ is simulated by examining the missing mass recoiling against the Λ in the analogous $\Sigma^0K^+\pi^-$ reaction. The $\Sigma^0K^+\pi^-$ sample shows a strong $K^*(890)^0$ signal. However, the missing mass $(K^+\pi^-\gamma)$ recoiling against the Λ, from the $\Sigma^0K^+\pi^-$ final state [Fig. 17(b)] shows only a broad distribution at masses well above the $K^*(890)^0$. We therefore conclude that any $\Sigma^0K^0\pi^0$ contamination in the $\Lambda K^0\pi^0$ sample does not affect the $\Lambda K^*(890)^0$ intensity. The Dalitz plot for the final sample of $\Lambda K^0\pi^0$ events at 4.5 GeV/c is shown in Fig. 35. A clear $K^*(890)^0$ and $\Sigma(1385)^0$ signal is seen.

The resulting mass spectra for $K^+\pi^-$ and $K^0\pi^0$ are displayed in Fig. 36. Results of the fits are shown in Table XVII. The values of R for the $K^*(890)^0$ are 5.8 ± 0.8 at 4.5 GeV/c and 5.4 ± 1.2 at 6 GeV/c; both are in good agreement with the expected value of 5.82. We therefore conclude that we do not observe any peculiarities in the $K^*(890)^0$ decay.

V. $\pi^-p\to\Lambda K^*(1420)^0$

A. $K^*(1420)^0\to K\pi$

From Figs. 12–15, the $K^*(1420)^0\to K^+\pi^-$ production is evident both at 4.5 and 6 GeV/c. The mass and width parameters are

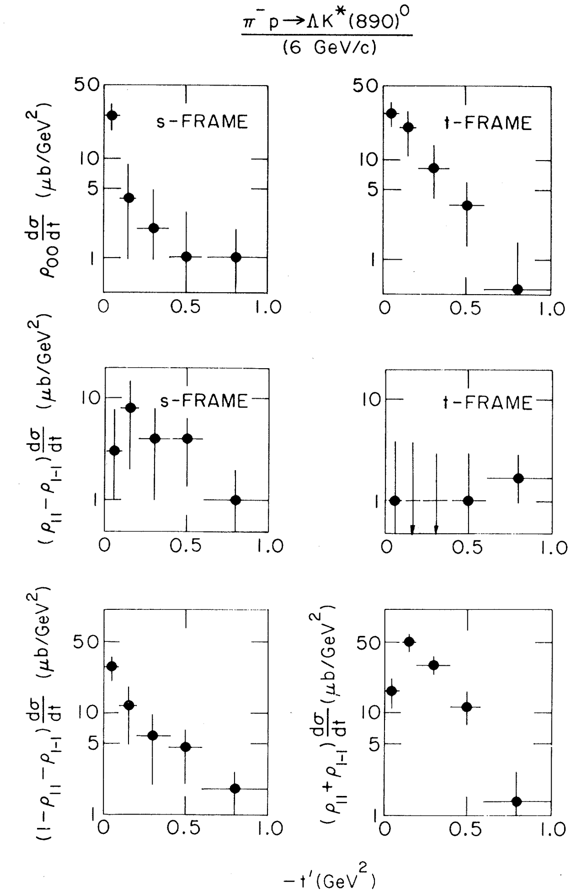

FIG. 31. Density-matrix elements times the differential cross section vs t' for reaction (2a) at 6.0 GeV/c.

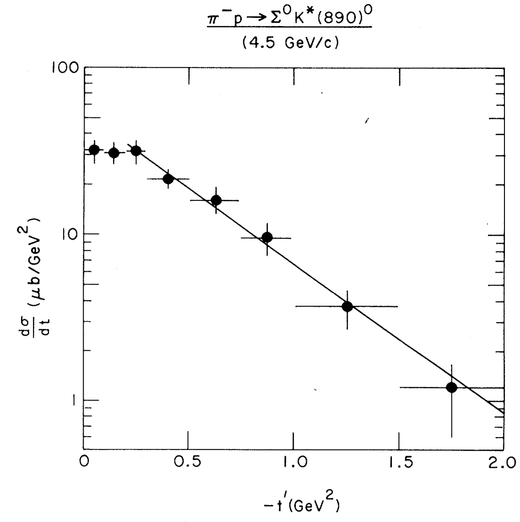

FIG. 32. Differential cross section for reaction (2b) at 4.5 GeV/c. Solid line indicates the fit shown in Table I.

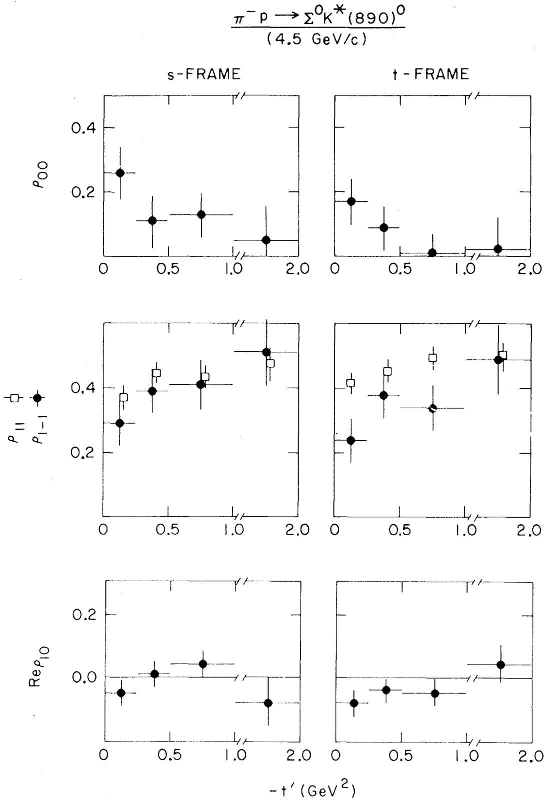

FIG. 33. Density-matrix elements vs t' for reaction (2b) at 4.5 GeV/c.

$M(K^+\pi^-)$ (MeV)	Γ (MeV)	P_{lab} (GeV/c)
1425 ± 10	130 ± 30	4.5
1430 ± 12	83^{+35}_{-24}	6.0

The values of mass and width at the two momenta are in agreement with accepted values. Because of the limited statistics at 6 GeV/c only the

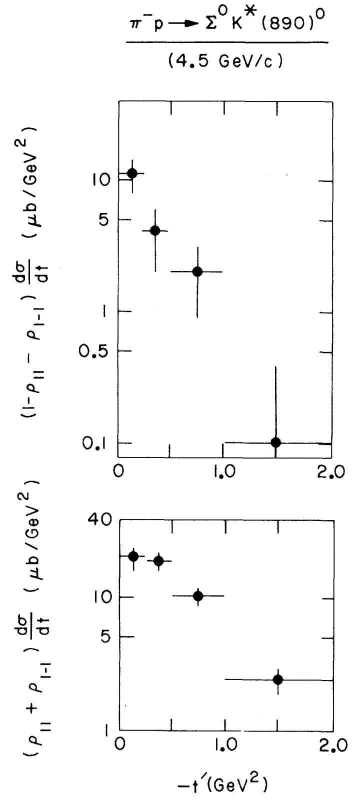

FIG. 34. Density-matrix element combinations times the differential cross section for reaction (2b) at 4.5 GeV/c.

$K^*(1420)^0\to K\pi$ cross section is given in Table I. For the 4.5-GeV/c data, the c.m. angular distribution for the $K^*(1420)^0$ is shown in Fig. 37 and Table XVIII. The forward differential cross section and Λ polarization are presented in Fig. 38 and Table XIX. The results of a fit to the differen-

TABLE XV. Differential cross section, Σ^0 polarization, and single density-matrix elements for $\pi^-p\to\Sigma^0K^*(890)^0$ at 4.5 GeV/c.

Range of $-t'$ (GeV^2)	$d\sigma/dt$ (μb/GeV^2)	$P_{\Sigma 0}$	t channel ρ_{00}	ρ_{1-1}	$\text{Re}\rho_{10}$	s channel ρ_{00}	ρ_{1-1}	$\text{Re}\rho_{10}$
0.0–0.25	31 ± 3.5	0.45 ± 0.3	0.17 ± 0.07	0.24 ± 0.07	-0.07 ± 0.04	0.26 ± 0.08	0.29 ± 0.07	-0.04 ± 0.04
0.25–0.5	23 ± 3		0.09 ± 0.07	0.38 ± 0.07	-0.03 ± 0.04	0.11 ± 0.07	0.39 ± 0.07	0.02 ± 0.04
0.5–1.0	12.5 ± 1.5		0.01 ± 0.08	0.34 ± 0.07	-0.04 ± 0.04	0.13 ± 0.07	0.41 ± 0.08	0.05 ± 0.04
1.0–2.0	2.5 ± 0.5		0.02 ± 0.10	0.49 ± 0.11	0.05 ± 0.05	0.05 ± 0.11	0.51 ± 0.10	-0.07 ± 0.06

Range of $-t'$ (GeV^2)	$d\sigma/dt$ (μb/GeV^2)	Range of $-t'$ (GeV^2)	$d\sigma/dt$ (μb/GeV^2)
0.0–0.1	32 ± 5	0.5–0.75	16 ± 3
0.1–0.2	31 ± 5	0.75–1.0	9.5 ± 2
0.2–0.3	31 ± 5	1.0–1.5	3.7 ± 1
0.3–0.5	21.5 ± 3	1.5–2.0	1.2 ± 0.6

TABLE XVI. Density-matrix elements times differential cross section[a] for $\pi^-p \to \Sigma^0 K^*(890)^0$ at 4.5 GeV/*c*.

Range of $-t'$ (GeV^2)	*t* channel $\rho_{11}-\rho_{1-1}$	$(\rho_{11}-\rho_{1-1})\frac{d\sigma}{dt}$	$\rho_{00}\frac{d\sigma}{dt}$	*s* and *t* channel $\rho_{11}+\rho_{1-1}$	$(\rho_{11}+\rho_{1-1})\frac{d\sigma}{dt}$	$(1-\rho_{11}-\rho_{1-1})\frac{d\sigma}{dt}$	*s* channel $\rho_{11}-\rho_{1-1}$	$(\rho_{11}-\rho_{1-1})\frac{d\sigma}{dt}$	$\rho_{00}\frac{d\sigma}{dt}$
0.0–0.25	0.18 ± 0.08	6 ± 2.5	5 ± 2.5	0.65 ± 0.09	20 ± 3.5	11 ± 3.0	0.08 ± 0.07	3 ± 2.0	8 ± 2.5
0.25–0.5	0.08 ± 0.07	2 ± 1.5	2 ± 1.5	0.83 ± 0.08	19 ± 3	4 ± 2	0.06 ± 0.07	1.5 ± 2.0	2.5 ± 2.0
0.5–1.0	0.15 ± 0.07	1.9 ± 1.0	0.1 ± 1.0	0.84 ± 0.09	10.5 ± 1.7	2.0 ± 1.1	0.03 ± 0.07	0.4 ± 1.0	1.6 ± 0.9
1.0–2.0	0.00 ± 0.11	0.0 ± 0.3	0.1 ± 0.3	0.98 ± 0.12	2.5 ± 0.5	0.1 ± 0.3	−0.04 ± 0.10	−0.1 ± 0.2	0.2 ± 0.3

[a] Cross sections in μb/ GeV^2.

tial cross section are given in Table I. The differential cross section for the $K^*(1420)^0$, like the $K^*(890)^0$, is much less steep ($b \simeq 2$ GeV^{-2}) in comparison with K^0 production ($b \simeq 8$ GeV^{-2}). The Λ polarization of the $\Lambda K^*(1420)^0$ reaction has been determined using a background subtraction obtained by comparing the mass dependence of N, the number of events, with $N\langle\cos\theta\rangle$ where $\cos\theta$ is defined in Ref. 2.

B. Density-Matrix Elements of $K^*(1420) \to K^+\pi^-$ at 4.5 GeV/*c*

The significant moments, $N\langle D^l_{\mathrm{mo}}\rangle$, of the usual D function as defined in Rose,[19] for the mass region 1.1–1.7 GeV, are shown in Fig. 39. Breit-Wigner peaks are seen in $N\langle D^2_{00}\rangle$ and $N\langle D^2_{10}\rangle$ in addition to the mass spectrum. A simultaneous mass fit to these moments and mass spectrum gives $M = 1417 \pm 9$ and $\Gamma = 113 \pm 13$ MeV. An incoherent background subtraction for the moments leads to nonphysical values of the density matrix with $\rho_{22} \sim -0.37$. This effect is well known in both $K^*(1420)^0$ and $f(1270)^0$ resonance production. The simplest explanation is the assumption of interference between s and d waves of the $K^+\pi^-$ system. The fact that the $\langle D^2_{\mathrm{mo}}\rangle$ moments retain the Breit-Wigner shape requires the s and d waves to have the same phase at the resonance mass. If we choose not to assume any rapid variation of s-wave phase in the $K^*(1420)^0$ region, this implies the s-wave phase is largely imaginary. We have used the method of Chung[20] to take into account the effects of s-d interference and also include p-wave background. Positivity constraints on the $K^*(1420)^0$ density matrix, together with limits on the maximum allowed amount of s wave, require a maximum constructive s-d wave interference for $|t'| < 0.5$ GeV^2 and destructive s-d wave interference for $2.0 > |t'| > 0.5$ GeV^2. An s-wave resonant behavior has not been invoked since it does not appear to be required; however it cannot be ruled out either. It is inter-

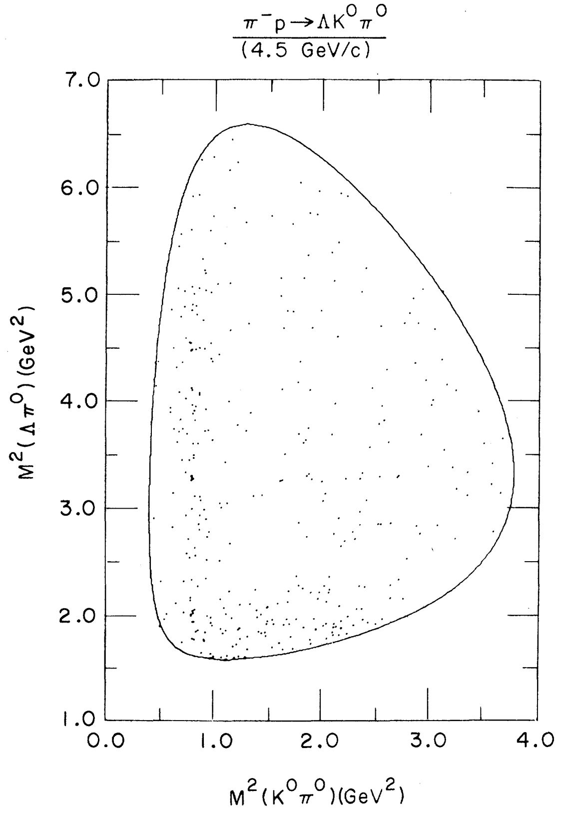

FIG. 35. Dalitz plot for the final state $\Lambda K^0\pi^0$ at 4.5 GeV/*c*.

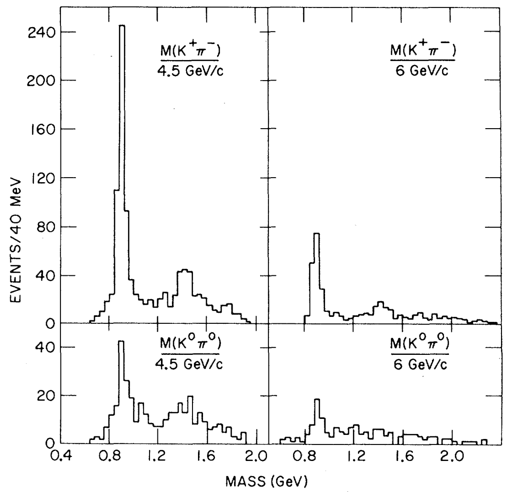

FIG. 36. $(K\pi)^0$ mass projections from the reactions $\pi^-p \to \Lambda K^+\pi^-$ and $\pi^-p \to \Lambda K^0\pi^0$ at 4.5 and 6 GeV/*c*.

TABLE XVII. Mass fits to $K^*(890)^0 \to K^+\pi^-$ and $K^*(890)^0 \to K_S^0\pi^0(K_S^0 \to \pi^+\pi^-)$.

	Breit-Wigner form	Mass (MeV)	Width (MeV)	Number of events	R (experimental) [a] $= \frac{K^+\pi^-}{K_S^0\pi^0\,(K_S^0 \to \pi^+\pi^-)}$	R (expected)
$K^+\pi^-$	$l=0$	896 ± 2	48 ± 3	526 ± 25	5.8 ± 0.8	5.82
4.5 GeV/c	$l=1$	896 ± 2	49 ± 4	535 ± 25		
$K_S^0\pi^0\,(K_S^0 \to \pi^+\pi^-)$	$l=0$	899 ± 5	60 ± 15	89 ± 11		
4.5 GeV/c	$l=1$	900 ± 5	66 ± 16	95 ± 12		
$K^+\pi^-$	$l=0$	891 ± 4	42 ± 5	167 ± 15	5.4 ± 1.2	5.82
6 GeV/c	$l=1$	891 ± 4	45 ± 5	176 ± 15		
$K_S^0\pi^0\,(K_S^0 \to \pi^+\pi^-)$	$l=0$	899 ± 7	44 ± 17	31 ± 7		
6 GeV/c	$l=1$	899 ± 7	46 ± 18	32 ± 7		

[a] Corrected for processing and escape losses.

esting to note that the s-wave phase relative to the d wave changes sign as a function of t'. The final results of the fit are given in Table XX for two t' intervals. The value for ρ_{00} for $|t'|<0.5$ GeV^2 seems to be larger for the $K^*(1420)^0$ than for the $K^*(890)^0$. The $N\langle D_{00}^1\rangle$ at the $K^*(1420)^0$ may be due to p-d interference assuming that the p-wave phase shift was slowly varying since the shape is that of the real part of the $K^*(1420)^0$ Breit-Wigner shape.

C. $K^*(1420) \to K\pi\pi$ and $K^*(1300) \to K\pi\pi$

To investigate the other decay modes of the $K^*(1420)$, we examine the final states of $\Lambda K^+\pi^-\pi^0$ and $\Lambda K^0\pi^+\pi^-$. There is strong $\Sigma(1385)^+$ and $\Sigma(1385)^0$ production in these final states; therefore events in the $\Sigma(1385)$ mass region have been removed. Figure 40 shows the $K^+\pi^-\pi^0$ and $K^0\pi^+\pi^-$ mass spectrum from the 4.5-GeV/c data for $\hat{p}\cdot\hat{\Lambda} > 0.5$. There are clear $K\pi\pi$ enhancements centered about 1.42 GeV as well as a $(K^+\pi^-\pi^0)$ enhancement at 1.3 GeV. We will discuss the $K^*(1300)^0$ later. For a comparison with the $K^+\pi^-$ decay mode of the $K^*(1420)^0$, we show the $K^+\pi^-$ mass spectrum with a similar cut of $\hat{p}\cdot\hat{\Lambda}>0.5$. An apparent difference is evident between the width of the $K^+\pi^-$ mode and the $K\pi\pi$ mode. The narrower width of the $K\pi\pi$ mode (45^{+40}_{-20} MeV for $K^+\pi^-\pi^0$ mode and 90^{+60}_{-30} MeV for the $K^0\pi^+\pi^-$ mode) in comparison with the $K^+\pi^-$ mode (130 ± 30 MeV) is not attributable to the removal of the $\Sigma(1385)$ events. This obvious difference warrants further experimental study. For the purpose of the discussion here, we assume the $K\pi\pi$ enhancement is an alternative decay mode of the $K^*(1420)^0$; however, we cannot obtain a meaningful branching ratio

$$[K^*(1420)^0 \to K\pi]\,/\,[K^*(1420)^0 \to K\pi\pi]$$

because of apparent differences in the width between $K\pi\pi$ and $K\pi$ modes and the uncertainties in the background assumptions in the $K\pi\pi$ final state.

TABLE XVIII. Differential cross section for $\pi^-p \to \Lambda K^*(1420)^0$ [$K^*(1420)^0 \to K\pi$ only] at 4.5 GeV/c.

Range of $\cos\theta^*$	$\frac{d\sigma}{d\Omega}$ (μb/sr)
0.95–1.0	13 ± 2.4
0.9–0.95	4.6 ± 1.9
0.8–0.9	2.7 ± 1.2
0.7–0.8	2.4 ± 0.9
0.5–0.7	2.6 ± 0.5
0.5– −0.8	0.19 ± 0.11
−0.8– −1.0	1.29 ± 0.44

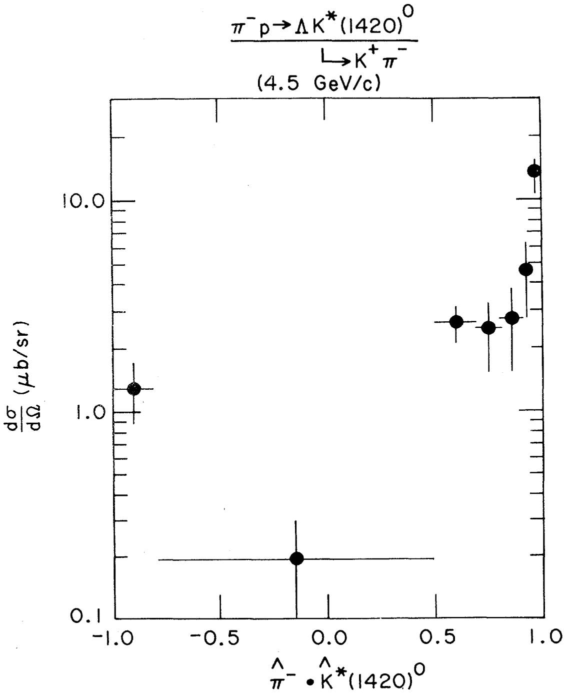

FIG. 37. Differential cross section vs center-of-mass production angle for reaction (3a) at 4.5 GeV/c.

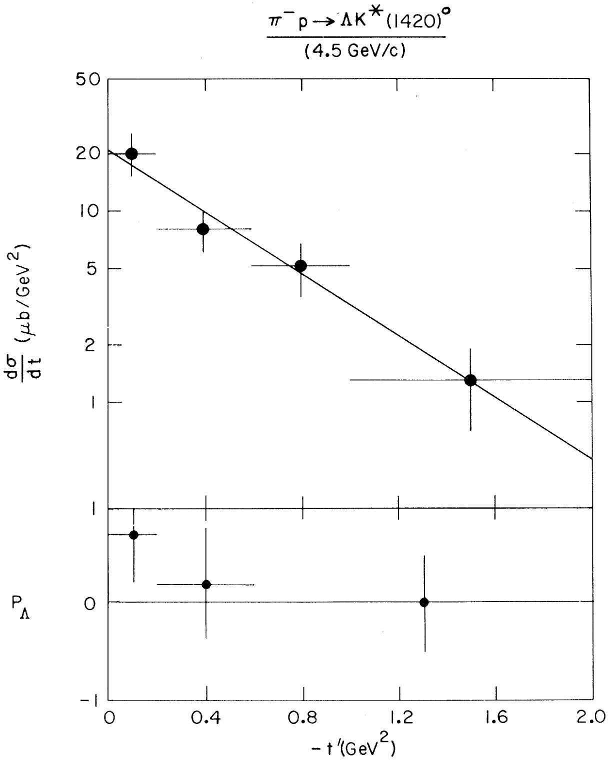

FIG. 38. Differential cross section and Λ polarization vs t' for reaction (3a) at 4.5 GeV/c.

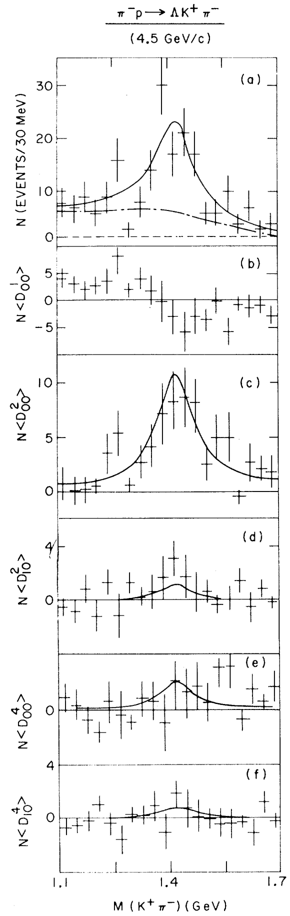

FIG. 39. Mass spectra and significant moments for the $\Lambda K^+\pi^-$ final state at 4.5 GeV/c for $|t'|<0.5$ GeV/c. Results of fit described in text are shown by solid curves. The s-wave background is shown in (a) by the dot-dashed line; the p-wave background is shown by the dashed line.

The 6-GeV/c data[21] are presented in Fig. 41. Two enhancements are again seen in the $K\pi\pi$ mass spectrum at 1300 and 1420 MeV for the combined final states ($K^0\pi^+\pi^-$ and $K^+\pi^-\pi^0$). Also the $K^+\pi^-$ spectrum is shown where only the 1420-MeV peak is evident. Within the statistics, the widths for $K^+\pi^-$ and $K\pi\pi$ are consistent with each other.

To examine the quasi-two-body decay mode of the $K\pi\pi$ enhancement at 1420 and 1300 MeV, we show in Figs. 42–44 scatter plots of the $\pi\pi$ and $K\pi$ mass spectrum versus the $K\pi\pi$ mass spectrum. The ρ, $K^*(890)$ bands are indicated by the horizontal lines. For the 4.5-GeV/c data, there is an accumulation of events where the ρ^- band intersects the $K^*(1300)^0$ and where the $K^*(890)^+$ and $K^*(890)^0$ bands intersect the $K^*(1420)^0$ in the $K^+\pi^-\pi^0$ final state (Fig. 42). For the $K^0\pi^+\pi^-$ final state, Fig. 43, the presence of the ρ^0 at the $K^*(1300)^0$ is not apparent. This may be explained assuming the $K^*(1300)^0$ has isospin $\frac{1}{2}$, in which case

$$\frac{K^*(1300)^0 \to K^+\rho^-}{K^*(1300)^0 \to K^0\rho^0} = 2\,.$$

There is also an accumulation of $K^*(890)^+$ events at the $K^*(1420)^0$ as shown in Fig. 43. Similar features are also observed in the 6-GeV/c data (Fig. 44) where the combined $K\pi\pi$ data are presented.

TABLE XIX. Differential cross sections for $\pi^-p \to \Lambda K^*(1420)^0$ [$K^*(1420)^0 \to K\pi$ only] at 4.5 GeV/c.

$-t'$ (GeV^2)	$K^*(1420)^0 \to$ $K^+\pi^-$ events	$\frac{d\sigma}{dt}$ (μb/GeV^2)	P_Λ
0–0.2	46 ± 12	20 ± 5	0.7 ± 0.5
0.2–0.6	37 ± 10	8 ± 2	0.2 ± 0.6
0.6–1.0	24 ± 7	5.1 ± 1.5	0.0 ± 0.5
1.0–2.0	15 ± 7	1.3 ± 0.6	

TABLE XX. Density-matrix elements[a] for $\pi^-p \to \Lambda K^*(1420)^0$ [$K^*(1420)^0 \to K^+\pi^-$] at 4.5 GeV/c.

$-t'$ (GeV^2)	ρ_{00}	ρ_{11}	ρ_{22}
0–0.5	0.63 ± 0.09	0.19 ± 0.05	0.00 ± 0.11
0.5–2.0	0.07 ± 0.23	0.41 ± 0.11	0.06 ± 0.20

[a] Density-matrix elements not listed are consistent with zero.

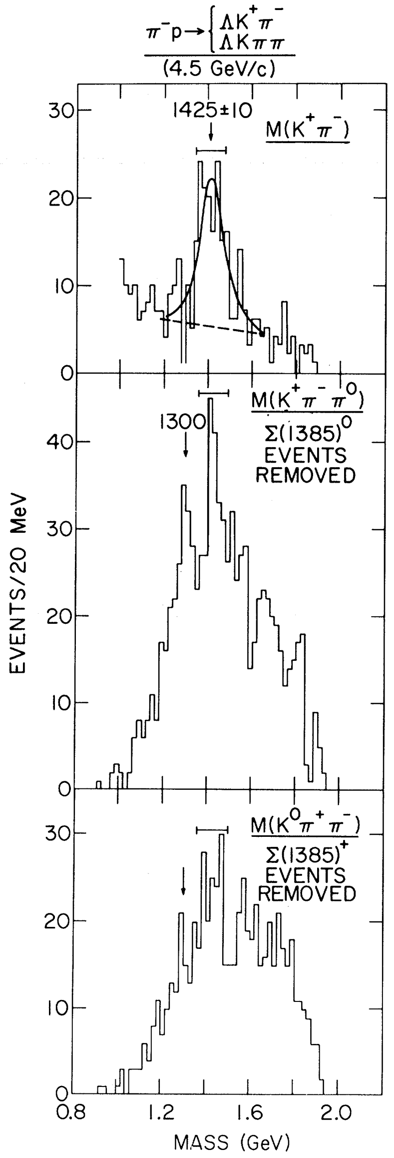

FIG. 40. $(K\pi)$ and $(K\pi\pi)$ mass spectra for center-of-mass production angle $\cos\theta^* = \hat{p} \cdot \hat{\Lambda} \geq 0.5$ at 4.5 GeV/c. Curve on $M(K^+\pi^-)$ represents fit described in text; dashed line shows linear background. For the $\Lambda K^+\pi^-\pi^0$ final state, $\Sigma(1385)^0$ is defined by $1.35 < M(\Lambda\pi^0) < 1.42$ GeV. For the $\Lambda K^0\pi^+\pi^-$ final state, $\Sigma(1385)^+$ is defined by $1.33 < M(\Lambda\pi^+) < 1.42$ GeV.

The dominance of the ρ band in the $K^*(1300)^0$ region is evident, and the strong $K^*(890)^+\pi^-$ contribution to the $K^*(1420)^0$ region in comparison with that from the $K^*(890)^0\pi^0$ is expected since the $[K^*(890)^+\pi^-]/[K^*(890)^0\pi^0] = 3$ for an isospin-$\frac{1}{2}$ assignment for the $K^*(1420)^0$ from the combined *seen* $K\pi\pi$ final states.

To study the decay modes of the $K^*(1300)^0$ and the $K^*(1420)^0$ further in the 4.5-GeV/c data, we present the two-body mass-squared projections in

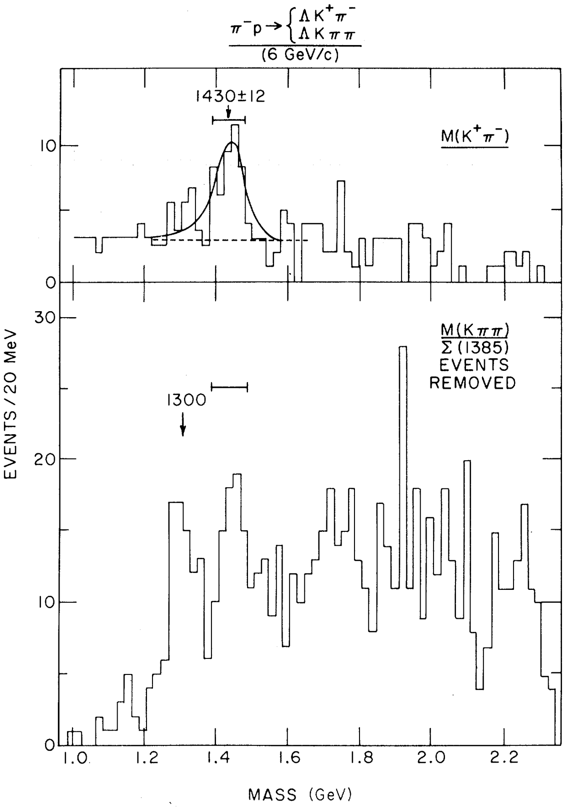

FIG. 41. $(K\pi)$ and $(K\pi\pi)$ mass spectra at 6.0 GeV/c. $\Sigma(1385)$ is defined by $1.34 < M(\Lambda\pi) < 1.43$ GeV/c.

Fig. 45 for the $K^+\pi^-\pi^0$ final state. There is a strong ρ^- signal in the $(\pi\pi)^-$ mass projections at the $K^*(1300)^0$ mass region [Fig. 45(b)], and $K^*(890)^+$ and $K^*(890)^0$ signals in the $K\pi$ mass projections at the $K^*(1420)^0$ mass region [Fig. 45(c)]. To estimate the excess amount of ρ^- and K^* signal in the $K^*(1300)^0$ and $K^*(1420)^0$ mass regions, a fit to the Dalitz plots was made corresponding to the four $K\pi\pi$ mass regions shown in Fig. 45. Assuming Figs. 45(a) and 45(d) represent the control region, an excess of 51 ± 15 ρ^- events was found in the $K^*(1300)^0$ region and an excess of 36 ± 10 $K^*(890)^+$ and 31 ± 15 $K^*(890)^0$ events in the $K^*(1420)^0$ region. The $I = \frac{1}{2}$ assignment for the $K^*(1420)^0$ requires equal $K^*(890)^+$ and $K^*(890)^0$ signals in this final state as observed.

To summarize the $K\pi\pi$ final state, we have observed a $K\pi\pi$ enhancement at 1420 and mainly decaying into the $K^*(890)\pi$ mode, whereas the $K^*(1300)^0$, observed in both 4.5 and 6 GeV/c, suggests a strong ρK mode. Since this reaction is nondiffractive, the observation of the well-defined narrow (~60 MeV) $K^*(1300)^0$ state without a large diffractive background event suggests that there is more than one state existing in the so-called "Q" region.

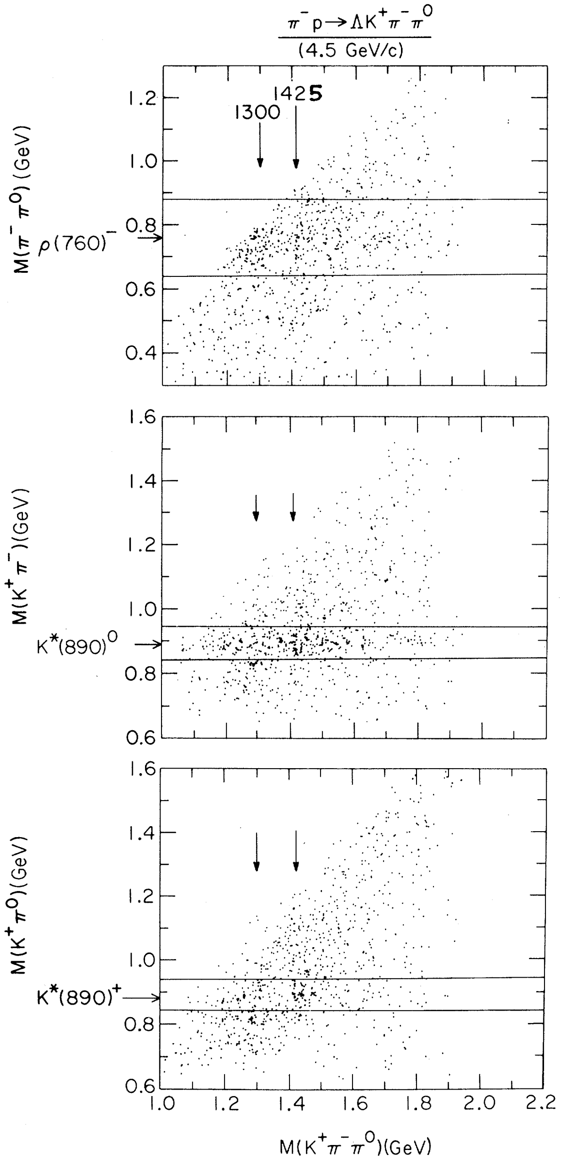

FIG. 42. Scatter plots of $\pi^-\pi^0$ and $K\pi$ mass vs $K^+\pi^-\pi^0$ mass from the reaction $\pi^-p \to \Lambda K^+\pi^-\pi^0$ at 4.5 GeV/c [$\Sigma(1385)^0$ removed and $\cos\theta^* \gtrsim 0.5$]. The lines indicate the limits for ρ and $K^*(890)$ mass regions (see text for details).

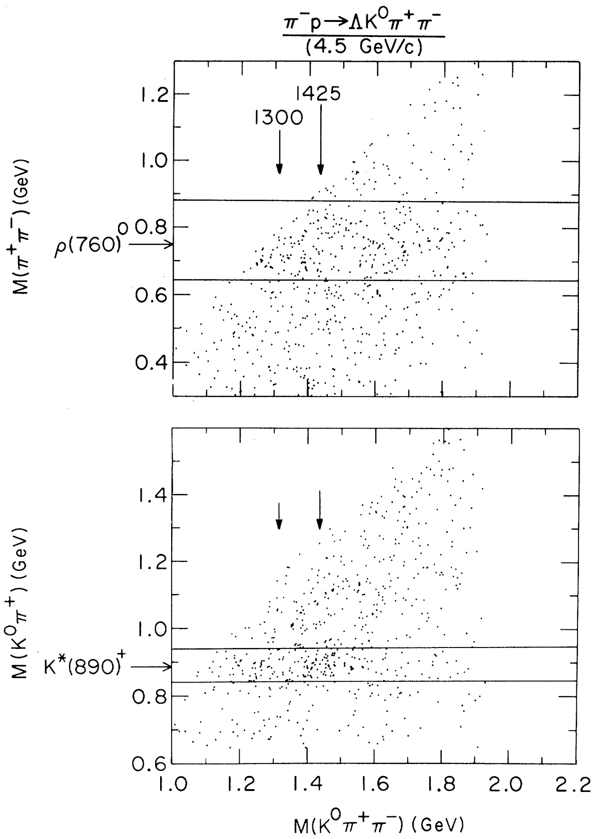

FIG. 43. Scatter plots of $\pi^+\pi^-$ and $K^0\pi^+$ mass vs $K^0\pi^+\pi^-$ mass from the reaction $\pi^-p \to \Lambda K^0\pi^+\pi^-$ at 4.5 GeV/c [$\Sigma(1385)^+$ removed and $\cos\theta^* \gtrsim 0.5$]. The lines indicate the limits for ρ and $K^*(890)$ mass regions (see text for details).

VI. REMARKS ON HYPERCHARGE EXCHANGE PROCESSES

In this section, we would like to remark on the general as well as markedly different features among the relevant hypercharge exchange reactions discussed in this study.

A. Comparison of $\pi^-p \to \Lambda K^0$, $\Lambda K^*(890)^0$, and $\Lambda K^*(1420)^0$

The production of K^0, $K^*(890)^0$, and $K^*(1420)^0$ exhibit forward peaks as well as backward peaks. In the forward scattering, the K^0 distribution is steeper ($b \sim 8$ GeV^{-2}) than either the $K^*(890)^0$ or the $K^*(1420)^0$ ($b \sim 2$ GeV^{-2}). There is no sign of forward dip in the K^0 production whereas a "flattening" effect is observed in the $K^*(890)^0$ production. Further, there is striking agreement between $(d\sigma/dt)(\pi^-p \to \Lambda K^0)$ – where only natural-parity contribution is allowed – and $(\rho_{11}+\rho_{1\,-1})(d\sigma/dt) \times(\pi^-p \to \Lambda K^*(890)^0)$ in shape as well as in magnitude for $|t'| \gtrsim 0.2$ GeV/c at 4.5 and 6 GeV/c as shown in Fig. 46. The difference in the natural-parity contribution to these two processes mainly comes from the region where $|t'| \lesssim 0.2$ GeV^2. We also present the Λ polarization due to the natural-parity contributions (derived from $S_\pm^2$; see Sec. IV) from these two processes as shown in Fig. 46(a). The marked disagreement in the $|t'| < 0.45$ GeV^2 and agreement in the $|t'| > 0.45$ GeV^2 are evident for the 4.5-GeV/c data [Fig. 46(a)].

In the backward region ($\hat{p}\cdot\hat{\Lambda} \sim -1.0$) any exchange must correspond to the quantum numbers of the Σ hyperon. Backward peaks are observed for K^0,

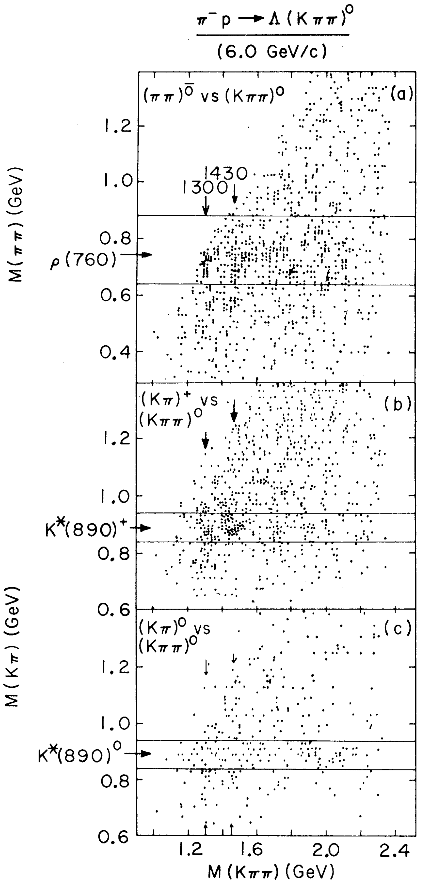

FIG. 44. Scatter plots of $\pi\pi$ and $K\pi$ mass vs $(K\pi\pi)^0$ mass from the reactions $\pi^-p\to\Lambda K^+\pi^-\pi^0$ and $\pi^-p\to\Lambda K^0\pi^+\pi^-$ at 6 GeV/c [$\Sigma(1385)$ removed]. The lines indicate the limits for ρ and $K^*(890)$ mass regions (see text for details).

$K^*(890)$, and $K^*(1420)^0$ production as shown in Figs. 2, 21, and 37. At 4.5 GeV/c the backward integrated cross sections ($-1.0<\hat{p}\cdot\hat{\Lambda}<-0.8$), with correction for all decay modes, are

$$\sigma(K^0)=1.0\pm0.25\ \mu\text{b}\,,$$

$$\sigma(K^*(890))=2.0\pm0.6\ \mu\text{b}\,,$$

$$\sigma(K^*(1420))=3.2\pm1.1\ \mu\text{b}\quad\text{(Ref. 22)}\,.$$

In contrast to the forward cross sections, the backward $K^*(890)^0$ and $K^*(1420)^0$ cross sections are as large or larger than the backward K^0 cross section.

B. Comparison of $\pi^-p\to\Sigma^0K^0$ and $\Sigma^0K^*(890)^0$

These Σ^0 final states resemble the Λ final states discussed in Sec. VI A. In both cases K^0 production shows forward peaking while $K^*(890)^0$ production shows flattening in the forward direction. Furthermore,

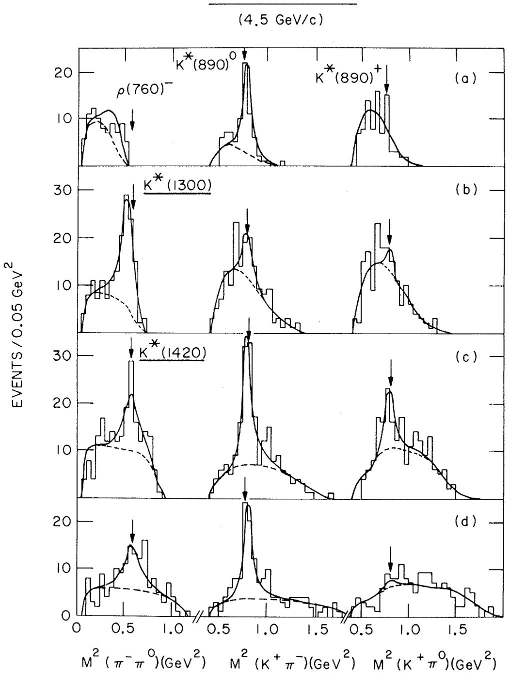

FIG. 45. $\pi^-\pi^0$, $K^+\pi^-$, and $K^+\pi^0$ mass squared projections for various $(K\pi\pi)^0$ masses from the reaction $\pi^-p\to\Lambda K^+\pi^-\pi^0$ at 4.5 GeV/c [$\Sigma(1385)^0$ removed and $\cos\theta^*\geq0.5$]. $(K\pi\pi)^0$ mass limits are (a) 1.12–1.24, (b) 1.24–1.36, (c) 1.36–1.48, and (d) 1.48–1.60, all in GeV. Central values of the ρ and $K^*(890)$ are indicated by arrows. Solid curves represent fit to the Dalitz plot. Dashed curves represent background in each mass spectrum from phase space and reflections of other resonances.

$$(\rho_{11}+\rho_{1\,-1})\frac{d\sigma}{dt}(\pi^-p\to\Sigma^0K^*(890)^0)\approx\frac{d\sigma}{dt}(\pi^-p\to\Sigma^0K^0)$$

for $|t'|\gtrsim0.2$ GeV^2 [Fig. 46(c)],

a behavior similar to the corresponding Λ reactions.

C. Comparison of $K^+\pi^-$ Asymmetry in $\pi^-p\to\Lambda K^+\pi^-$ and $\Sigma^0K^+\pi^-$

The $K^+\pi^-$ asymmetry $\langle D^1_{00}\rangle$ as a function of $K^+\pi^-$ mass is displayed in Fig. 47 for the reaction $\pi^-p\to\Lambda K^+\pi^-$ at 4.5 and 6.0 GeV/c and for $\pi^-p\to\Sigma^0K^+\pi^-$ at 4.5 GeV/c for $|t'|<0.5$ GeV^2. The angle defined in the $K\pi$ rest frame is $\hat{\pi}^-_{\text{beam}}\cdot\hat{K}^+$. The asymmetry goes through zero at both the $K^*(890)^0$ and $K^*(1420)^0$ regions for $\pi^-p\to\Lambda K^+\pi^-$ at 4.5 GeV/c. The simplest explanation of this behavior is that there is s-p wave interference in the $K^*(890)^0$ region with the s-wave phase shift rather constant and p-d wave interference in the $K^*(1420)^0$ region with the p-wave phase shift rather constant. The 6-GeV/c data show similar behavior.

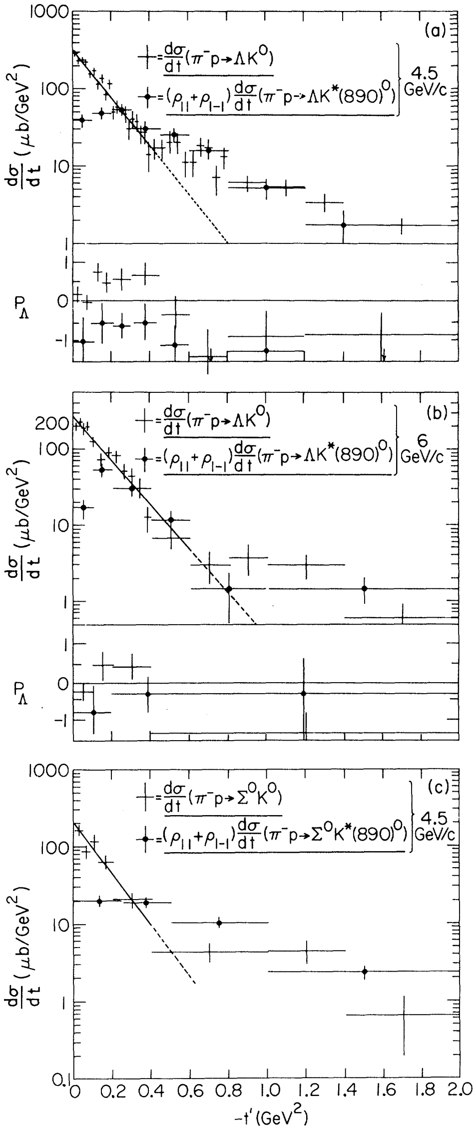

FIG. 46. (a) Comparison of differential cross section and Λ polarization reaction (1a) with the natural-parity-exchange contribution to the differential cross section and Λ polarization for reaction (2a) at 4.5 GeV/*c*. (b) Similar comparison for 6 GeV/*c*. (c) Similar comparison for Σ^0 final states at 4.5 GeV/*c*. Natural-parity Λ polarization for reaction (2a) is $(S_+^2-S_-^2)/(S_+^2+S_-^2)$ [see Eqs. (14) and (15) in text].

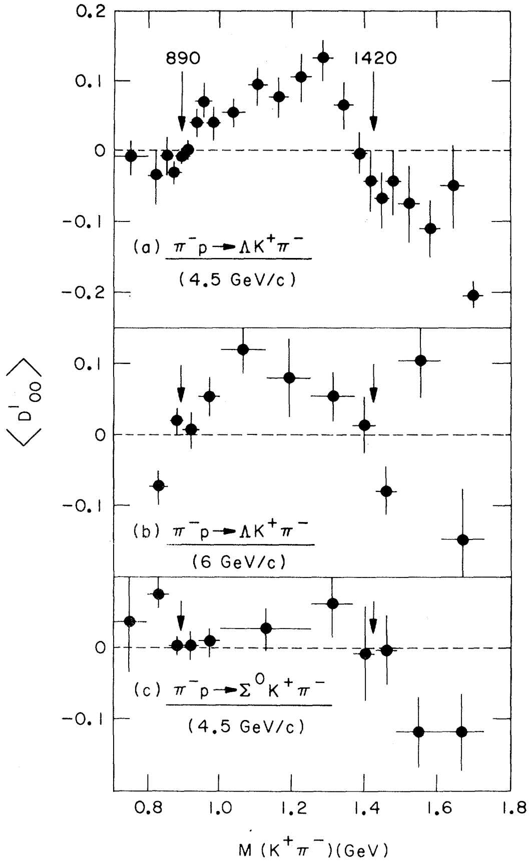

FIG. 47. $K^+\pi^-\langle D^1_{00}\rangle$ moment for reaction $\pi^-p\to\Lambda K^+\pi^-$ at 4.5 and 6 GeV/*c* and reaction $\pi^-p\to\Sigma^0K^+\pi^-$ at 4.5 GeV/*c*, all for $|t'|<0.5$ GeV^2.

D. Comparison of $\pi^-p\to\Lambda K^0$, $\Lambda(1405)K^0$, and $\Lambda(1520)K^0$

Strong Λ(1405) and Λ(1520) production is observed in the $\pi^-p\to\Sigma^\pm\pi^\mp K^0$ data at 4.5 GeV/*c* (Fig. 48). In calculating the differential cross section for $\pi^-p\to\Lambda(1405)K^0$ (Fig. 49 and Table XXI) we excluded the biased $\Sigma^+\to p\pi^0$ decays. Lifetime corrections were applied to the remaining Σ's and to the K^0's. Strong Λ(1520) production is also seen in $\pi^-p\to pK^-K^0$ (Fig. 50). The corrected differential cross section for the Λ(1520) from the K^-K^0p final state is shown in Fig. 51 and Table XXII. The slope parameters and total cross sections for Λ(1405) and Λ(1520) production are shown in Table I. Again the Λ(1405) and Λ(1520) are produced with much less steepness ($b\simeq 2$ GeV^{-2}) in comparison with that ($b\simeq 8$ GeV^{-2}) of Λ production. This is particularly interesting because the same exchange [K^*(890) and K^*(1420)] is required in all three reactions. In the context of exchange degeneracy, a measurement of the forward scattering cross section at $\hat{\pi}^-\cdot\hat{K}^0\approx 1$ represents a determination of the spin-nonflip ratio of $g_{\Lambda K^*\bar{p}}{}^2 : g_{\Lambda(1405)K^*\bar{p}}{}^2 : g_{\Lambda(1520)K^*\bar{p}}{}^2$, where Λ, Λ(1405), and Λ(1520) belong to different SU_3 multiplets. Experimentally, we obtain

318 ± 12 μb/GeV^2 for ΛK^0,

32 ± 7 μb/GeV^2 for $\Lambda(1405)K^0$,

60 ± 13 μb/GeV^2 for $\Lambda(1520)K^0$

at $\hat{\pi}^-\cdot\hat{K}^0\approx 1$.

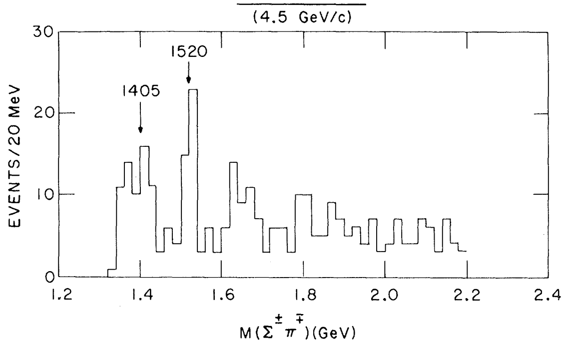

FIG. 48. $\Sigma^\pm\pi^\mp$ mass spectrum from the reactions $\pi^- p \to \Sigma^\pm\pi^\mp K_S^0$ at 4.5 GeV/*c*.

E. Comparison of $\pi^- p \to \Sigma^0 K^0$ and $\Sigma(1385)^0 K^0$

The $\Sigma(1385)^0$ production is observed in the $\Lambda^0 K^0 \pi^0$ final state at 4.5 GeV/*c* as shown in Fig. 52. The corrected differential cross section, Fig. 53 and Table XXIII, is less steep ($b \simeq 2$ GeV^{-2}) than the $\Sigma^0 K^0$ slope ($b \simeq 7$ GeV^{-2}). The forward differential scattering cross sections ($\hat{\pi}^- \cdot \hat{K}^0 \approx 1$) are

$$\frac{d\sigma}{dt}(\pi^- p \to \Sigma^0 K^0) = 186 \pm 28\ \mu\text{b/GeV}^2\,,$$

$$\frac{d\sigma}{dt}(\pi^- p \to \Sigma(1385)K^0) = 29 \pm 6\ \mu\text{b/GeV}^2\,.$$

Assuming $K^*(890)^0$ and $K^*(1420)^0$ exchange degeneracy in the forward direction, the above values give

$$g_{\Sigma K^* \bar{p}}^2 / g_{\Sigma(1385) K^* \bar{p}}^2 = 6.4 \pm 1.6\,.$$

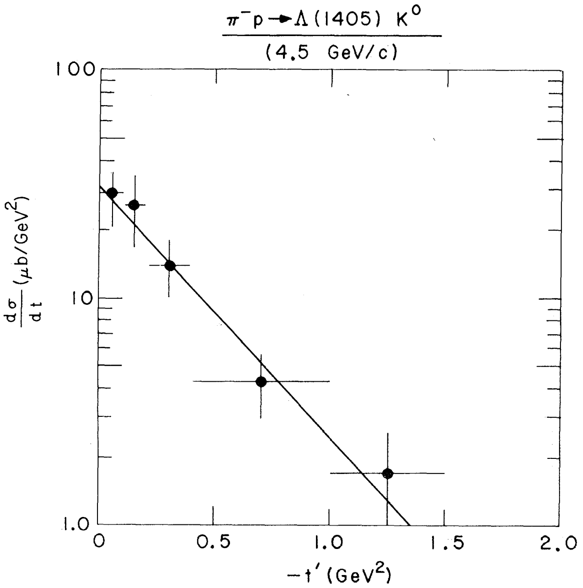

FIG. 49. Differential cross section for reaction (4) at 4.5 GeV/*c*. Curve represents fit shown in Table I.

TABLE XXI. Differential cross section for $\pi^- p \to \Lambda(1405)K^0$ [$\Lambda(1405) \to$ all] at 4.5 GeV/*c*.

$-t'$ (GeV^2)	$\Lambda(1405) \to \Sigma^\pm\pi^\mp$ events	$\frac{d\sigma}{dt}$ (μb/GeV^2)
0–0.1	12	29 ± 8
0.1–0.2	9	26 ± 9
0.2–0.4	11	14 ± 4
0.4–1.0	9	4.3 ± 1.4
1.0–1.5	3	1.7 ± 0.9

VII. "FORBIDDEN" PERIPHERAL SCATTERING FROM THE REACTION $\pi^- p \to \Sigma(1385)^- K^+$

Since there has been no strong experimental evidence for an $I = \frac{3}{2}$ $K\pi$ resonance from production experiments, the observation of the "forbidden" peripheral scattering[23] of K^+ from $\pi^- p \to \Sigma(1385)^- K^+$ has renewed the interest and speculation concerning its possible existence.[24] However, this "forbidden" scattering has been given other interpretations such as kinematic reflections in the $\Lambda K^+ \pi^-$ final state, *s*-channel resonances, and two-particle (for example, $K^\pm$, $\pi^\pm$ or $\rho^\pm$, $K^{*\pm}$) exchange in the *t* channel.[25] In this section we present the evidence of this "forbidden" forward reaction: $\pi^- p \to \Sigma(1385)^- K^+$ at 4.5 GeV/*c*.[26] We cannot explain these results by a simple kinematic reflection in our data. The shape of the differential cross section at this energy, when compared with those at lower energies, suggests that an *s*-channel resonance is not a likely interpretation for this effect. We also present the upper limit of the cross section for this "forbidden" forward scattering at 6 GeV/*c*. These data lead to an energy dependence of the cross section for this peak of $s^{-3.7\pm0.4}/\ln s$ for incident π^- momenta from ~2 to 6 GeV/*c* ($s \simeq 5$ to 10 GeV^2).

The Dalitz plots and mass-squared projections for the $\Lambda K^+ \pi^-$ and $\Sigma^0 K^+ \pi^-$ final state at 4.5 GeV/*c*

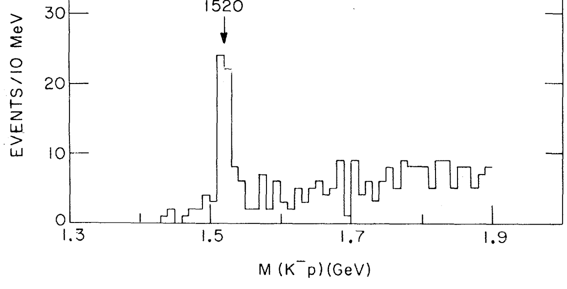

FIG. 50. $K^- p$ mass spectrum from the reaction $\pi^- p \to p K^- K_S^0$ at 4.5 GeV/*c*.

TABLE XXII. Differential cross section for $\pi^- p \to \Lambda(1520)K^0$ [$\Lambda(1520) \to$ all] at 4.5 GeV/c.

$-t'$ (GeV^2)	$\Lambda(1520) \to K^- p$ visible events	$\frac{d\sigma}{dt}$ (μb/GeV^2)
0–0.2	17	40 ± 10
0.2–0.4	17	40 ± 10
0.4–0.8	10	12 ± 4
0.8–1.4	5	4 ± 2
1.4–2.0	2	1.6 ± 1.1

are shown in Figs. 54 and 55. The $K^*(890)^0$ and $K^*(1420)^0$ bands, as noted before, are the dominant feature of these reactions. Therefore to search for $\Sigma(1385)^-$ production, events in the K^* bands (0.84 to 0.96 GeV and 1.34 to 1.48 GeV as shown in the Dalitz plots) must be removed from the subsequent analysis. A marked enhancement in the $\Lambda\pi^-$ mass spectrum is evident after removal of K^*'s [solid region in Fig. 54(a)].[27] This enhancement does not depend on the exact choice of the limits of these K^* bands and thus it is not associated with the K^*'s. We identify this enhancement with the $\Sigma(1385)^-$ since the fitted mass of 1392 ± 8 MeV and width of 32^{+16}_{-10} MeV are in good agreement with the established values for this resonance. There is no similar structure in the $\Sigma^0\pi^-$ mass spectrum [Fig. 55(a)], a point which will be discussed later.

To investigate how the $\Sigma(1385)^-$ is produced at 4.5 GeV/c, the $\Lambda\pi^-$ mass-squared distributions are shown in Fig. 54(b) for different selections of $\hat{\pi}^- \cdot \hat{K}^+$. The forward ($\hat{\pi}^- \cdot \hat{K}^+ \sim +1$) and backward ($\hat{\pi}^- \cdot \hat{K}^+ \sim -1$) scatterings dominate the angular distribution. The cross section in the "forbidden" forward hemisphere ($0 \leq \hat{\pi}^- \cdot \hat{K}^+ \leq 1$) corresponds to 0.9 ± 0.25 μb and can be described by e^{bt} with $b = 2 \pm 1$ GeV^{-2} for $|t| < 0.5$ GeV^2. The upper limit for the similar cross section at 6 GeV/c is 0.3 μb at the 99% confidence level. Because the forward scattering of the K^+ in the reaction $\pi^- p \to \Sigma(1385)^- K^+$ cannot be explained by the exchange of any single known particle in the t channel, we must, therefore, consider other possible explanations of this peripheral K^+ production as follows:

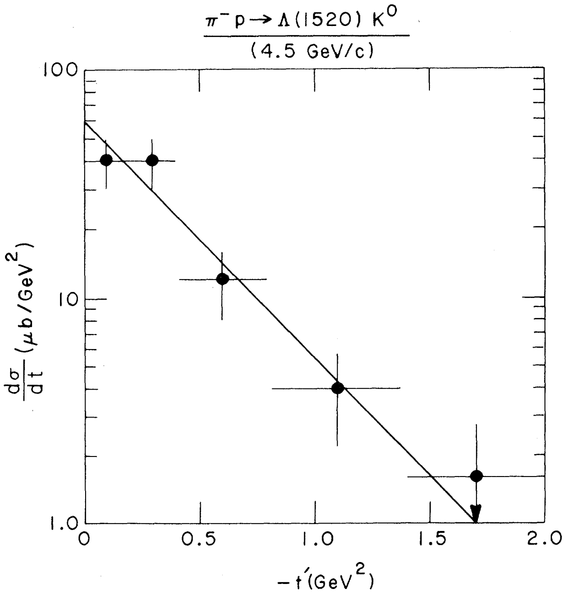

FIG. 51. Differential cross section for reaction (5) at 4.5 GeV/c. Curve represents fit shown in Table I.

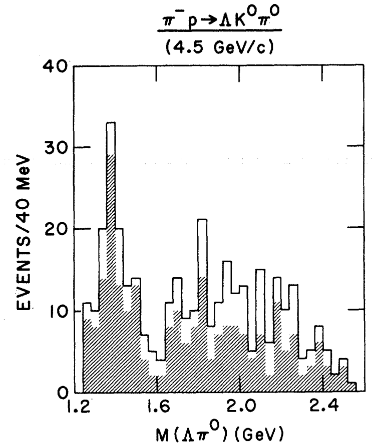

FIG. 52. $\Lambda^0\pi^0$ mass spectrum from the reaction $\pi^- p \to \Lambda K^0 \pi^0$ at 4.5 GeV/c. Shaded region remains after subtracting events in the $K^*(890)^0$ region: $0.79 < M(K^+\pi^-) < 0.99$ GeV.

1. *Kinematic effect.* Unlike broad resonances such as $\Delta(1238)$, the $\Lambda\pi^-$ peak is narrow (~35 MeV) and well defined (1392 ± 8 MeV), and in general is difficult to generate by a kinematic reflection of $K\pi$ scattering without invoking other final-state in-

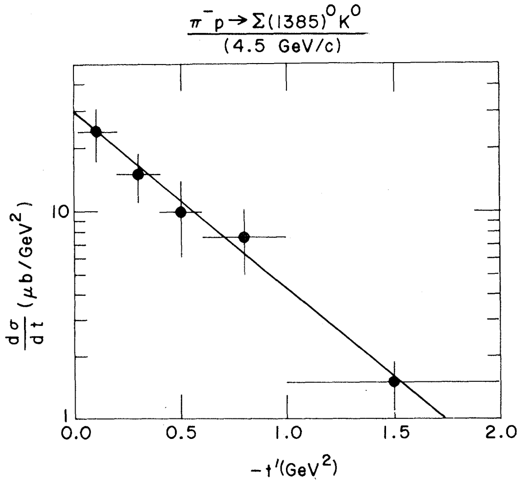

FIG. 53. Differential cross section for reaction (6) at 4.5 GeV/c. Curve represents fit shown in Table I.

TABLE XXIII. Differential cross section for $\pi^- p \to \Sigma(1385)^0 K^0$ [$\Sigma(1385)^0 \to$ all] at 4.5 GeV/c.

$-t'$ (GeV^2)	$\Sigma(1385)^0 \to \Lambda\pi^0$ visible events	$\frac{d\sigma}{dt}$ (μb/GeV^2)
0–0.2	26 ± 7	24 ± 7
0.2–0.4	16 ± 4	15 ± 4
0.4–0.6	11 ± 4	10 ± 4
0.6–1.0	17 ± 5	7.6 ± 2.6
1.0–2.0	8 ± 3	1.5 ± 0.4

teractions. For example, the calculations of Berger[28] predict a width for the $\Lambda\pi^-$ peak due to kinematic reflection of the order of 200 MeV. In this respect, we have examined the $K^+\pi^-$ angular distributions as a function of $K^+\pi^-$ mass for both $\Lambda K^+\pi^-$ and $\Sigma^0 K^+\pi^-$ final states. These distributions, found in terms of $K^+\pi^-$ moments, $\langle D^1_{00}\rangle$, for events outside the $K^*(890)^0$ and $K^*(1420)^0$ regions, are similar for the $\Lambda K^+\pi^-$ and $\Sigma^0 K^+\pi^-$ final states [Figs. 47(a) and 47(c)]. Therefore, a relevant test can be made in the reaction $\pi^- p \to \Sigma^0 K^+\pi^-$: If there were kinematic reflections producing the $\Lambda\pi^-$ peak in the reaction $\pi^- p \to \Lambda K^+\pi^-$, the same mechanism would produce a $\Sigma^0\pi^-$ peak in the reaction $\pi^- p \to \Sigma^0 K^+\pi^-$. With no final-state interaction, the magnitude should be proportional to the number of events in the $\Sigma^0 K^+\pi^-$ final state and the mass perhaps displaced from the $\Sigma^-(1385)$. However, the absence of a $\Sigma^0\pi^-$ peak (where eight events are expected above background and none is seen) in the $\Sigma^0 K^+\pi^-$ final state, as shown in Fig. 54(c), suggests that the $\Lambda\pi^-$ peak is not due to this kinematic effect, and is indeed the $\Sigma(1385)^-$. From the established branching ratio $\Sigma(1385)^- \to (\Sigma^0\pi^-)/(\Lambda\pi^-)$, we expect that less than two $\Sigma^0\pi^-$ events can be due to $\Sigma(1385)^-$. This is certainly consistent with

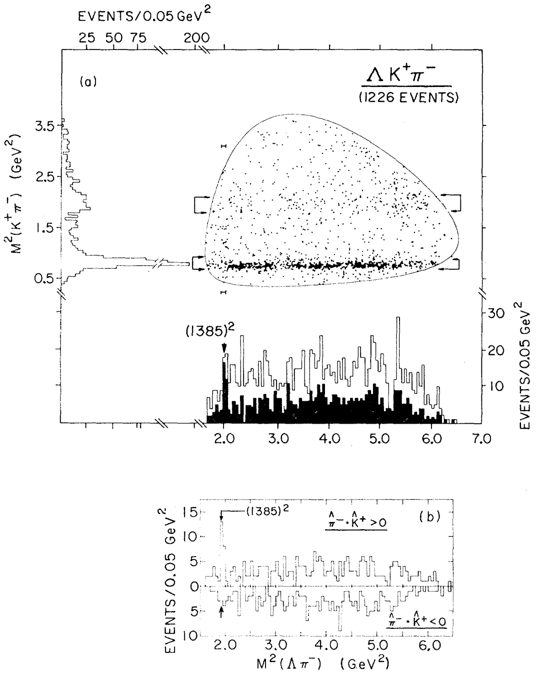

FIG. 54. (a) Dalitz plot and mass projections for the $\Lambda K^+\pi^-$ final state at 4.5 GeV/c. Solid histogram is for events outside the $K^*(890)^0$ and $K^*(1420)^0$ bands. (b) Mass-squared projections for $\Lambda\pi^-$ for different selections of $\hat{\pi}^- \cdot \hat{K}^+$ as shown.

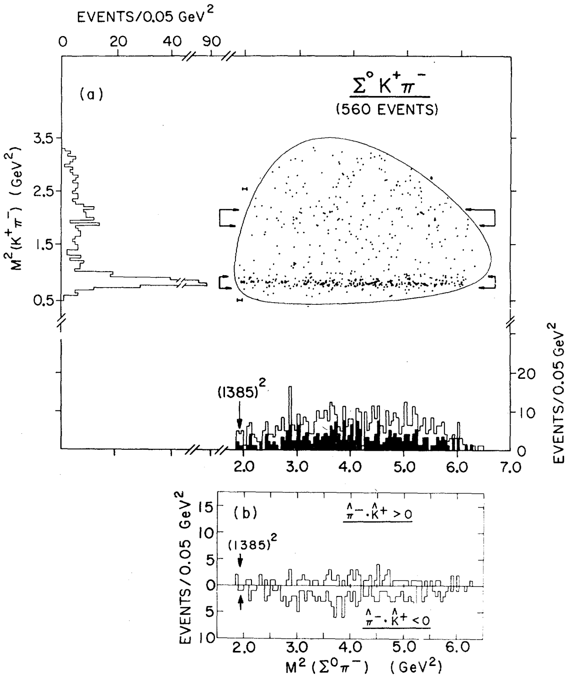

FIG. 55. (a) Dalitz plot and mass projections for the $\Sigma^0 K^+\pi^-$ final state at 4.5 GeV/c. Solid histogram is for events outside the $K^*(890)^0$ and $K^*(1420)^0$ bands. (b) Mass-squared projections for $\Sigma^0\pi^-$ for different selections of $\hat{\pi}^- \cdot \hat{K}^+$ as shown.

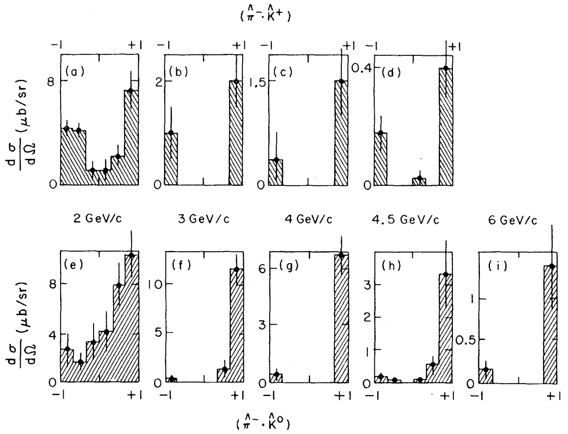

FIG. 56. (a)–(d) $d\sigma[\pi^- p \to \Sigma(1385)^- K^+]/d\Omega$ for incident pion momenta of 2–4.5 GeV/c. (e)–(i) $d\sigma[\pi^- p \to \Sigma(1385)^0 K^0]/d\Omega$ for incident pion momenta of 2–6 GeV/c. Data for 2–4 GeV/c come from Ref. 23.

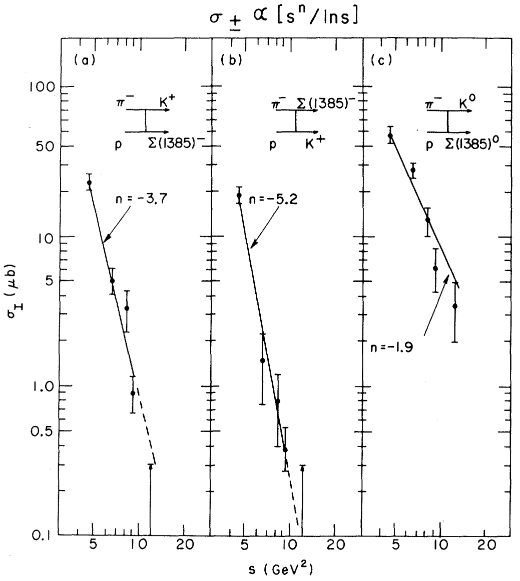

FIG. 57. Integrated cross sections σ_I vs s. Solid lines are the fit to the data as shown. See text for details.

our observation.

We have also examined the distribution of the angle between the target proton and the Λ in the $\Sigma(1385)^-$ rest frame (not shown) and found it to be symmetric. This distribution is again not consistent with a kinematic reflection.

We conclude that a simple kinematic reflection due to $K^+\pi^-$ scattering is not consistent with our observation without invoking an additional final-state interaction between π^- and Λ, as suggested by Berger.[28] This additional assumption, of course, is somewhat indistinguishable from two-particle exchange in the t channel, a possibility which we discuss later.

2. *s-channel resonance(s).* A single s-channel isobar could produce both the forward and backwark peaking in the reaction $\pi^-p \rightarrow \Sigma(1385)^-K^+$ and $\Sigma(1385)^0K^0$. In the reaction $\pi^-p \rightarrow \Sigma(1385)^0K^0$ at 4.5 GeV/c, the K^0 production angular distribution,[29] Fig. 56(h), shows a strong forward ($\hat{\pi}^- \cdot \hat{K}^0 \sim +1$) signal but with no backward peak ($\hat{\pi}^- \cdot \hat{K}^0 \sim -1$). This is not in good agreement with the $\Sigma(1385)^-K^+$ angular distribution[29,30] [Fig. 56(d)]. Therefore a single s-channel resonance interpretation is not a likely one. However, many isobars are reported in this mass region and the different behavior of angular distributions between $\Sigma(1385)^-K^+$ and $\Sigma(1385)^0K^0$ may be explained by complicated interference effects among the isobars. We see no s dependence in the angular distributions of $\pi^-p \rightarrow \Sigma(1385)^-K^+$ and $\Sigma(1385)^0K^0$ in Fig. 56 above 2 GeV/c, indicating the t-channel and u-channel exchanges to be the simplest description from the duality[9] point of view. To support this conjecture, the energy behavior of cross sections in the "forbidden" forward hemisphere and the "allowed" backward hemisphere from $\pi^-p \rightarrow \Sigma(1385)^-K^+$, and in the "allowed" forward hemisphere from $\pi^-p \rightarrow \Sigma(1385)^0K^0$, for incident pion momenta ~2 to 6 GeV/c, are shown in Figs. 57(a), 57(b), and 57(c), respectively. The data are fitted well with the form $s^n/\ln s$,[31] where $n_1 = -3.7 \pm 0.4$ for the forward "forbidden," $n_2 = -5.2 \pm 0.5$ for the backward "allowed," and $n_3 = -1.9 \pm 0.3$ for the forward "allowed" reactions.[32] The last two values are in agreement with the "hyperon"-exchange and "meson"-exchange behavior deduced from other processes.[33] We therefore suggest that the forward K^+ production, above 2 GeV/c π^- incident momentum, can be best described by a t-channel and not an s-channel effect.

It is interesting to note that the s dependence for the differential cross section at the forward direction for $\pi^-p \rightarrow \Sigma^-K^+$ is steep ($\sim s^{-11}$) and has been attributed to an s-channel $\Delta(1950)$ effect.[34] In this connection, the s-dependence of the forward cross section for $\pi^-p \rightarrow \Sigma(1385)^-K^+$ is, however, less steep ($\sim s^{-4}$).

3. *Two-particle or single exotic exchange in t channel.* Experimentally these two possibilities are difficult to distinguish from each other. From the simple Regge-pole model, the cross section for the forward hemisphere can be expressed as $s^{2\alpha_0 - 2}/\ln s$, where α_0 is the value of a Regge trajectory at $t = 0$ in the Chew-Frautschi plot.[31] From Fig. 57(a) we obtain the experimental value $\alpha_0 = -0.9 \pm 0.2$. If this "forbidden" forward peak is indeed due to a single $I = \frac{3}{2}$ "exotic" meson exchange, then this may imply an exotic meson having a mass of ~1.0 (1.4) GeV for $J^P = 0^+$ (1^-) assuming the slope of the trajectory to be 1.

For two-particle or "cut" contribution in the t channel,[25] α_0 takes a form of $(\alpha_0^1 + \alpha_0^2) - 1$, where α_0^1 and α_0^2 are the values of two possible trajectories at $t = 0$. For the examples $(\pi^\pm, K^\pm)$ and $(\rho^\pm, K^{*\pm})$, $\alpha_0(\pi^\pm, K^\pm) \simeq -1.25$ and $\alpha_0(\rho^\pm, K^{*\pm}) \simeq -0.4$. The large error in the experimental α_0 precludes any positive identification of which one if either of these examples of two-particle exchanges may be responsible for the K^+ forward scattering.[35] However, for $(\pi^\pm, K^\pm)$ exchange, one would expect the slope b of the differential cross section to be steep in disagreement with what we observe ($b = 2 \pm 1$), whereas for $(\rho^\pm, K^{*\pm})$ exchange,[25] the slope would be about 4, which is not incompatible with our result. More data, particularly at higher energies, should be able to answer these questions.

To summarize, we have observed the "forbidden" forward scattering of K^+ from the reaction $\pi^-p \rightarrow \Sigma(1385)^-K^+$. This forward peak cannot be explained by kinematic reflections of the $K^+\pi^-$ final state. The $\Sigma(1385)^-K^+$ angular distribution at 4.5 GeV/c as well as those from lower energies suggest that this peak is not due to s-channel effects. We therefore have to face the possibility of either two-particle or a single "exotic" exchange in the t channel to describe the production of the "forbidden" peripheral peak. In any case, more data are needed for this reaction, $\pi^-p\to\Sigma(1385)^-K^+$ and, in particular, the line-reversed reaction $K^-p\to\Sigma(1385)^-\pi^+$ in order to compare their energy dependences and angular distributions.[36]

VIII. CONCLUDING REMARKS

To summarize the study presented in this paper, we note the following important points.

(i) $\pi^-p\to\Lambda K^0$. Both the differential cross section and the Λ polarization exhibit a characteristic change at $-t\simeq 0.4$ GeV^2, namely a dip in the differential cross section and a zero in the Λ polarization from a large positive value to a large negative value. These features do not show up in the $\bar{K}n\to\Lambda\pi$ reaction where the exchange in the t-channel, $K^*(890)$ and $K^*(1420)$, is identical. Thus the simple and attractive concept of exchange degeneracy between these two K^*'s does not seem to work in the forward direction in the energy range available thus far. Further measurements of differential cross sections and Λ polarization of these two reactions at higher energy are needed to test the concept of the exchange degeneracy. These reactions are particularly suitable because no $I=\frac{3}{2}$ exchange is present in the t channel.

(ii) $\pi^-p\to\Lambda K^*(890)^0$. The analysis presented for $\pi^-p\to\Lambda K^*(890)^0$ shows a striking correlation between the Λ and $K^*(890)^0$ decays. The data can be interpreted as indicating natural- and unnatural-parity-exchange contributions both producing strong Λ polarization, negative (positive) for natural- (unnatural-) parity exchange. This behavior cannot be explained by a simple model with exchanges of K and the exchange-degenerate pair $K^*(890)$ and $K^*(1420)$. Absorption or additional trajectories are required. We have only been able to obtain a rough value of the phase between the two most important amplitudes A_+ and S_-.

(iii) $\pi^-p\to\Lambda K^*(1420)^0$. We observe s-wave and d-wave contributions in the $K^*(1420)^0\to K\pi$ mass region. A study of s-d wave interference suggests the s wave and resonating d wave have the same phase at the resonance mass for $t'<0.5$ GeV^2. This has also been observed in a different reaction, $K^-p\to nK^*(1420)^0$.[20] However, even though an s-wave resonant behavior is not required with the present data, we cannot rule out that possibility.

(iv) $\pi^-p\to\Lambda K^*(1300)^0$. A narrow, ~60 MeV, well-defined peak is observed in the 1300-MeV region in both 4.5- and 6-GeV/c data. Since this $K^*(1300)^0$ is produced via nondiffractive process at both momenta, it cannot be produced by any known kinematic process, such as the Deck effect. Furthermore, the $K^*(1300)^0$ seems to decay strongly into the ρK mode in our data. Therefore it is reasonable to assume that there exists more than one state in the Q region. The nondiffractive process, such as the one studied here, is most suitable for studying the resonance properties of this state. Since the Λ is not produced very peripherally ($d\sigma/dt\sim e^{2t}$) in this reaction, a counter-spectrometer approach to accumulate large statistics for this state is feasible.

(v) $\pi^-p\to\Sigma(1385)^-K^+$. We have observed the K^+ forward scattering from the reaction $\pi^-p\to\Sigma(1385)^-K^+$ at 4.5 GeV/c. The narrow, 32^{+16}_{-10}-MeV, well-defined $\Sigma(1385)^-\to\Lambda\pi^-$ cannot be explained by any known kinematic reflection process or simple s-channel effect. We, therefore, have to face the fact that there exists an $I=\frac{3}{2}$ "exotic" amplitude in the t channel. Experimentally it is difficult to distinguish whether it corresponds to a two-particle or a single exotic exchange in the t channel. More data are needed in this reaction as well as the line-reversed reaction $K^-p\to\Sigma(1385)^-\pi^+$ in order to compare their angular distributions and energy dependences.

ACKNOWLEDGMENTS

We wish to thank many individuals who have contributed to the completion of this study. At BNL, we thank Dr. N. P. Samios and Dr. R. P. Shutt for their interest in this experiment; Dr. M. S. Webster for the design of the 6-GeV/c beam; Dr. J. Louie for his contribution to the study of the reaction $\pi^-p\to\Lambda K^0$; Dr. S. U. Chung for helpful discussions concerning interference phenomena in the $K^*(1420)^0\to K\pi$ decay; Dr. R. D. Field for useful discussions and his enthusiastic interest in our data. The generous help from the AGS staff and the 80-in. bubble-chamber operating crews are greatly appreciated. The data-processing efforts from the BNL data-reduction personnel were essential to the successful completion of this experiment. The 4.5-GeV/c film was obtained from SLAC. We would like to acknowledge the assistance and cooperation from Dr. W. K. H. Panofsky, Dr. J. Ballam, Dr. J. Murray, Dr. R. Gearhart, and R. Watt.

---

*Work performed under the auspices of the U. S. Atomic Energy Commission.

[1] Previous work on the reactions $\pi^-p \rightarrow \Lambda K^0$ and $\pi^-p \rightarrow \Sigma^0 K^0$ can be found as follows. 1.5–4.2 GeV/c: O. I. Dahl *et al.*, Phys. Rev. 163, 1430 (1967) (see for earlier references). 3.9 GeV/c: M. Abramovitch *et al.*, Nucl. Phys. B27, 477 (1971). 8, 10.7 GeV/c: S. Ozaki *et al.*, BNL report, presented at the Fifteenth International Conference on High-Energy Physics, Kiev, U.S.S.R., 1970 (unpublished). 11.2 GeV/c: B. Bertolucci *et al.*, Lett. Nuovo Cimento 2, 149 (1969).

[2] The Λ polarization is

$$P_\Lambda = \frac{3}{\alpha_\Lambda} \sum_{i=1}^{n} \cos\theta_i\, \omega_i / \Sigma\omega_i ;$$

$\cos\theta = \hat{p} \cdot \hat{n}$; $\hat{p}$ is a unit vector along direction of proton in Λ rest frame; $\hat{n}$ is the production normal $\hat{\pi}^-_{\text{beam}} \times \hat{K}^0$; ω_i is the weight of each event. We use $\alpha_\Lambda = 0.645$ (see Ref. 13).

[3] For $K^-n \rightarrow \Lambda\pi^-$ and $K^-n \rightarrow \Sigma^0\pi^-$ reactions: 3 GeV/c: SABRE collaboration, Nucl. Phys. B9, 493 (1969). 3.6, 3.9 GeV/c: D. J. Crennell *et al.*, Phys. Rev. Letters 23, 1347 (1969); and unpublished results. 4.5 GeV/c: W. L. Yen *et al.*, Phys. Rev. Letters 22, 963 (1969). 5, 5.5, 13 GeV/c: B. Musgrave, *Phenomenology in Particle Physics, 1971,* edited by C. B. Chiu *et al.* (California Institute of Technology, Pasadena, Calif., 1971), p. 505; and unpublished results.

For $K^-p \rightarrow \Lambda\pi^0$ reactions: 2 GeV/c: G. R. Kalbfleisch, Brookhaven National Laboratory, unpublished results. 2.24 GeV/c: G. W. London *et al.*, Phys. Rev. 143, 1034 (1966). 3 GeV/c: J. Badier *et al.*, in *Proceedings of the Twelfth International Conference on High-Energy Physics, Dubna, 1964* (Atomizdat, Moscow, 1966), p. 650. 3.5 GeV/c: Birmingham-Glasgow-London (I.C.)-Oxford-Rutherford collaboration, Phys. Rev. 152, 1148 (1966). 3.9, 4.65 GeV/c: M. Aguilar-Benitez, S. U. Chung, R. L. Eisner, and N. P. Samios, Phys. Rev. D 6, 29 (1972). 3.95 GeV/c: L. Moscoso *et al.*, Nucl. Phys. B36, 332 (1972). 4.1, 5.5 GeV/c: D. D. Reeder, University of Wisconsin, unpublished results.

For $K_L^0 p \rightarrow \Lambda\pi^+$ reactions: 2–8 GeV/c: A. D. Brody *et al.*, SLAC Report No. SLAC-PUB-823 (unpublished).

[4] For an earlier experimental review, see, for example, K. W. Lai and J. Louie, Nucl. Phys. B19, 205 (1970).

[5] See, for example, A. C. Irving, A. D. Martin, and C. Michael, Nucl. Phys. B32, 1 (1971); R. D. Field, Jr. and J. D. Jackson, Phys. Rev. D 4, 693 (1971).

[6] S. M. Pruss *et al.*, Phys. Rev. Letters 23, 189 (1969).

[7] C. Michael and R. Odorico, Phys. Letters 34B, 422 (1971).

[8] Calculated by moments using $P_{\Sigma^0} = -(9/\alpha_\Lambda)\langle(\hat{n}\cdot\hat{q}) \times (\hat{q}\cdot\hat{K})\rangle$, where $\vec{\mathrm{n}} = \vec{\mathrm{p}} \times \vec{\Sigma}^0$, $\hat{q}$ is unit vector in direction of Λ in Σ^0 rest frame, and $\hat{K}$ is unit vector in direction of proton in Λ rest frame. See, e.g., R. Gatto, Phys. Rev. 109, 610 (1958).

[9] For a review see J. D. Jackson, Rev. Mod. Phys. 42, 12 (1970).

[10] See, for example, E. L. Berger and G. C. Fox, Phys. Rev. Letters 25, 1783 (1970).

[11] D. J. Crennell, K. W. Lai, J. M. Scarr, and T. G. Schumann, Phys. Rev. Letters 19, 1212 (1967), and D. J. Crennell, K. W. Lai, J. Louie, J. M. Scarr and W. H. Sims, *ibid.* 25, 187 (1970).

[12] See, for example, H. Pilkuhn, *The Interactions of Hadrons* (North-Holland, Amsterdam, 1967), p. 237.

[13] Particle Data Group, Rev. Mod. Phys. 43, S1 (1971).

[14] N. Byers and C. N. Yang, Phys. Rev. 135, B796 (1964).

[15] This association of $S_\pm{}^2$ and $D_\pm{}^2$ with, respectively, natural- and unnatural-parity exchanges is only approximate, even in the absence of absorptive effects, because of the small value reached by $|\cos\theta_t|$, the t-channel scattering angle at this energy. See, for example, G. Cohen-Tannoudji, Ph. Salin, and A. Morel, Nuovo Cimento 55A, 412 (1968).

[16] In the s-channel frame, $A_+{}^2$ falls rapidly with increasing $|t'|$ and because of the invariance of $(A_+{}^2 + D_+{}^2)$, a compensating bump appears in $D_+{}^2$.

[17] Compilation of coupling constants and low-energy parameters, G. Ebel *et al.*, Nucl. Phys. B33, 317 (1971).

[18] J. Lynch *et al.*, Phys. Letters 35B, 457 (1971).

[19] M. E. Rose, *Elementary Theory of Angular Momentum* (Wiley, New York, 1957).

[20] M. Aguilar-Benitez, S. U. Chung, and R. L. Eisner, Phys. Rev. D 6, 11 (1972).

[21] Results of the 6-GeV/c data were reported earlier. See D. J. Crennell, G. R. Kalbfleisch, K.-W. Lai, J. M. Scarr, and T. G. Schumann, Phys. Rev. Letters 19, 44 (1967).

[22] Corrected for all decay modes using the branching ratio from Ref. 13.

[23] M. A. Abolins *et al.*, Phys. Rev. Letters 22, 427 (1969); P. M. Dauber *et al.*, Phys. Letters 29B, 609 (1969); P. L. Hoch (private communication).

[24] For example, J. L. Rosner, in *Experimental Meson Spectroscopy,* edited by C. Baltay (Columbia Univ. Press, New York, 1970), p. 499.

[25] D. Amati, S. Fubini, and A. Stanghellini, Phys. Letters 1, 29 (1962); C. B. Chiu and J. Finkelstein, Nuovo Cimento 59A, 92 (1969); C. Michael, Phys. Letters 29B, 230 (1969); N. W. Dean, Nucl. Phys. B7, 311 (1968).

[26] These results were reported earlier. See D. J. Crennell *et al.*, Phys. Rev. Letters 26, 1280 (1971).

[27] No enhancement is present in the $\Sigma^-(1385)$ region if only events in the K^* bands are plotted.

[28] E. Berger, Phys. Rev. Letters 23, 1139 (1969).

[29] The angular distributions are shown after a background subtraction and correction for the K^* bands which were removed.

[30] For an s-channel Δ isobar the branching ratio would be $(\Delta \rightarrow \Sigma^0 K^0)/(\Delta \rightarrow \Sigma^- K^+) = 2$, whereas if the s-channel resonance were a $N^*_{1/2}$ the branching ratio would be $(N^*_{1/2} \rightarrow \Sigma^0 K^0)/(N^*_{1/2} \rightarrow \Sigma^- K^+) = \frac{1}{2}$. Therefore an s-channel Δ as well as $N^*_{1/2}$ can be ruled out by 2 standard deviations by comparing the backward signals in Fig. 56.

[31] Limited statistics in the forward "forbidden" peaks preclude exact determination of $d\sigma/dt$ at $t_{\min}$. Therefore, we assume the forward peak can be expressed as $d\sigma/dt \propto s^{2(\alpha-1)}$ where $\alpha = \alpha_0 + \alpha' t$. The integrated cross section

$$\sigma_1 = \int_{-\infty}^{t_{\min}} \frac{d\sigma}{dt}\, dt$$

can be expressed as $\propto s^n/\ln s$, where $n = 2(\alpha_0 - 1)$ assuming $\alpha' > 0$.

[32] When the data are fitted with the form $\propto s^n$, we find $n_1 = -4.2 \pm 0.4$, $n_2 = -5.8 \pm 0.5$, and $n_3 = -2.5 \pm 0.3$.

[33] D. R. O. Morrison, Phys. Letters 22, 528 (1966).

[34] See, for example, C. W. Akerlof *et al.*, Phys. Rev. Letters 27, 539 (1971).

[35] Further, if two single particles were exchanged the amplitudes could have an interference which could lead to a polarization of the Λ from the $\Sigma^-(1385)$ decay. However, there are too few events in our data to obtain reliable polarization information.

[36] An experimental comment is in order here. Since the reaction $K^-p \rightarrow \Lambda\pi^-\pi^+$ is dominated by $\Sigma(1385)^+$ as well as ρ^0, f^0, etc., a missing-mass search for $\Sigma(1385)^-$ by detecting π^+ *only* from the reaction $K^-p \rightarrow \pi^+$ + anything is probably fruitless; also the production cross section of $\Sigma(1385)^-$ is small and the possible signal will be buried under overwhelming reflections from other strongly produced resonances as stated above. This, certainly, is the case for the reaction $\pi^-p \rightarrow K^+\Lambda\pi^-$ investigated in this experiment.

PHYSICAL REVIEW D VOLUME 6, NUMBER 5 1 SEPTEMBER 1972

K^+ Decay in Flight*

I-H. Chiang, J. L. Rosen,† and S. Shapiro
University of Rochester, Rochester, New York 14627

and

R. Handler, S. Olsen,‡ and L. Pondrom§
University of Wisconsin, Madison, Wisconsin 53706

(Received 5 May 1972)

From a sample of 10^5 K^+ decays in flight the following branching ratios were obtained: $K_{\mu 2} = (63.24 \pm 0.44)\%$, $K_{\pi 2} = (21.18 \pm 0.28)\%$, $\tau(K^+ \rightarrow \pi^+\pi^+\pi^-) = (5.56 \pm 0.20)\%$, $\tau'(K^+ \rightarrow \pi^+\pi^0\pi^0) = (1.84 \pm 0.06)\%$, $K_{\mu 3} = (3.33 \pm 0.16)\%$, and $K_{e3} = (4.86 \pm 0.10)\%$. The phase-space distributions for three-body semileptonic modes were studied in detail from a second sample of 10^5 decays. For 4017 $K^+ \rightarrow \pi^0 e^+\nu$ events, $\lambda_+ = 0.029 \pm 0.011$. Limits on scalar and tensor form factors of $|f_S/f_+| < 0.13$ and $|f_T/f_+| < 0.75$ (90% confidence) were obtained. For $K^+ \rightarrow \pi^0\mu^+\nu$ a parametrized fit to 3900 events assuming $\lambda_+ = \lambda_- = +0.030$ gave $\xi = -0.09 \pm 0.28$.

I. EXPERIMENTAL ARRANGEMENT

The subject of K^+ decays has been thoroughly reviewed in the literature.[1-3] The experiment discussed here was designed to study the decay of 1.84-GeV/*c* K^+'s in flight, with emphasis placed on good detection efficiency for γ rays from π^0 decay and a minimum of kinematic bias. Optical spark chambers were used to observe the decay products. The technique of using in-flight decay to measure properties in the K^+ rest frame offers certain technical advantages which are worth special mention. The velocity of the decaying system in the laboratory compacts the decay products into a forward cone, and increases their kinetic energy. All of the dominant decay modes of the K^+ except $(\mu^+\nu)$ and $(\pi^+\pi^+\pi^-)$ contain at least one π^0 in the final state. A high-average π^0 energy results in a sample of predominantly well-collimated and high-energy γ rays, which can be detected with better efficiency than the 100-MeV γ rays resulting from K^+ decay at rest. The muons from the decay $(\mu^+\pi^0\nu)$ have an average energy around 500 MeV, and therefore a range of about two collision lengths, which can be advantageous in π^+-μ^+ separation. Furthermore, the K^+ decay can occur in a very-low-density medium – essentially a gas at atmospheric pressure – leading to a good vertex determination and low multiple scattering of the charged secondaries.

The experimental setup is shown in Fig. 1. The 1.84-GeV/*c* K^+ mesons were obtained in a partially separated beam at the Argonne Zero Gradient Synchrotron (ZGS). The K^+ flux was intentionally

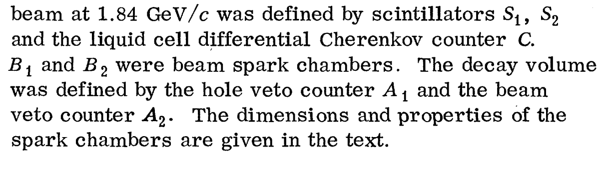

FIG. 1. Plan view of the apparatus. The enriched K^+ beam at 1.84 GeV/*c* was defined by scintillators S_1, S_2 and the liquid cell differential Cherenkov counter *C*. B_1 and B_2 were beam spark chambers. The decay volume was defined by the hole veto counter A_1 and the beam veto counter A_2. The dimensions and properties of the spark chambers are given in the text.